

Development and Analysis of a Tip-based Mechanical Nano-Manufacturing Process: Nanomilling

Submitted in partial fulfillment of the requirements for

the degree of

Doctor of Philosophy

in

Mechanical Engineering

Bulent Arda Gozen

B.S, Mechanical Engineering, Middle East Technical University Ankara, Turkey

Carnegie Mellon University

Pittsburgh, PA

May, 2012

*To my parents,
Deniz and Kenan Gozen,*

Acknowledgements

The research presented in this thesis benefited from the valuable insights and support of many people. It is a great pleasure to express my gratitude and sincere appreciation to all of them.

First and foremost, I want to thank my advisor Prof. Burak Ozdoganlar for his guidance, mentorship and patient support during the course of my PhD. Words cannot express my heartfelt gratitude for his efforts towards my development as good researcher and a future academic. I consider myself ever so lucky to have been mentored by his strong understanding of academic quality that resonated with me in every single way and shaped my future goals as a researcher. The infinite energy he brings to research have taught me to stay resilient and driven in the research process and provided an excellent example that I hope to emulate for the rest of my career.

I wish to thank my committee members, Prof. Alan McGaughey and Prof. Tomasz Kowalewski and Prof. William C. Messner for serving on my committee and providing helpful suggestions regarding my research and its presentation. I also want to thank them for helping me obtain an important perspective on the applicability of my research.

I would like to acknowledge the financial support of the National Science Foundation (CMMI-0602401).

I want to thank Jim Dillinger, John Fulmer and Ed Wojciechowski of the Mechanical Engineering machine shop and Larry Hayhurst of the Chemical Engineering machine shop for their practical guidance and help in fabrication of various components and fixtures. I want to thank Joseph Suhan and Tom Nuhfer for their assistance with scanning electron microscopy. I would like to thank Emre Karagozler and Peter Gilgunn for their help in the NanoFab. I want to thank Evan Robinson for his help with LabView. I also want to thank Dolores Smiller, Bobbi Kostyak and Chris Hertz for their assistance in administrative issues.

During my time in Carnegie Mellon University, I had the privilege of knowing and working with many great people. Special thanks to Prashanth and Nithya for the valuable technical discussions and enjoyable times spent together. I would like to express my gratitude to Recep and Emrullah for their help and support particularly during the last stages of my Ph.D. I want to thank JuEun and Bekir for their efforts in the projects we collaborated. I would like to extend my gratitude to all the other past and present members of the MMDL

Lab that I had the pleasure of working with, including Gerardo, Anmol, Alex, Eralp, Shin Hyung, Sudanshu, Rakesh, Abhinandan, Eric, Murat and Aaron for creating an enjoyable working environment.

I feel blessed to have many great friends in Pittsburgh, who have helped me stay sane and motivated throughout my Ph.D. studies. Special thanks to Sinan for his generous help and support during the first years of my stay in a new country. Thanks to Burak, for being a great best friend whom I can share everything with. I would like to express my gratitude to my dear friends Ersin, Bilge, Tugce and Bekir for their support and literally being my second family in the last two years of my Ph.D. Thanks to all the other close friends I got to know in Pittsburgh, including Emre, Jen, Sherri, Aycil, Ozgur, Gozde and Bilsay. Without them, this experience would not be close to enjoyable as it has been.

Lastly, and most importantly, I want to thank my parents, Deniz and Kenan Gozen, for their unconditional love, support and encouragement. I am truly blessed to have them as my parents and be able to make them proud. They are the primary reason and the source of inspiration for everything I have achieved in my life, including this work. That is why, I dedicate this thesis to them with all my love and gratitude.

"There is no shortcut to truth, no way to gain knowledge of the universe except through the gateway of the scientific method"

-Karl Pearson

Abstract

As an alternative to well-established nano-lithographic methods, mechanical manufacturing methods which are widely applied in macro and micro-scales, have also been adapted to nano-scale. Recently, tip-based mechanical nanomanufacturing have been realized through the use of Atomic Force Microscopes (AFM) where the ultra-sharp AFM probe is used to induce sufficiently high contact stresses to remove material from variety of surfaces. Even though the basic applicability of the AFM-based mechanical nanomanufacturing have been demonstrated, its application as a viable controlled nanomanufacturing method is hindered by a number of issues including high dimensional uncertainty, limited shape capability, rapid tip wear, and inefficient material removal.

In this Ph.D. research, to address the issues with the current application of AFM-based methods, a new tip-based mechanical nanomanufacturing process, referred to as *nanomilling*, is proposed. **The overarching objective of this Ph.D. research** is to develop, implement and analyze a novel nanomanufacturing process, *nanomilling*, and the associated equipment. The nanomilling process imposes high-frequency rotational motions to the ultra-sharp probe tip (nanotool) using a piezoelectric actuator, achieving a configuration similar to that of the conventional milling process. By imposing controlled high-frequency motions and implementing a high-stiffness nanotool configuration, nanomilling has the potential to exhibit high-dimensional accuracy and repeatability, achieve high material removal rates and effectively reduce tip wear and forces. Development, implementation and analysis of the nanomilling process constitute the foundation for realization of high-volume, controlled tip-based mechanical nanomanufacturing.

To achieve the overarching research objective, first, the nanomilling method and the associated system is developed. Two fundamental nanomilling configurations are identified: in-plane and out-of-plane configurations where the nanotool is rotated within a plane parallel and perpendicular to the sample surface, respectively. The nanomilling system mainly includes a three-axis piezo-stack actuator hosting the nanotool and imposing the high-frequency rotations, a high-stiffness nanotool assembly and a high-precision nanopositioning stage that controls the feeding motions to create desired feature shapes during nanomilling.

Successful implementation of the nanomilling process requires precision characterization and control of the high-frequency nanotool rotations and feeding motions. To characterize the motions of the piezo-stack actuator and the nanopositioning stage, a three-dimensional motion measurement setup is constructed. To generate accurate nanotool rotations, a comprehensive method is developed for characterization and mathematical representation

of non-linear dynamics of piezo-stack actuators. The obtained dynamic representations are then utilized to devise a frequency-domain open-loop method to control the piezo-stack actuator motions. The capability of this method to generate desired nanotool rotations with high accuracy is demonstrated.

Having developed the nanomilling method, the associated system and established the methodology for precision control of nanomilling motions, the dimensional accuracy of the process is evaluated. It was shown that the removal depth and width can be controlled with 5 nm accuracy using the nanomilling process. The preliminary observations on material removal mechanism showed that nanomilling process is able to remove material in the form of long and curled chips.

Finally, the preliminary studies are conducted on the nanotool wear characteristics of the process. A method for experimentation and quantitative analysis of nanotool wear is devised.

Specific contributions of this thesis research include: (1) A novel rotating-tip-based mechanical nanomanufacturing method and associated system that is capable of creating nano-scale features with 5 nm dimensional accuracy, (2) A new method for accurate characterization and representation of three-dimensional dynamic motions of piezo-stack actuators, including those used in the nanomilling system, (3) An experimental understanding on the characteristics of the non-linear dynamic motions of piezo-stack actuators, (4) A frequency-domain-based open-loop method for controlling the non-linear, three-dimensional motions of multi-axis piezo-stack actuators, (5) An approach for quantitative analysis of wear in nanometrically-sharp probe-tips.

Contents

Acknowledgements	ii
Abstract	v
List of Figures	xi
List of Tables	xv
1 Introduction	1
1.1 Motivation	1
1.2 Research Objectives	3
1.3 Research Contributions	4
1.4 Thesis Organization	5
1.5 Literature Review	6
1.5.1 AFM-based mechanical nanomanufacturing	6
1.5.2 Mechanical Material Removal at Nano-scale	8
1.5.3 Tip Wear at Nano-scale	9
2 Development of the Nanomilling Process and System	10
2.1 Nanomilling Process Kinematics	10
2.2 Nanomilling System and Procedure	12
2.2.1 Nanotool Assembly	12
2.2.2 Obtaining Nanotool Motions	13
2.2.3 Sample Attachment and Surface-Contact Indication	13

2.2.4	Data Acquisition and Process Control	15
2.2.5	Nanomilling Procedure	15
2.3	Characterization and Alignment of Nanomilling Motions	15
2.3.1	Three-Dimensional Motion Measurement System	16
2.3.2	Sample Reference Frame	18
2.3.3	Characterization and Generation of the Nanopositioning Stage Motions	19
2.3.4	Dynamic Characterization of the Piezoelectric Actuator	19
3	Characterization of Three-Dimensional Dynamics of Piezo-Stack Actua-	
	tors	22
3.1	Introduction	22
3.2	Experimental Methods	24
3.3	Analysis of the Experimental Data	27
3.3.1	Frequency Domain Categorization of the Response	27
3.3.2	Power Analysis	27
3.3.3	Frequency Response Representations for the Dynamic Response of Piezo-Stack Actuators	29
3.4	Application of the Characterization Method	31
3.4.1	Results of the Stepped-Sine Testing	31
3.4.2	Power Analysis	33
3.4.3	Analysis of extended-FRFs	36
3.5	Analysis of Measurement Errors	40
3.6	Summary and Conclusions	44
4	A Method for Open-loop Control of Dynamic Motions of Piezo-stack Ac-	
	tuators	46
4.1	Introduction	46
4.1.1	Calculation of response to arbitrary excitations	48
4.2	Definition of the control problem	49
4.3	Determination of the excitations to generate arbitrary single-frequency motions	53

4.3.1	Determination of the fundamental excitation component	53
4.3.2	Determination of the compensatory excitation components	54
4.4	Evaluation of the control method	59
4.4.1	Experimental Details	59
4.4.2	Evaluation Method	60
4.4.3	Results of the Evaluation Tests	63
4.5	Analysis of Measurement Errors	66
4.6	Summary and Conclusions	67
5	Evaluation of the Dimensional Accuracy and Shape Capability	69
5.1	Accuracy of Feature Depth	69
5.2	Accuracy of Feature Width	71
5.3	Shape Capability of Nanomilling	74
5.4	Observations on Material Removal Mechanism	75
6	Preliminary Analysis of Nanotool Wear	77
6.1	Experimental and Analysis Method	77
6.2	Results	82
6.3	Preliminary studies on nanotool replication for wear progression studies . .	83
7	Conclusions	86
8	Future Work	90
8.1	Completion of the fundamental research on the nanomilling process	90
8.1.1	Analysis of the nanotool wear	90
8.1.2	Realization of force measurement during nanomilling	91
8.1.3	Analysis of material removal	92
8.2	Towards Industrial Feasibility of Nanomilling	93
8.2.1	Parallelization of the Nanomilling Process	93
8.2.2	Combination of the Nanomilling and Elastomer Molding Processes .	94

List of Figures

1.1	AFM images of the features created using AFM-based mechanical nanomanufacturing: (a) Small characters created by Choi <i>et al</i> [15], (b) A two dimensional structure created by Yan <i>et al</i> [12], (c) Human face nano-structure fabricated by Yan <i>et al</i> [13].	6
1.2	Number of issues of AFM-based mechanical nanomanufacturing highlighted Notargiacomo et al [21]: (a) AFM topography and (b) three-dimensional view of a series of lines patterned on the aluminium surface with different amount of force applied. The distortion at the end of the lines is due to the torsional deflection of the AFM cantilever. The section profile along the (c) aa' and the (d) bb' directions show the formation of the ridges alongside the created lines indicating a ploughing type material removal mechanism. . . .	7
2.1	Two basic configurations of the nanomilling process: (a) the in-plane configuration and (b) the out-of-plane configuration.	11
2.2	The nanomilling system and its components.	12
2.3	The contact detection method used for determination of nanotool-surface contact.	14
2.4	The LDV-based measurement system for 3D characterization of dynamic nanomilling motions.	17
2.5	Alignment of three orthogonal laser beams (a) Course positioning of the beams on the acrylic post, (b) Perpendicular alignment of laser beams on cornercube faces (c) Final configuration of the laser beams.	18
2.6	The nonlinear response characteristics of the piezoelectric actuator: The response at the harmonics of the excitation frequency for (a) $\omega_{ex} = 3$ kHz, and (b) $\omega_{ex} = 4$ kHz; and (c) the frequency response function showing the effect of amplitude (excitation voltage) on the response at the excitation frequency for $\omega_{ex} = 3$ kHz.	20
3.1	Depiction of a typical multi-axis piezo-stack actuator.	23
3.2	Description of the stepped-sine testing method: (a) A sinusoidal voltage with a specific amplitude is supplied to one of the stacks of the actuator at the selected excitation frequency, (b) the piezo-stack actuator's response is measured in 3D using the three laser beams, and (c) the time-domain responses in each of the three (measurement) reference axes are converted to frequency domain through FFT.	25
3.3	Description of the frequency refinement procedure: Response occurs not only at the excitation frequency, but also its harmonics. Those regions in which the rapid changes occur on the response either at the excitation frequency or at its harmonics are refined using smaller excitation-frequency increments. .	26

3.4	(a) A typical response amplitude (in logarithmic scale) as function of the excitation and response frequencies, and (b) the response amplitude corresponding to a particular excitation step at $\omega_{ex} = 3$ kHz, indicating the responses at the harmonics of the excitation frequency.	32
3.5	Percent contribution of the fundamental response component to the total response power for Actuator 1: (a)-(c) As a function of both the excitation frequency and amplitude to excitation of stacks x , y and z , respectively; (d)-(f) as a function of the excitation frequency at excitation amplitudes of 160 V and 60 V given for responses to excitation of stacks x , y and z , respectively.	33
3.6	Cumulative percent contribution of the higher harmonic response components to the total response power for Actuator 1: (a)-(c) As a function of both the excitation frequency and amplitude to excitation of stacks x , y and z , respectively; (d)-(f) as a function of the excitation frequency at excitation amplitudes of 160 V and 60 V given for responses to excitation of stacks x , y and z , respectively.	34
3.7	Percent contribution of the non-harmonic response component to the total response power for Actuator 1: (a)-(c) As a function of both the excitation frequency and amplitude to excitation of stacks x , y and z , respectively; (d)-(f) as a function of the excitation frequency at excitation amplitudes of 160 V and 60 V given for responses to excitation of stacks x , y and z , respectively.	35
3.8	Percent contribution of the fundamental response component to the total response power given for Actuator 2: ((a)-(c) As a function of both the excitation frequency and amplitude to excitation of stacks x , y and z , respectively; (d)-(f) as a function of the excitation frequency at excitation amplitudes of 160 V and 60 V given for responses to excitation of stacks x , y and z , respectively.	37
3.9	Amplitude ratios of fundamental nFRFs corresponding to the excitation of the x stack for Actuator 1: (a)-(c) As a function of the excitation frequency and amplitude measured along x_m , y_m and z_m directions, respectively, and (d)-(f) as a function of the excitation frequency at the tested excitation amplitudes measured along x_m , y_m and z_m directions, respectively.	38
3.10	Amplitude ratios of to the first three nFRFs and nhFRF corresponding to the excitation of z stack and response along the z_m axis for Actuator 1: (a)-(d) As a function of the excitation frequency and amplitude. (e)-(h) as a function of the excitation frequency for the excitation amplitudes of 10 V and 160 V.	39
3.11	Amplitude ratios of to the first three nFRFs and nhFRF (in log scale) corresponding to the excitation of z stack and response along the z_m axis for Actuator 2: (a)-(d) As a function of the excitation frequency and amplitude. (e)-(h) as a function of the excitation frequency for the excitation amplitudes of 10 V and 160 V.	41
3.12	Percent harmonic and non-harmonic error amplitudes as functions of the excitation frequency (a)-(c) Percent amplitude errors for the first three harmonic error components (d) Percent amplitude errors for the non-harmonic error components	42
4.1	Geometric description of three-dimensional single frequency motions	50
4.2	Frequency domain representations of the response terms (a) $\mathbf{R}_1(\omega)$ (b) $\mathbf{R}_n(\omega)$ and (c) $\mathbf{H}(\omega)$	51
4.3	The reduction of third harmonic power through first level harmonic compensation for the cases where the fundamental excitation of 160 V amplitude is supplied to the (a) x -stack (b) y -stack and (c) z -stack of the actuator. . . .	55

4.4	Description of the multi-level stepped-sine testing procedure. The fundamental excitation is supplied to x stack as an example.	56
4.5	Reduction of the third harmonic response power through four levels of harmonic compensation for the cases where the y -stack of the actuator is excited with a fundamental excitation of 160 V amplitude at (a)2.5 kHz (b)3 kHz and (c)3.5 kHz.	58
4.6	Determination of harmonic motions: (a)total motion (b)harmonic motion obtained as a result of the sample-by-sample averaging	60
4.7	Definition of deviation metrics (a) In-plane harmonic evaluation metrics for non-linear motions (b) Out-of-plane harmonic evaluation metrics for non-linear motions (c) Determination of in-plane non-harmonic deviation (d)Determination of out-of-plane non-harmonic deviation (e) Harmonic evaluation metrics for linear motions	62
4.8	Effect of the compensatory excitation on the harmonic errors (a)Radial deviation ($F(\theta)$) plot ,all numbers are in percentile (b)Normal deviation . . .	65
5.1	An AFM measurement of the steps created on a PMMA surface using the in-plane configuration of the nanomilling process for evaluation of the depth prescription.	71
5.2	An AFM measurement of three channels created on a PMMA surface using the out-of-plane configuration of the nanomilling process. The horizontal axis of the bottom figure is compressed to show all three channels.	72
5.3	The V-shaped trench created to demonstrate the different-width capability during a single nanotool-pass using the in-plane nanomilling configuration. .	73
5.4	Various features created by nanomilling	74
5.5	SEM images of the channels created using different nanotool motions. The long and curled chips observed for the cases with nanotool motions indicate that the material removal mechanism is shearing dominated. No-motion (scratch) case does not produce chips consistently, indicating the dominance of the ploughing mechanism.	76
6.1	AFM image of the channels created during the wear tests	78
6.2	AFM images of an unused diamond nanotool (a) Low resolution image (b) High resolution image (c)Three dimensional representation of the high resolution image	79
6.3	The result of the correlation of two AFM images corresponding to the same nanotool, (a) First high resolution image (b) Second high resolution image before angular and translational alignment, (c) Second high resolution image after the alignment, (d-e) Cross-sectional data corresponding to the aligned images around the apex along the X and Y axes, (f) The height difference map of the aligned images.	80
6.4	SEM images of the unused and worn nanotools	81
6.5	Results of the wear experiments. Three dimensional images of the nanotool before and after nanomilling in the (a) in-plane (d) out-of-plane configurations, the unused nanotool is depicted by a wireframe representation. Cross sectional images of the unused and worn nanotools after nanomilling in the (b) in-plane (e) out-of-plane configurations. Height difference maps around the nanotool apexes after (c) in-plane (f) out-of-plane nanomilling.	82
6.6	Two step molding process to produce nanotool replicas	83
6.7	AFM images of the obtained nanotool replicas (a)Original unused nanotool (b)PU replica (c)Resin replica	84

8.1	Three-dimensional AFM images and height density plots of the (a-b) step structure nanomilled on a PMMA surface and corresponding (c-d) PDMS mold	95
-----	--	----

List of Tables

3.1	Parameters used during the characterization of the piezo-stack actuators. .	31
3.2	Percent contributions of harmonic response components corresponding to the excitation of the y stack with an excitation frequency and amplitude of 16 kHz and 160 V, respectively.	36
3.3	Largest error amplitudes and ratios for the first five harmonic and non-harmonic response components.	43
4.1	Results of the evaluation tests for circular, elliptical and general Lissajous curve shaped motions. Error terms are given in percentages unless noted otherwise.	63
4.2	Results of the evaluation tests for linear motions. Error terms are given in percentages unless noted otherwise.	64
5.1	Prescribed depths, average depths, and standard deviation of the steps created during in-plane nanomilling.	70
5.2	The width-increase rates and associated width variation for four V-shaped channels nanomilled using the in-plane configuration to assess the single-pass width capability.	71
6.1	Experimental parameters used during the characterization of the piezo-stack actuators.	78
8.1	Experimental parameters to be used during the experimental analysis of nan-tool wear.	91
8.2	Experimental parameters to be used during the experimental analysis of material removal.	93

Chapter 1

Introduction

1.1 Motivation

Nanodevices such as integrated circuits, data storage and memory devices, optical devices, sensors, and analytical devices can provide many benefits by taking advantage of the modified physical/chemical properties and behavior at the nano scale. However, without repeatable, accurate and high-throughput (scalable) nanomanufacturing techniques that are applicable to a broad range of materials, the potential benefits of these devices cannot be fully realized. Since early 1990's a wide-range of lithographic methods such as optical lithography, x-ray lithography, electron and focused ion beam lithography have been developed and considered as well-established methods of nanofabrication [1]. More recently, other nano-manufacturing approaches, such as molding and embossing based methods, electrical and nano-transfer printing, and self-assembly methods have been demonstrated [2].

As an alternative to lithographic and other nanomanufacturing methods, motivated by the agility of the mechanical manufacturing techniques used in the macro- and micro-scales, researchers have attempted to develop mechanical nanomanufacturing approaches for fabrication of 3D nano-scale features and devices. Mechanical material removal methods, such as milling, are preferred in a broad range of manufacturing applications in different size scales due to their versatility, geometric capability, high precision, wide-range material applicability, and low overall cost. Precision machining methods, such as diamond turning [3], may be considered as the first application of mechanical manufacturing techniques to nano-scale material removal [4, 5].

More recent application of mechanical nanomanufacturing involve the utilization scanning probe microscopy (SPM) systems to facilitate tip-based nanomanufacturing. In gen-

eral, SPM tips with tip radii up to a few tens of nanometers have been used to selectively modify surfaces in mechanical, electrical, electrochemical, and/or photonic manners to remove or add nano-scale features. The main advantages of the tip-based nanomanufacturing methods include (1) the ability to induce selective surface modifications with high spatial resolution, (2) the capability to perform *in-situ* characterization of the fabricated features, (3) the applicability to a broad range of materials and media, and (4) the ease of use and relatively low-cost of application [6, 7]. Mechanical modification of surfaces is commonly performed using atomic force microscope (AFM) systems, the primary intent of which is the nano-scale characterization of surface topographies [8].

In AFM-based mechanical material removal, standard AFM cantilevers are used under high normal forces (significantly higher forces compared to AFM measurements), inducing sufficient contact stresses to create plastic deformation (ductile) or brittle fracture (brittle) on the material surface [9, 10]. The tip is moved along a prescribed path to scratch and plough the substrate. Repeated scratches are used to create deep trenches and pockets. In addition to the contact mode, the tapping mode is used to "dynamically plough" the material from the surface.

Although the application of the AFM-based mechanical nanomanufacturing has been demonstrated in the literature, its usage as a viable, controlled nanomanufacturing process has been hindered by a number of factors:

- **Low dimensional accuracy:** Although AFM has superior positional accuracy, due to the force controlled—as opposed to displacement controlled—process, the resulting depth of removal depends on the type and uniformity of the substrate material, the tip shape, the existing surface topography as well as a number of operational parameters such as removal speed. This precludes straightforward fabrication of controlled features.
- **Limited shape capability:** The large tip forces required during nano-scratching generally causes large torsional deflections if the tip is moved lateral to the beam axis. Moreover, truly three-dimensional features have not been commonly fabricated using AFMs.
- **Rapid tip wear:** In the manner that the AFM-based mechanical nanomanufacturing is currently practiced, the tip wear rate is relatively large due to the large contact stresses. Furthermore, the mechanism of tip wear is not clearly understood.
- **Inefficient material removal:** The surface modification through AFM-based nano-

scratching is usually realized through ploughing type plastic deformation, rather than removal through shearing (chip formation). This causes unwanted material accumulation in the vicinity of the created features and increases tip wear. The shape and size of the tip, the workpiece material, and the AFM nanomachining conditions (depth, width, speed, tip motion) have a significant effect on the mechanism of material removal which has not been studied in detail.

Therefore, limitations of the current application of the AFM-based methods prevent the realization of controllable tip-based mechanical nanomanufacturing techniques with geometric capability and applicability to a diverse selection of materials. Addressing and resolving these issues and gaining fundamental understanding on the nanoscale mechanical removal of material and tip wear can potentially render tip-based mechanical nanomanufacturing as a viable nanomanufacturing process for a wide range of applications. Such a research effort may constitute the foundation for large impact applications of tip-based mechanical nanomanufacturing where molds and lithography masks with nano-scale features are created through simultaneous operation of multiple tips, thereby leading to effective high-volume fabrication of nanoscale devices.

1.2 Research Objectives

In this PhD. research, a new tip-based nanomanufacturing method, referred to as *nanomilling*, is proposed in an effort to address the aforementioned issues with AFM-based methods and to realize controllable tip-based mechanical nanomanufacturing. The nanomilling process uses an ultra-sharp tip (with nominal radius of a few tens of nanometers) as the nanotool and imposes high-frequency rotational motions to the nanotool using piezoelectric actuators, thereby achieving a configuration similar to the conventional macro-scale milling process. By imposing controlled high-frequency nano-scale motions to the tip, nanomilling has the potential to widen the shape and size capability, achieve high material removal rates and effectively reduce tip wear and forces. Implementation of a high-stiffness nanotool configuration enables direct prescription and control of the position of the tool-tip (rather than forces), providing high-level dimensional accuracy and repeatability.

The nanomilling process carries the potential of becoming a viable controlled nanomanufacturing process. However, to realize this potential, there is a strong need for research on both practical and fundamental aspects of the nanomilling process. **The overarching objective of this PhD. research** is to develop, implement and analyze a novel nanoman-

ufacturing process, *nanomilling*, and the associated equipment. This overarching objective is addressed through the following specific objectives:

1. **To develop and implement the nanomilling system:** The unique aspects of the nanomilling process such as the high-stiffness nanotool configuration and rotational motions cannot be realized through the commercially-available SPM systems. Accordingly, the aim of this objective is to develop a dedicated system/testbed for nanomilling, and to establish the corresponding nanomilling procedure.
2. **To characterize and control the three-dimensional dynamic motions of piezo-stack actuators used as a means to generate nanotool rotations:** Precision control of the nanomilling motions is critical to satisfy the dimensional accuracy and repeatability requirements. The aim of this objective is to develop an experimental framework for measurement and alignment of the motions of various components of the nanomilling system. The emphasis is placed on the accurate generation of the high-frequency rotational motions of the nano-tool through the use of piezo-stack actuators. Thus, a comprehensive method for dynamic characterization and open-loop control of piezo-stack actuators will be devised.
3. **To evaluation the dimensional accuracy of nanomilling:** The implementation of a high-stiffness nanotool configuration and precision controlled nanomilling motions enables attaining high dimensional accuracy of the created features through nanomilling. To evaluate this capability, a number of reference features are created using the developed nanomilling system. The dimensions of the created features (measured using AFM) are then compared to the prescribed dimensions and dimensional accuracy of nanomilling is quantified.
4. **To devise a method for quantitative analysis of nanotool wear:** Nanotool wear significantly affects the throughput, accuracy, and geometric capability of the nanomilling process. This objective aims to devise an experimental and analysis method for quantitative analysis of nanotool wear. The outcomes of this preliminary study will be foundational for more comprehensive studies on nanotool wear and its dependence on various process parameters.

1.3 Research Contributions

The specific technical contributions of this Ph.D. research are:

1. A novel rotating-tip-based mechanical nanomanufacturing method and associated system that is capable of creating nano-scale features with 5 nm dimensional accuracy.
2. A new method for accurate characterization and representation of three-dimensional dynamic motions of piezo-stack actuators, including those used in the nanomilling system.
3. An experimental understanding on the characteristics of the non-linear dynamic motions of piezo-stack actuators.
4. A frequency-domain-based open-loop method for controlling the non-linear, three-dimensional motions of multi-axis piezo-stack actuators.
5. An approach for quantitative analysis of wear in nanometrically-sharp probe-tips.

1.4 Thesis Organization

In the next section of this chapter, the literature review on the AFM-based mechanical nanomanufacturing, experimental methods on the analysis of nano-scale mechanical material removal and tip wear is presented. In chapter 2, the nanomilling process and the developed nanomilling system is introduced. Process kinematics, construction of the nanomilling system and characterization and alignment of nanomilling motions are discussed in detail. In chapter 3, the method for dynamic characterization and mathematical representation of piezo-stack actuator dynamics is presented. In chapter 4, open-loop control method for piezo-stack actuators is explained, demonstrating the capability of imposing nano-scale rotational nanotool motions with high accuracy. In chapter 5, the dimensional accuracy and shape capability of the nanomilling system is evaluated. In chapter 6, preliminary studies on the development of an experimental method for quantitative analysis of nanotool wear are presented. Chapter 7 summarizes the conclusions from the presented research. Chapter 8 discusses the future work that is needed for rendering nanomilling as a high-throughput, industrially feasible nanofabrication process and the extension of the conducted fundamental research.

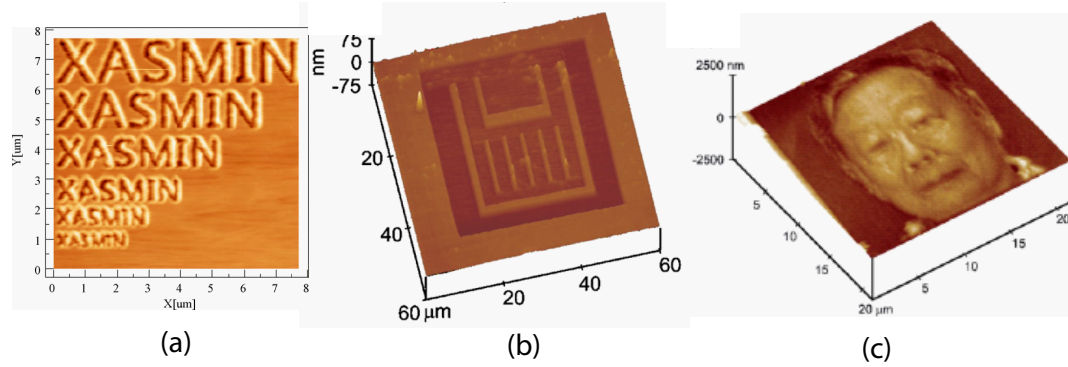


Figure 1.1: AFM images of the features created using AFM-based mechanical nanomanufacturing: (a) Small characters created by Choi *et al* [15], (b) A two dimensional structure created by Yan *et al* [12], (c) Human face nano-structure fabricated by Yan *et al* [13].

1.5 Literature Review

1.5.1 AFM-based mechanical nanomanufacturing

Since the late 90s, variety of SPM systems, such as scanning tunneling microscopes (STM) and atomic force microscopes (AFM), have been used to create nano-scale features mechanically on various materials [11]. Using AFMs at force levels significantly higher than those used for topography measurements, a variety of simple and complex shapes (see Fig. 1.1) were created on semiconductor [14], metal [12, 13], and polymer/photoresist [15, 16] surfaces through indentation and *scratching* using the AFM probe tip. Various applications of AFM-based mechanical nanomanufacturing have been identified, including shaping of mask layers for lithography [21], fabrication of single-electron transistors (SETs) [17], Coulomb blockades, quantum point contacts, quantum nano-dots, quantum wells, nano-wires [18–20] and grating structures [15].

Although the basic capability of AFM-based mechanical nanomanufacturing techniques has been established, several issues prevent the application of these techniques as viable nanomanufacturing approaches. First, the modification of surfaces through scratching with high normal forces is commonly realized through the mechanism of ploughing (i.e., plastic deformation) rather than shearing (i.e., removal of material in the form of a chip). This causes accumulation, rather than removal, of the material in the vicinity of the created features (i.e., ridge formation, see Fig. 1.2) [21–23] and induces significant increases in tip deformation and wear. Second, the process throughput is limited by the low translational speeds of the AFM systems, and the rapid tool wear arising from the ploughing-dominated material removal mechanism [16, 18, 21–24]. Third, accurate features can only be fabricated

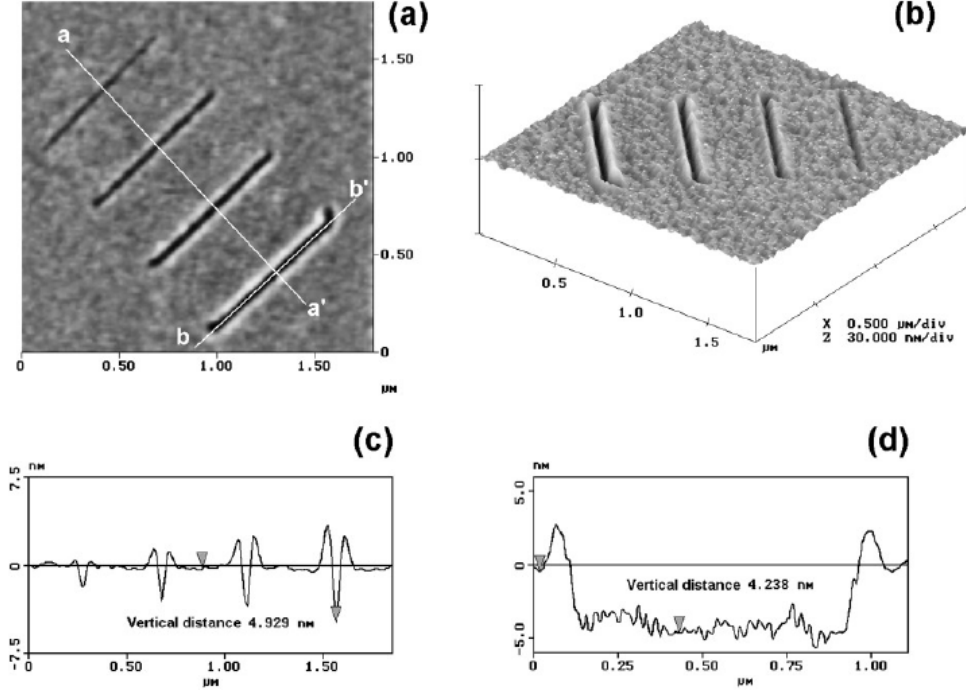


Figure 1.2: Number of issues of AFM-based mechanical nanomanufacturing highlighted Notargiacomo et al [21]: (a) AFM topography and (b) three-dimensional view of a series of lines patterned on the aluminium surface with different amount of force applied. The distortion at the end of the lines is due to the torsional deflection of the AFM cantilever. The section profile along the (c) aa' and the (d) bb' directions show the formation of the ridges alongside the created lines indicating a ploughing type material removal mechanism.

through iterative processing. This is due to the fact that AFM scratching is a force-based, as opposed to a displacement-based, process: The depth of removal is dictated *indirectly* by monitoring the AFM cantilever deflections, which are correlated with the forces applied at the tip. Since the removal forces depend on removal conditions (e.g., removal speed) [25–29], tip geometry [23,24,28,30], material properties and inhomogeneities [16], the original surface topography [16] and progressing tip wear [14,31], a non-linear tip forces vs. removal depth relationship and corresponding dimensional uncertainty in fabricated geometries are present. Torsional deflections of the AFM cantilevers has also been shown to affect the created feature geometry [21] (see Fig. 1.2). Further improvements to the AFM-based techniques, such as the use of high-stiffness cantilever [14, 22, 32, 33], vibrating cantilevers [18, 25], ultrasonic

vibrations of the sample [34], depth control algorithms [13,35], and diamond tips (to reduce wear) [14], have been implemented with limited success.

1.5.2 Mechanical Material Removal at Nano-scale

Researchers used in-situ measurements and post-test observations to determine the mechanism of tip-surface interaction during tip-based mechanical material removal processes. By in-situ measurement of forces acting on the tip, characterization of the process has been made through determination of several parameters such as friction coefficient [36–38], scratch hardness [39], specific cutting energy [38]. Acoustic emission based methods that have been widely used for larger scale machining processes have been recently applied in nano-scales. It has been shown that acoustic waves are generated from surfaces due to plastic deformation or crack initiation [40] and different forms of plastic deformation can be identified through the monitoring of several acoustic wave characteristics [37]. Volume analysis using the AFM measurements of the created features involves determining the volume of the removed material and the ploughing debris accumulated in the vicinity of the feature. The ratio of these volumes provides distinction between cutting and ploughing regimes [37,41].

Change of material characteristics as a result of the mechanical material removal has also been investigated. Residual stresses and subsurface damage can be observed through the diffraction patterns in the TEM images [42,43]. Furthermore, the mechanical material removal has been shown to induce certain chemical changes both on the surface and the subsurface regions of the modified materials. These changes can be examined through electric potential measurements using AFM [42] or material composition measurements using X-Ray spectroscopy [42,43].

As a result of the experimental analysis, several distinct forms of material behavior have been observed during mechanical material removal at nano-scale. Usually polymers with low modulus of elasticity exhibit elastic behavior resulting in significant elastic recovery after modification [43,44]. Ploughing type behavior (plastic deformation and displacement of the material) has been observed for many materials for low normal forces and/or depths [37,45]. For metals and polymers combination of ploughing and cutting behavior (chip formation) can be observed depending on several process parameters such as the applied normal force and tip geometry [38,41,45,46]. Ductile cutting can also be observed for brittle materials for certain cutting depths [40]. Brittle behavior in the form of crack generation and propagation is widely observed for materials brittle nature such as silicon [47,48], GaAs [49] or even

non-brittle materials like polymers [43] under high loads.

1.5.3 Tip Wear at Nano-scale

Several experimental methods have been utilized to study the wear of the silicon [50, 51], silicon nitride [50, 52], diamond [53, 54] and diamond like carbon (DLC) [55] tips during their interactions with various material surfaces. AFM measurements of the tips before and after their use for material removal are used to determine the volume worn during the process. By associating this volume to normal load and total process length, wear rate can be evaluated [53, 54]. Archard's Law is a commonly used empirical approach which relates the wear volume with normal load, distance and the material hardness [52, 55]. The proportionality constant in this law is empirically determined and provides a quantitative measure for tip wear. An indirect quantitative monitoring of tip wear can also be achieved through observation of the removal depth at constant normal load. It has been shown that the removal depth decreases as the tool gets blunter and the contact stresses decrease [53, 54]. Qualitative tools such as TEM and Raman spectroscopy are used to study the mechanism of tip wear. Researchers utilized TEM imaging of the tip to observe changes in the crystal structure [51, 55] and Raman spectroscopy to examine the chemical changes that can be exhibited by the tip [55].

It has been observed that for the ultra sharp tips of radius around 10 nm or less, both gradual or sudden (fracture based) wear can occur [55]. It has been noted that, regardless of material, the tip undergoes some plastic deformation due to high contact stresses [52, 53]. Chung *et al* reported that the silicon tip wear is initiated by the quick abrasion of the amorphous layer at the very tip and is followed by gradual flattening and oxidation of the crystalline silicon [51]. Similarly for DLC, it has been reported that amorphous carbon wears off before the crystalline diamond leading to a wear rate reducing in time [55]. For silicon nitride tips, main wear mechanisms are determined to be adhesive wear [50, 52] and low cycle fatigue [52]. Zhao *et al* determined that diamond tip under severe machining conditions undergoes a chemical wear at high local temperatures by reaction of carbon with oxygen and silicon [53]. It has also been noted that the environmental conditions such as the media in which the process takes place [51] and humidity [50] play significant role in tip wear.

The literature review on the dynamics and control of piezo-stack actuators are provided in the associated chapters.

Chapter 2

Development of the Nanomilling Process and System

In this chapter, the nanomilling process and the associated system is introduced, an experimental framework for characterization and alignment of various nanomilling motions is established. The technical contribution of the work presented in this chapter, is the dedicated nanomilling testbed and procedure that constitutes the experimental foundation for the further research on the practical and fundamental aspects of the nanomilling process.

2.1 Nanomilling Process Kinematics

In this section, we briefly describe the nanomilling process and its basic configurations, which were originally presented in [56]. The material removal in nanomilling is accomplished by rotating a nanotool (an AFM-probe tip with as small as 10 nm tip radius) in an elliptical pattern, while feeding the sample along a path at a prescribed depth of removal. Similar rotational motions, but with significantly larger amplitudes, have been recently used for fabricating complex micro-scale features using single-point diamond tools to facilitate reduction of machining forces and tool wear [57, 58]. As described below, the nanotool rotation is obtained through three-dimensional motions of a piezoelectric-stack, on which the nanotool is attached. Two basic configurations of the nanomilling process—in-plane and out-of-plane—are depicted in Fig. 2.1.

For the in-plane configuration shown in Fig. 2.1 (a), the three-axis piezoelectric actuator is excited to generate an elliptical nanotool motion in a plane parallel to the sample surface (the $x_s - y_s$ plane). The specific shape and the speed of the elliptical nanotool motion is

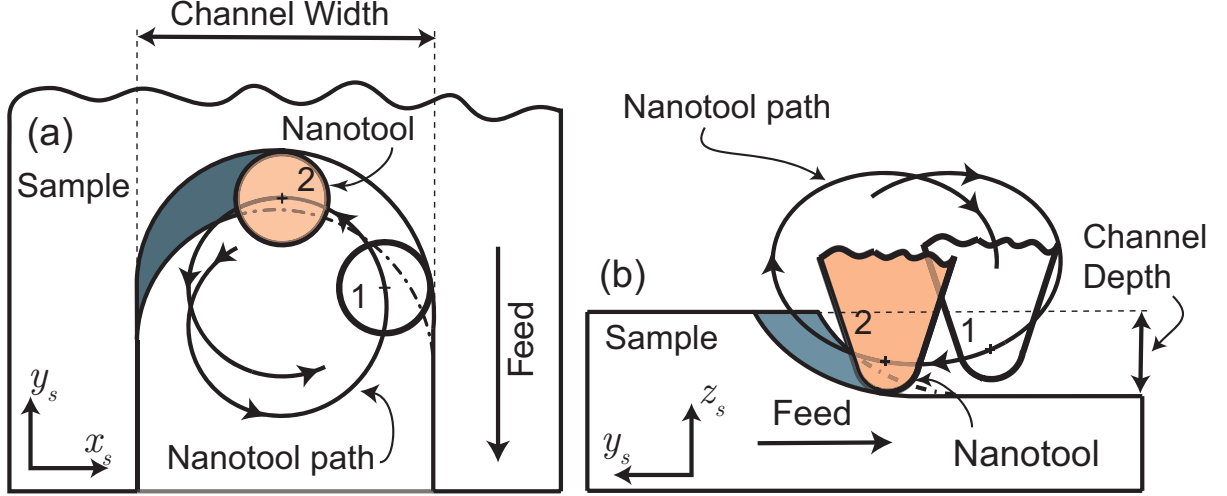


Figure 2.1: Two basic configurations of the nanomilling process: (a) the in-plane configuration and (b) the out-of-plane configuration.

controlled by varying the amplitude and frequency of the voltage inputs to the piezoelectric actuator, whereas the channel depth is prescribed by moving the sample using a nanopositioning stage. If the depth of removal is larger than the spherical portion of the tip (with circular cross-section, as shown in Fig. 2.1(a)), the nanotool cross-section changes into a triangular or rectangular shape at higher elevations. Continued motion of the nanotool along the nanotool path causes the material (the shaded region in Fig. 2.1(a)) to be removed. Through the feeding motions, complex shapes can be created on the sample surface along the prescribed feeding path. Importantly, the width of the feature created during a single pass can be controlled by changing the diameter of the elliptical nanotool motion (in the x_s direction).

For the out-of-plane configuration, the nanotool is rotated in a plane (the $y_s - z_s$ plane) that is perpendicular to the sample surface plane. Figure 2.1(b) depicts a cross-sectional view of the process. The shaded portion of the sample material is removed as the nanotool follows the motion path (both up-milling and down-milling configurations can be realized). The depth of removal during a single pass is prescribed by the nanotool path along the sample-surface normal (z_s), rather than through the use of the nanopositioning stage as in the in-plane configuration. Deeper features can still be obtained by providing additional depth-direction movements through the nanopositioning stage. The channel width and shape that can be fabricated in a single tool pass are dictated directly by the shape of the nanotool.

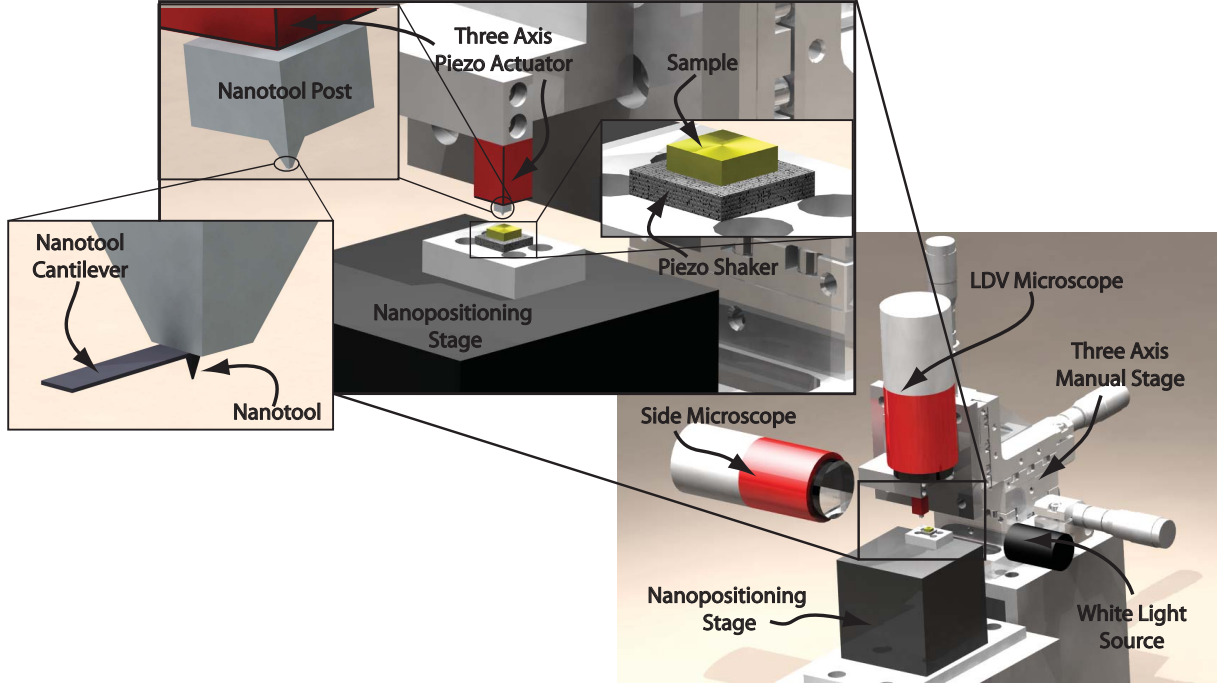


Figure 2.2: The nanomilling system and its components.

2.2 Nanomilling System and Procedure

To perform the nanomilling process, a nanomilling system shown in Fig. 2.2 was designed and constructed. This section describes different subsystems of the nanomilling system and their operation during the nanomilling process.

2.2.1 Nanotool Assembly

Creating nanomilled features with well-controlled shape and high dimensional accuracy necessitates a low-compliance structural loop between the nanotool and the sample. The AFM-based mechanical removal processes in the literature have utilized AFM probes, tips of which are located at the end of an AFM-cantilever. Due to the low-stiffness of the AFM-cantilevers that function as the connection element, the loop stiffness of such systems are very low, causing shape distortions and inaccuracies on the fabricated shapes.

In this work, we used an alternative approach, and attached the AFM tip (i.e., the nanotool) directly onto an acrylic post in a *reverse* configuration, where the tip is directly supported by the nanotool post as shown in Fig. 2.2. Since the compliant AFM cantilever is not used as the connection element, a high stiffness nanotool assembly is attained. During the assembly, first a UV-curable adhesive is applied on top of the micromachined protrusion

on the nanotool post. Under an optical microscope and using a pair of controlled tweezers, the AFM probe is brought to the top of the protrusion such that the bottom side of the cantilever below the AFM tip lays on the top of the protrusion. After curing of the UV adhesive, the AFM beam is snapped off close to the cantilevered end of the beam. This suspended portion of the AFM beam, referred to here as the *nanotool cantilever*, is utilized during contact detection and surface indication procedures (see below). The width and thickness of the nanotool cantilever is $45\text{ }\mu\text{m}$ and $1\text{ }\mu\text{m}$, respectively. The final length of the cantilever is approximately $200\text{ }\mu\text{m}$.

2.2.2 Obtaining Nanotool Motions

The rotary motions of the nanotool is obtained by attaching the nanotool post onto a three-axis piezoelectric-stack actuator (Physik Instrumente PI-123.01) shown in Fig. 2.2. This actuator consists of an assembly of two horizontal (x_p and y_p) shear-type piezoelectric stacks and a vertical (z_p) tension-type piezoelectric stack. The piezoelectric actuator is attached to a three axis manual stage (Newport 461-XYZ) that enables the coarse positioning of the nanotool prior to the nanomilling process.

2.2.3 Sample Attachment and Surface-Contact Indication

The feeding motions (and the depth prescription during the in-plane configuration) are obtained by moving the sample using a nanopositioning stage (Physik Instrumente P-611.3 NanoCube®) (see Fig. 2.2). The stage includes three flexure-based piezo-driven linear axes with built-in strain gage sensors for closed-loop position control. Using the nanopositioning stage, the sample can be positioned with 1 nm resolution and 5 nm rms repeatability (with the closed-loop position control) within $100\text{ }\mu\text{m}$ motion range in each of the three dimensions. An analog controller (Physik Instrumente E-664 Nanocube Controller) with proportional-integral (PI) architecture is used to control the stage motion in a closed-loop fashion. The trajectory of each axis is dictated by the supplying appropriate signals to the analog reference inputs of the controller with a sensitivity of $0.1\text{ V}/\mu\text{m}$. Closed loop control of the nanopositioning stage eliminates non-linear behavior due to its piezoelectric actuators such as hysteresis and creep.

Precise detection of the nanotool-surface contact is critical to fabricate accurate features. Furthermore, the initial surface is commonly inclined with respect to the nanopositioning stage axes. To address these issues, a surface-contact method described in Fig. 2.3 is employed. A piezoelectric (shaker) element (Physik Instrumente PL055.31) is placed under

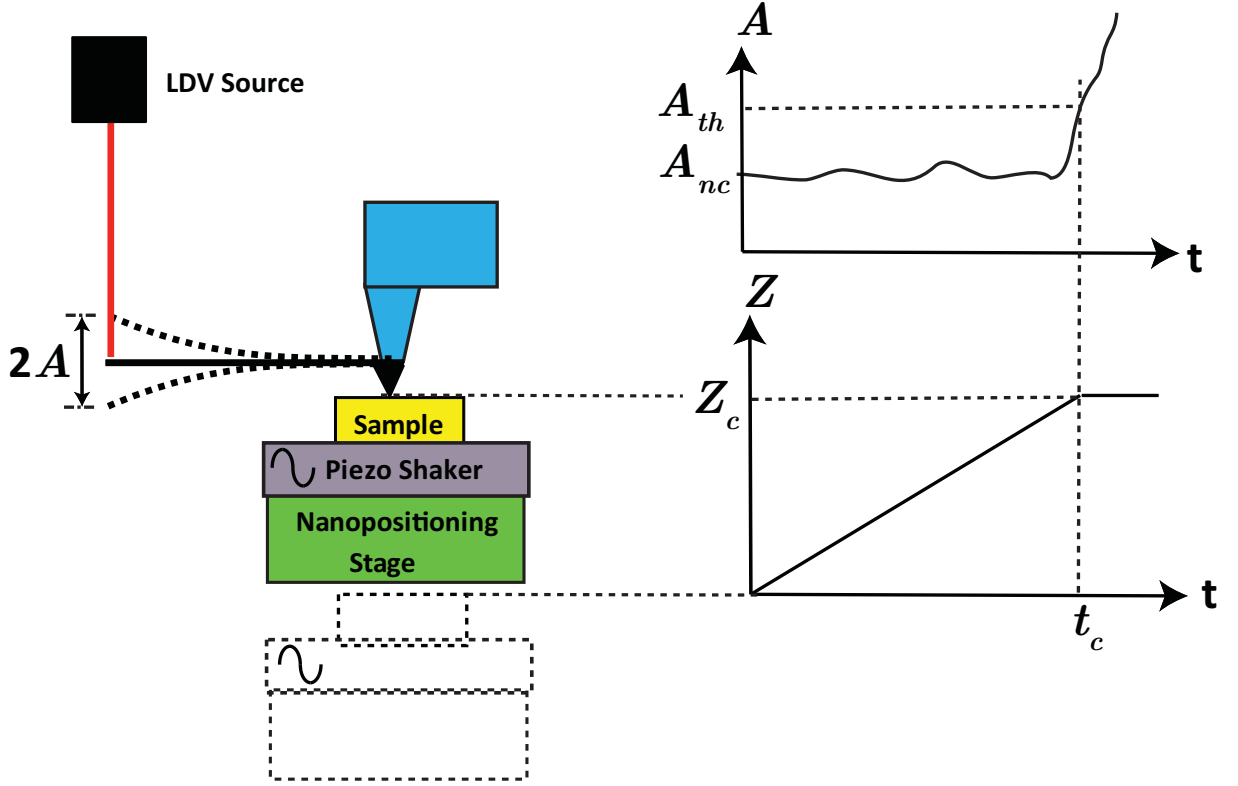


Figure 2.3: The contact detection method used for determination of nanotool-surface contact.

the sample, between the sample and the nanopositioning stage (see Fig. 2.2). The tip is approached to the sample surface to within less than $10\text{ }\mu\text{m}$ using the manual stages while observing through the optical side-microscope shown in Figure 2.2. Next, a Laser Doppler Vibrometer (LDV) system, which has a bandwidth of 350 kHz and a sensitivity of 50 nm/V when using the DD-500 decoder [59], is used to determine the first natural frequency (ω_{c1}) of the nanotool cantilever. Subsequently, the piezoelectric shaker element is vibrated at ω_{c1} with an amplitude less than 1 nm. The sample is then gradually (with 4 nm steps) approached to the nanotool using the nanopositioning stage while measuring the vibrations at the free end of the nanotool cantilever using the LDV system. A lock-in amplifier is used to detect the change in cantilever response amplitude at ω_{c1} . The contact is detected by the abrupt increase of vibration amplitude (A) above a threshold. Using this method for multiple points within the range of interest enables determination of initial sample-surface plane (see details below).

2.2.4 Data Acquisition and Process Control

To generate the analog driving signals for the nanotool rotations and nanopositioning stage motions, as well as to conduct the contact-detection procedure, a computer controlled data acquisition/signal generation system (National Instruments PXI-1033 chassis with PXI-6115 and PXI-6259 acquisition boards) is used. A LabVIEWTM-based program is written to control the system. This program is capable of managing nanomilling tasks for creating different feature geometries, such as surface indication, as well as calculation and generation of the driving signals for the piezoelectric actuator and nanopositioning stage. As outlined below, the software is also used during the characterization and alignment of nanomilling motions, including application of (linear and nonlinear) transformations between voltage inputs and motion responses. Power amplifiers (Khron Hite 7500) are used to supply the required voltage amplitude to the piezoelectric actuator.

2.2.5 Nanomilling Procedure

The nanomilling process is conducted through the following step-by-step procedure: First, the surface indication process is performed at different locations on the sample surface and a sample surface coordinate frame $[x_s, y_s, z_s]$ is defined (see below). The sample is then brought to contact with the nanotool. Second, according to the required nanomilling configuration, the LabVIEWTM program is used to calculate the signals that are required to prescribe the desired rotational motions of the nanotool within the sample-surface coordinate frame, and the data acquisition/signal generation system is used to supply the signals to the piezoelectric actuator through the voltage amplifiers. Third, the required depth (for a single pass) is imposed by moving the nanopositioning stage along the sample-surface normal z_s . Fourth, the feeding motions for the required feature geometry are obtained by providing the necessary inputs to the nanopositioning stage through the LabVIEWTM program. Continued feeding (and depth, as necessary) motions enables fabricating the feature with the desired geometry.

2.3 Characterization and Alignment of Nanomilling Motions

Successful execution of the nanomilling process necessitates well-controlled and coordinated motions of the nanopositioning stage and the nanotool motions with respect to the sample surface. This section describes the characterization and alignment of nanomilling motions. To facilitate determination and alignment of coordinate frames associated with the nanopo-

sitioning stage, nanotool motions and the sample surface, an LDV-based three-dimensional (3D) motion measurement system is developed. The sample-surface (plane) reference frame is then described with respect to a measurement reference frame. The physical motion axes of the nanopositioning stage are then measured, and the coordinate transformations between those axes and the sample-surface reference frame are determined to enable obtaining nanopositioning motions with respect to the sample surface. Next, a thorough characterization of nanotool (piezoelectric actuator) motions are completed using the measurement system at different voltage levels and frequencies, considering the nonlinear behavior of the piezoelectric-stack actuator. An approach is then developed to determine the necessary inputs to piezoelectric actuator to obtain the required nanotool motions. The details of each step are described below.

2.3.1 Three-Dimensional Motion Measurement System

Figure 2.4 illustrates the 3D measurement system. Each of the three fiber-optic LDV laser-beam carriers, which emit and receive the laser beams, is placed on a six-axis kinematic mount that facilitates orienting and moving the laser beam. Other long-range manual positioning stages are also attached under the six-axis mounts for coarse positioning of the lasers. An aluminum frame is constructed to enable attaching the vertical laser beam. The nanomilling system is assembled onto a breadboard, and placed at the center of the aluminum frame.

The alignment of three laser beams in mutually orthogonal configuration is crucial to the establishment of an absolute measurement frame within which the motions of the piezo-stack actuator is described. Upon the completion of the alignment procedure, each laser beam coincides with one of the axes of the established measurement reference frame $[x_m \ y_m \ z_m]$.

The alignment procedure uses the intensity of the returned laser beams that can monitored through the LDV system. When a laser beam is focused highly on a reflective surface, the intensity of the returned laser beam is directly correlated with the angular orientation of the laser beam with respect to the local surface normal: The intensity reaches its maximum level when the beam is perpendicular to the surface. To achieve mutual-orthogonality, the three laser beams are oriented to be perpendicular to the surfaces of a reference cornercube that consists of three mirror surfaces with better than 10 arc-sec perpendicularity. The cornercube is custom-fabricated by applying a reflective aluminum coating to the back side of a commercial retro-reflector. The returned beam intensity-based alignment method can be used align a laser beam perpendicular to a face of a cornercube in an uncertainty of \pm

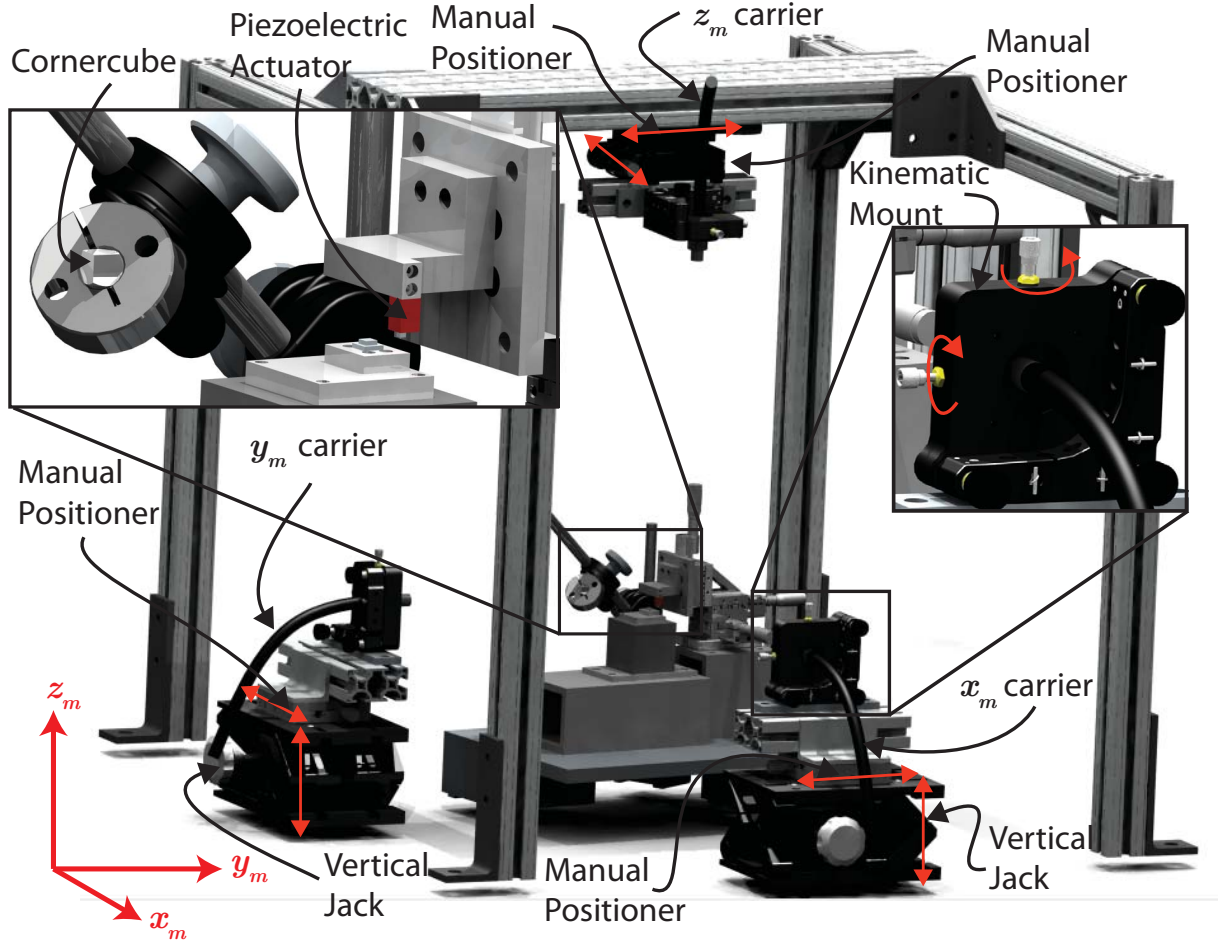


Figure 2.4: The LDV-based measurement system for 3D characterization of dynamic nanomilling motions.

0.04 degrees.

The procedure followed to position and align the laser beams can be summarized as follows: First, the piezo-stack actuator is placed within the measurement frame. The three laser beams are coarse-positioned to shine onto the acrylic post as shown in Figure 2.5 (a). Second, the piezo-stack actuator is removed, and the reference cornercube is placed within the measurement frame such that each of the three laser beams shines on one the mirror faces. The beams are then individually aligned to be perpendicular to their corresponding faces of the cornercube as shown in Figure 2.5 (b). This alignment is performed using kinematic mounts to rotate the beam carriers while monitoring returned beam intensity for each beam carrier. During this alignment procedure, the relative position changes of the laser beams due to rotation of beam carriers are compensated by the manual translation stages of the system. Finally, the piezo-stack actuator is brought back in the measurement frame

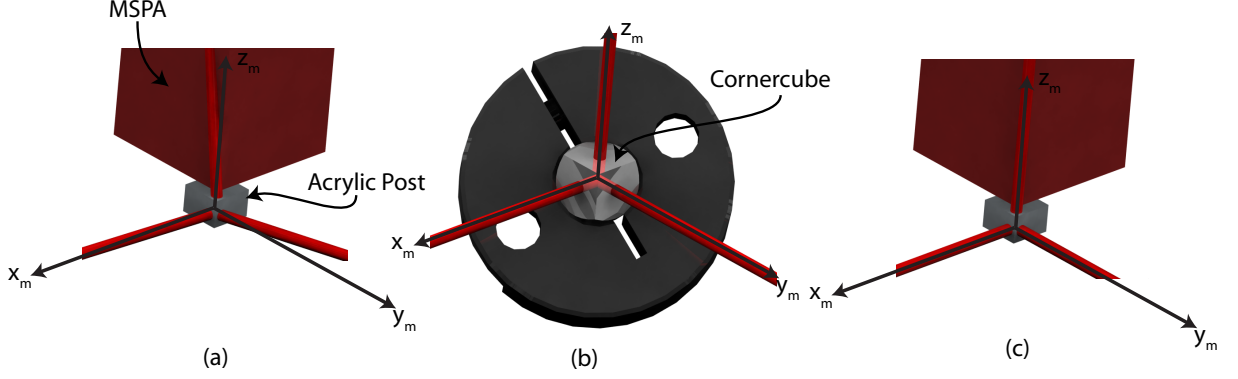


Figure 2.5: Alignment of three orthogonal laser beams (a) Course positioning of the beams on the acrylic post, (b) Perpendicular alignment of laser beams on cornercube faces (c) Final configuration of the laser beams.

and positioned such that the laser beams are at their determined measurement locations as shown in Figure 2.5 (c).

2.3.2 Sample Reference Frame

Since the nanomilling process proceeds on the sample surface, it is logical to define nanotool (rotary) motions and feeding/depth motions (provided by the nanopositioning stage) on a reference frame $[x_s, y_s, z_s]$ attached to the sample surface. Although the nanomilled feature can be created on a non-planar sample surface, we will limit our discussion to (nominally) planar sample surfaces for simplicity without loss of generality. The average surface roughness (Ra) of the PMMA samples used during this work was measured (using the Zygo NewView 7300 system) to be 2 nm.

To establish the *sample reference frame* $[x_s, y_s, z_s]$, the first step is to use the contact detection method (described above) to locate a (relatively large) number of points on the sample surface within the area in which the nano-scale feature will be fabricated. The 3D location of each of those points are recorded in the measurement reference frame $[x_m, y_m, z_m]$. Next, a least square fit is applied to fit the measured points to a plane in space, therefore determining the sample surface plane. The z_s axis is then selected along the normal to the sample surface plane. Subsequently, Gram-Schmidt [60] orthogonalization procedure is used to define x_s and y_s axes (from the initial orientations of x_m and y_m). Furthermore, the coordinate transformation between the sample reference frame and the measurement reference frame is determined and represented using the transformation matrix $\mathbf{T}_{s \rightarrow m}$ and its inverse $\mathbf{T}_{m \rightarrow s}$.

2.3.3 Characterization and Generation of the Nanopositioning Stage Motions

The motions of the nanopositioning stage dictates the shape of the nanomilled feature by providing the feeding motions and prescribing the removal depth during the nanomilling process. Therefore, a correlation between the sample reference frame and the nanopositioning stage motions must be established. Since the feeding motions and depth prescription considered in this work occur at very low frequencies, the dynamic effects and cross-talk between the motions of different axis of the nanopositioning stage are assumed to be negligible. Furthermore, a nanopositioning reference frame $[x_n, y_n, z_n]$, individual axes of which are aligned with the motion axes of the nanopositioning stage, is defined.

To determine orientation of the nanopositioning reference frame, a linear motion (30 μm long) is provided separately to each axis of the stage. Using the measurement system, the orientation of the resulting motion is measured in the measurement reference frame in three dimensions. Each of the x_n, y_n and z_n directions are then established by fitting straight lines to the obtained responses. A coordinate transformation between the measurement and nanopositioning reference frames is then established ($\mathbf{T}_{\mathbf{n} \rightarrow \mathbf{m}}$ and $\mathbf{T}_{\mathbf{m} \rightarrow \mathbf{n}}$). It should be noted that the nanopositioning reference frame obtained from this procedure was seen to be non-orthogonal. As a result, for desired feeding motion $f_s(t)$ prescribed in the sample reference frame, the required motion to be commanded to the nanopositioning stage $f_n(t)$ can be then be determined as

$$f_n(t) = \mathbf{T}_{\mathbf{m} \rightarrow \mathbf{n}} \mathbf{T}_{\mathbf{s} \rightarrow \mathbf{m}} f_s(t) \quad (2.1)$$

2.3.4 Dynamic Characterization of the Piezoelectric Actuator

To enable precise control of the nanotool motions (rotations) during the nanomilling process, the correlation between the driving signals and the response of the piezoelectric actuator must be well-characterized. Due to the nonlinear dynamic response, non-ideal motions of the piezoelectric elements (e.g., cross-talk, hysteresis), and inaccurate assembly of the piezoelectric stacks, the piezoelectric-stack actuators do not possess a set of well-defined, orthogonal physical axes of response. In other words, although there are three separate inputs to control the piezoelectric actuator motions in three dimensions, *both* the direction *and* the magnitude of the response vary (nonlinearly) with the frequency and amplitude of the excitation voltages. Therefore, instead of assigning a set of (constant) physical axes along which the motions will be commanded, the piezoelectric actuator is characterized as

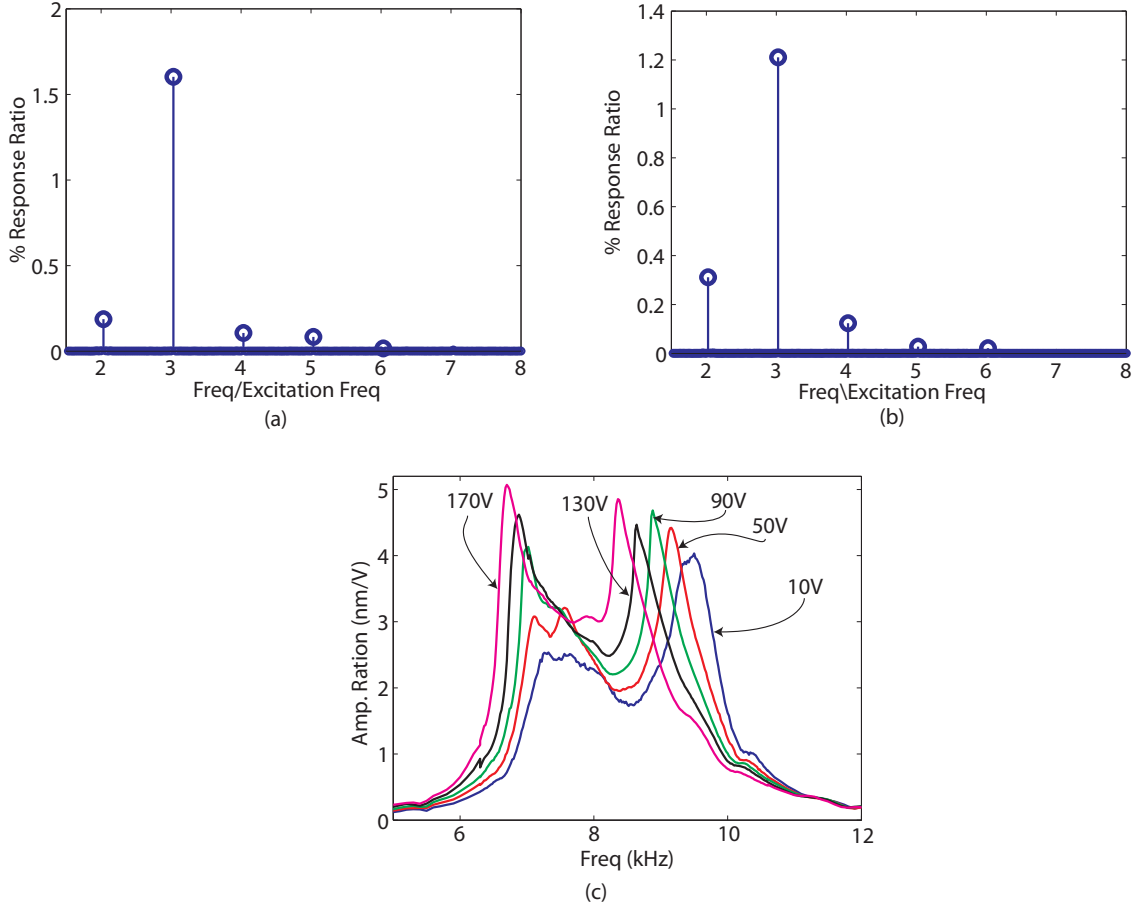


Figure 2.6: The nonlinear response characteristics of the piezoelectric actuator: The response at the harmonics of the excitation frequency for (a) $\omega_{ex} = 3$ kHz, and (b) $\omega_{ex} = 4$ kHz; and (c) the frequency response function showing the effect of amplitude (excitation voltage) on the response at the excitation frequency for $\omega_{ex} = 3$ kHz.

a three input-three output dynamic system, where the inputs are the voltages to each of the three piezoelectric stacks, and the outputs are the displacement responses along the three axes of the measurement reference frame.

The piezoelectric stack was seen to exhibit two major types of nonlinearities: First, the piezoelectric actuator was seen to produce responses at both the excitation frequency and its harmonics. This is illustrated in Figs. 2.6(a) and 2.6(b) for single-frequency sinusoidal excitations at ω_{ex} to a single stack. The horizontal axis indicates the measured response frequency as the harmonics of the excitation frequency ω_{ex} , and the vertical axis is the ratio between the responses at each harmonic to that at the excitation frequency, both measured along one of the measurement axes.

Second, the response behavior (both amplitude and direction of the response at all

harmonics) was seen to vary with the amplitude of excitation (voltage). This is illustrated in Fig. 2.6(c), which shows the change of the frequency response characteristics for the response at the excitation frequency measured along a measurement axis for a single-stack excitation at different excitation amplitudes.

A comprehensive method for dynamic characterization and control of piezoelectric-stack actuators to obtain high accuracy nanotool motions is explained in detail in Chapter 3.

Chapter 3

Characterization of Three-Dimensional Dynamics of Piezo-Stack Actuators

Generation of accurate high-frequency nanotool rotations is critical for the implementation of the nanomilling process with high accuracy and repeatability. In this chapter, the comprehensive methodology for characterization and mathematical representation of the dynamic response of the piezo-stack actuators is presented. The technical contributions of this study, are a new method for accurate characterization and representation of three-dimensional dynamic motions of piezo-stack actuators and an in-depth experimental understanding on the characteristics of the non-linear dynamic motions of piezo-stack actuators.

3.1 Introduction

Driven by the recent advances in the nanotechnology [61, 62], precision engineering [57], and metrology [8] fields, there is a strong need for obtaining three-dimensional motions with nanometer-level accuracy within a broad range of frequencies. Piezoelectric actuators are commonly chosen to fulfill this need due to their capability of generating nano-scale motions with sub-nanometer resolution. To obtain long range and multi-dimensional motions, the piezoelectric actuators are assembled into stacks (see Fig. 3.1). Dynamic motions of the piezo-stack actuators are three-dimensional in nature due to their complex modes of deformation that strongly depend upon their mechanical assembly and boundary conditions. Although three-dimensional motions can be generated using multi-axis piezo-stack

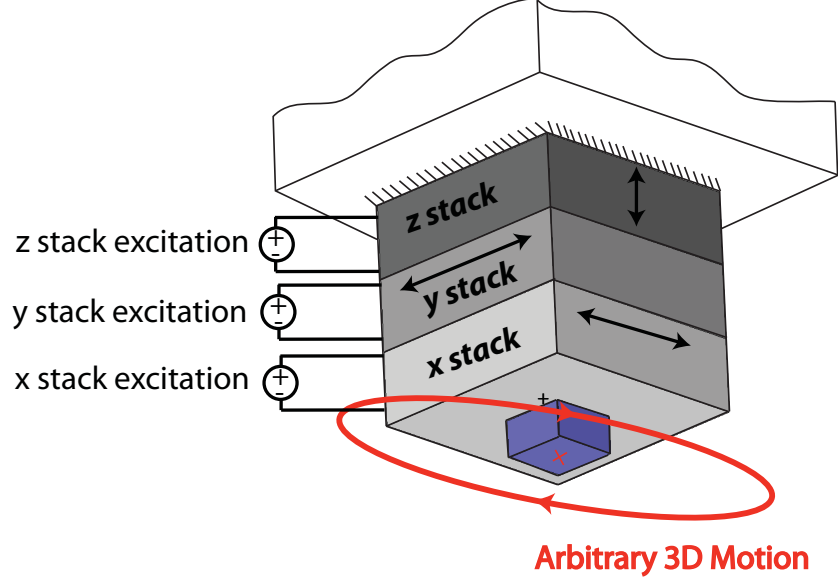


Figure 3.1: Depiction of a typical multi-axis piezo-stack actuator.

actuators, mechanical assembly, boundary conditions, and the non-linear dynamic behavior brings significant complexities. Therefore, the use of piezo-stack actuators for obtaining specific (e.g., elliptical) high-accuracy motions at high frequencies require a thorough understanding of their dynamic response characteristics. Specifically, techniques for accurate characterization and representation of non-linear behavior of piezoelectric actuators are needed.

In addition to the complex three-dimensional nature of their motions, the piezo-stack actuators have been shown to exhibit non-linear response behavior such as hysteresis, drift, creep, and time delay [63]. Methods of characterizing and controlling the *quasi-static* non-linear response behavior of piezo-stack actuators have been well established in the literature [64,65]. To understand the *dynamic* non-linear response behavior of the piezo-stack actuators, several modeling approaches have been proposed, including the rate-dependent hysteresis models [66,67] and non-linear lumped-parameter constitutive models [68,69]. The modeling efforts and accompanying experimental analysis have shown that the dynamic response of the piezo-stack actuators exhibit several characteristics common to non-linear dynamic systems, including (1) response to sinusoidal excitations include not only the excitation frequency, but also other frequencies, especially the harmonics of the excitation frequency [70], and (2) frequency response behavior of piezo-stack actuators strongly depend upon the excitation amplitudes [68,70]. To date, a comprehensive method for experimental characterization of the response behavior of piezo-stack actuators addressing those non-linear dynamic characteristics has not yet been devised.

In this chapter, we present an experimental method for characterization and representation of the three-dimensional dynamic response behavior of piezo-stack actuators. The characterization technique is based on accurate measurements of the response of piezo-stack actuators within the three-dimensional space using laser Doppler vibrometry (LDV). Subsequently, a system representation that extends the conventional FRF approach to describe the non-linear behavior is proposed. The following section describes the three-dimensional metrology system that is created to characterize the dynamic behavior of piezo-stack actuators. Next, the stepped-sine testing method used in this work is described. In this procedure, the piezo-stack actuators are sinusoidally excited within a range of excitation frequencies and amplitudes (to capture non-linear behavior) and the three-dimensional responses are acquired. The following section outlines the data analysis techniques and the extended-FRF-based representation approach. To demonstrate the presented characterization and representation approach, two three-axis piezo-stack actuators are then tested. Finally, an experimental analysis of the measurement errors is conducted to assess the fidelity of the characterization method.

3.2 Experimental Methods

This section describes the experimental methods used for the dynamic characterization of piezo-stack actuators. To enable capturing the non-linear dynamic behavior, the stepped-sine testing method is adopted [71]. The responses obtained during the experiments are measured along three measurement axes. Furthermore, the measured responses are analyzed in the frequency domain within a broad frequency range to capture the wide-band response behavior due to the non-linearity.

Each stepped-sine test consists of a number of excitation steps, during which sinusoidal excitations are supplied to one of the stacks of the piezo-stack actuator. The excitation frequency is varied incrementally within the predetermined excitation frequency range, while keeping the excitation amplitude constant. At each excitation step, the excitation with the prescribed amplitude and frequency is applied for a predetermined duration, and the motions of the piezo-stack actuator is measured along the three measurement reference frame axes, as depicted in Fig. 3.2. The generated excitation signal is also measured simultaneously to provide a phase reference. A predetermined dwell time is used in the beginning of the acquisition to discard the transient response. At each step, the average response from four repetition tests is used to eliminate unbiased noise. The entire stepped-sine testing procedure is repeated for different excitation amplitudes to capture the dependence of

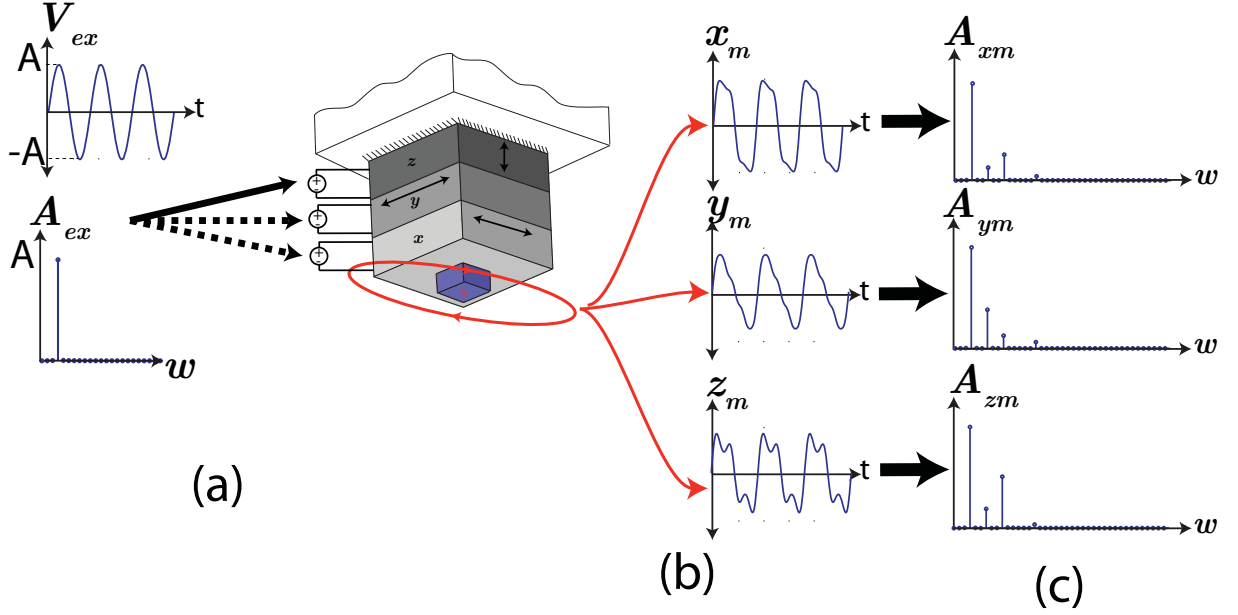


Figure 3.2: Description of the stepped-sine testing method: (a) A sinusoidal voltage with a specific amplitude is supplied to one of the stacks of the actuator at the selected excitation frequency, (b) the piezo-stack actuator's response is measured in 3D using the three laser beams, and (c) the time-domain responses in each of the three (measurement) reference axes are converted to frequency domain through FFT.

dynamic response behavior upon the excitation amplitude.

The measured responses are processed in the frequency domain through a fast Fourier transform (FFT) algorithm to determine their amplitude and relative phase. The lower bound of the frequency range is selected to be 500 Hz so that the low frequency drift and noise introduced by the LDV system are excluded from the response. The frequency domain calculations are performed using a Hanning window to avoid spectral leakage.

In the conventional application of the stepped-sine testing procedure, a test with a relatively large frequency step is first conducted. To obtain more accurate data, additional tests with smaller excitation frequency increments are then conducted within the frequency ranges where the frequency response exhibit rapid changes, i.e., in the vicinity of resonance and anti-resonant peaks. This refinement procedure commonly considers the response behavior only at the excitation frequency. In other words, the refinement is done based on the fundamental (linear) FRF only. As stated above, however, the dynamic response of piezo-stack actuators include responses not only at the excitation frequency, but also at the harmonics of the excitation frequency. In this case, the refinement procedure should include an analysis of the response at both the excitation frequency and its harmonics. Therefore, as depicted in Fig. 3.3, those regions that produce peaks in the higher-harmonic responses

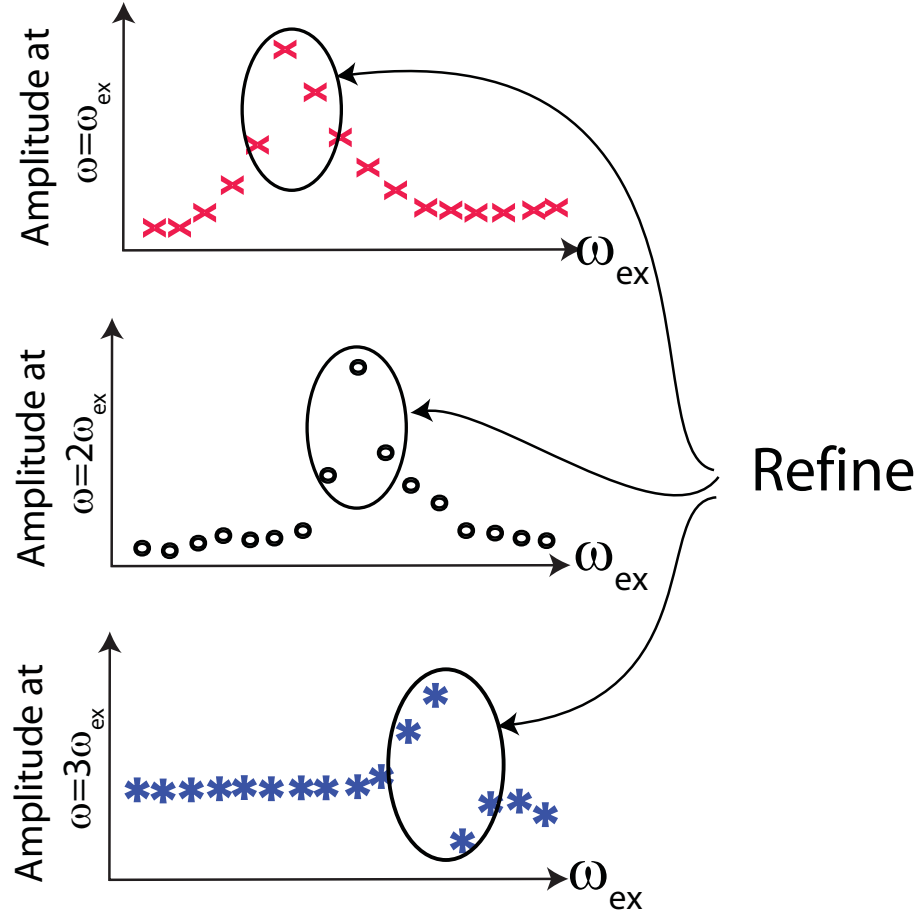


Figure 3.3: Description of the frequency refinement procedure: Response occurs not only at the excitation frequency, but also its harmonics. Those regions in which the rapid changes occur on the response either at the excitation frequency or at its harmonics are refined using smaller excitation-frequency increments.

should also be refined.

Each stepped-sine test is initially executed with a frequency increment of 100 Hz within the entire frequency range. As a result of this preliminary test, the response amplitudes (along each of the three measurement frame axes) measured at the harmonics of the excitation frequencies can be plotted as a function of the excitation frequency, as illustrated in Fig. 3.3. Subsequently, for those regions that exhibit rapid changes (peaks) on the responses measured at the excitation frequency and its harmonics are refined by successively reducing the frequency increments to 20 Hz and 4 Hz.

3.3 Analysis of the Experimental Data

As a result of the stepped-sine tests, amplitude and phase (relative to the excitation) of the response along the three measurement axes are obtained as functions of the response frequency, excitation frequency and excitation amplitude. The amplitude and phase of the response measured along the reference frame axis k at frequency ω for a sinusoidal excitation to the stack i are denoted as $A_{ki}(\omega, \omega_{ex}, V_i)$ and $\Phi_{ki}(\omega, \omega_{ex}, V_i)$, respectively, where V_i is the excitation amplitude, and ω_{ex} is the excitation frequency. The response amplitude is measured in the units of nanometers, and the relative phase is measured in radians. For a multi-axis piezo-stack actuator with n independently-controlled stacks, the amplitude and relative phase can be described by $n \times 3$ matrices, each element of which corresponds to the response along the measurement axis k to the excitation of stack i .

3.3.1 Frequency Domain Categorization of the Response

The dynamic response characteristics of a piezo-stack actuator within predetermined excitation amplitude and frequency ranges can be fully defined by the aforementioned amplitude and relative phase functions. Further insight on the response characteristics may be obtained by categorizing the response based on its frequency content. The response to a sinusoidal excitation at ω_{ex} produces *harmonic* and *non-harmonic* response components. The n^{th} *harmonic response component* is defined as the single-tone response at the n^{th} harmonic of the excitation frequency ($n\omega_{ex}$). The first harmonic response component is referred to as the fundamental response component as it corresponds to the response at the excitation frequency. The response at the remaining frequencies can be classified as the *non-harmonic response components*, which can also be categorized into two groups: A *specific* non-harmonic response component is defined as a single-tone response component measured at a frequency other than the harmonics of the excitation frequency. The *wide-band* non-harmonic response component is defined as the response with a wide-band nature throughout the measurement frequency range excluding the harmonics of the excitation frequency and the frequencies at which the specific non-harmonic responses are observed.

3.3.2 Power Analysis

For both understanding its dynamic behavior and efficiently controlling its motions, the dynamics of a piezo-stack actuator should be presented using the simplest possible representation. The response component categorization can facilitate simplifying the representation

of the piezo-stack actuator dynamics.

An approach to determine the contribution of each response component to the total dynamic response is to perform a power analysis. The signal power of a given dynamic response can be calculated by integrating its *power spectral density* (PSD) over the desired frequency range. Given the response amplitude function (A_{ki}), the power spectral density of the response measured along a single axis can be calculated as [72]

$$S_{ki}(\omega, \omega_{ex}, V_i) = \frac{(A_{ki}(\omega, \omega_{ex}, V_i))^2}{\Delta\omega \times ENBW}, \quad (3.1)$$

where $\Delta\omega$ is the measurement frequency increment, and $ENBW$ is the *equivalent noise bandwidth* for the Hanning window [73].

The power of the response within a given frequency range $[\omega_1, \omega_2]$ can be calculated as :

$$P_{ki}^{[\omega_1, \omega_2]}(\omega_{ex}, V_i) = \int_{\omega_1}^{\omega_2} S_{ki}(\omega, \omega_{ex}, V_i) df \quad (3.2)$$

where i indicates the excited piezo-stack. The integral in the Eq. (3.2) is calculated through trapezoidal integration.

The total measured power of the response (P_{ki}^{tot}) is calculated by performing the above integration within the entire measurement frequency range. Although the fundamental and harmonic response components are single frequency components, the use of Hanning window causes a leakage of response power to its neighboring frequencies. Accordingly, the power of the n^{th} harmonic response component ($P_{ki}^{(n)}$) can be calculated by integrating the response PSD within the frequency band $n\omega_{ex} \pm 3\Delta\omega$ to capture the main lobes of the Hanning window (leakage range) in the frequency domain [72]. The power of the non-harmonic response component (P_{ki}^{nh}) can be calculated by subtracting the harmonic response components from the total measured power of the response as

$$P_{ki}^{nh}(\omega_{ex}, V_i) = P_{ki}^{tot}(\omega_{ex}, V_i) - \sum_{n=1}^{n_{max}} P_{ki}^{(n)}(\omega_{ex}, V_i), \quad (3.3)$$

where n_{max} is the highest harmonic of the excitation frequency within the measurement frequency range.

The contribution of a specific response component to the total dynamic response can be

calculated by defining a percent contribution (PC_i) as

$$PC_i(\omega_{ex}, V_i) = \frac{\sum_{k=x_m, y_m, z_m} P_{ki}(\omega_{ex}, V_i)}{\sum_{k=x_m, y_m, z_m} P_{ki}^{tot}(\omega_{ex}, V_i)} \times 100, \quad (3.4)$$

where i is the excited stack, k is the measurement axis, and $P_{ki}(\omega_{ex}, V_i)$ is the power at a specific response component.

Eq. (3.3) is used to calculate the total non-harmonic response power that includes the power corresponding to both the specific and the broad-band non-harmonic response components. The significance of specific non-harmonic response components can be determined through calculation of the spectral flatness [74] of the power spectral density excluding harmonic response components. If the calculated spectral flatness is above a predetermined threshold value, the specific non-harmonic response components can be assumed to be negligible.

By observing the percent power contributions of different response components, dynamic response within the excitation frequency and amplitude ranges of interest, can be represented by only a limited a number of response components. Alternatively, results of the power analysis could be used to select the operational ranges of excitation frequency and amplitude for the tested actuator, depending on the desired response behavior (such as low contribution of higher harmonic components).

3.3.3 Frequency Response Representations for the Dynamic Response of Piezo-Stack Actuators

The excitation-response relations for linear systems are represented by *frequency response functions* (FRFs), which are complex functions of excitation frequency. The magnitude of the FRFs represents the ratio of the response and the excitation amplitudes, and the phase of the FRFs indicate the relative phase between the response and the excitation. For many non-linear systems, the definition of FRFs are extended to higher order FRFs that are obtained through Volterra Series representations [75, 76]. These representations completely address the aforementioned non-linear dynamic response characteristics, such as the wide-band response and excitation amplitude dependence. However, their application to experimental characterization are limited due to their complexity [77].

In this work, we propose a new practical approach for representation of the non-linear dynamic behavior of piezo-stack actuator. In this approach, the linear FRF definition is extended to describe each identified response component individually at different levels of the

excitation amplitudes. The FRFs corresponding to the harmonic response components are referred to as n^{th} *harmonic FRFs* (nFRFs), which are complex functions of excitation frequency and amplitude, magnitude and phase of which are the amplitude ratio and relative phase between the n^{th} harmonic response component and the excitation. The first harmonic FRF is referred to as the fundamental FRF. A broad-band *non-harmonic frequency response function* (nhFRF) is defined as a real function of excitation frequency and amplitude that is equal to the ratio between the broad-band amplitude of the non-harmonic response component and the excitation amplitude. For the cases where specific non-harmonic response components are not negligible, frequency response function definitions similar to nFRFs can be made for those components.

Calculation of nFRFs and nhFRFs requires determination of amplitudes and phases corresponding to the harmonic and non-harmonic response components. The amplitude of a response component is equal to the square root of its response power i.e., $A_{ki}^{(n)}(\omega_{ex}, V_i) = \sqrt{P_{ki}^{(n)}(\omega_{ex}, V_i)}$ and $A_{ki}^{nh}(\omega_{ex}, V_i) = \sqrt{P_{ki}^{nh}(\omega_{ex}, V_i)}$. The phase of a harmonic response component can be calculated from the measured relative phase as $\Phi_{ki}^{(n)}(\omega_{ex}, V_i) = \Phi_{ki}(\omega, \omega_{ex}, V_i)|_{\omega=n\omega_{ex}}$.

Accordingly, nFRFs and nhFRFs of a multi-axis piezo-stack actuator can be calculated as

$$G_{ki}^{(n)}(\omega_{ex}, V_i) = \frac{A_{ki}^{(n)}(\omega_{ex}, V_i)}{V_i} e^{j\Phi_{ki}^{(n)}(\omega_{ex}, V_i)}, \text{ and} \quad (3.5)$$

$$G_{ki}^{nh}(\omega_{ex}, V_i) = \frac{A_{ki}^{nh}(\omega_{ex}, V_i)}{V_i}, \quad (3.6)$$

where $G_{ki}^{(n)}$ and G_{ki}^{nh} are the nFRF and nhFRF corresponding the response along the reference frame axis k to the sinusoidal excitation provided to the stack i , respectively. For a multi-axis piezo-stack actuator, the determined frequency response functions can be expressed as $n \times 3$ matrices, where n is the number of independently controlled stacks of the actuator.

The nFRFs and nhFRFs can be used to obtain the components of the response of a piezo-stack actuator to a sinusoidal excitation. The total response can then be estimated by the summation of the response components included in the simplified response representation. Furthermore, FRFs and nhFRFs provide detailed information regarding the dynamic response characteristics within various ranges of the excitation frequency and amplitude.

Table 3.1: Parameters used during the characterization of the piezo-stack actuators.

Excitation Frequency Range (kHz)	1 \cdots 25
Excitation Amplitudes (V)	10, 60, 110, 160
Excitation Amplitudes (V) (z stack of Actuator 2)	1, 6, 11, 16
Sampling Rate(kHz)	400
Measurement Frequency Range (kHz)	0.5 \cdots 200
Excitation Duration (s)	0.6
Dwell Time (s)	0.1
Measurement Frequency Resolution (Hz)	2

3.4 Application of the Characterization Method

This section demonstrates the application of the characterization method for the dynamic response of piezo-stack actuators.

To demonstrate the application of the presented method, two different three-axis piezo-stack actuators (Actuators 1 and 2) are tested. The actuators consist of three stacks, which are denoted as x , y and z stacks. The x and y stacks of both actuators are shear mode actuators, the z stack of both actuators are normal-mode actuators. Actuator 1 is a commercially available three-axis piezo-stack actuator (Physik Instrumente PICA Shear Actuator P-123.01). Actuator 2 is built by assembling two-axis (XY) piezo-stack actuator (Physik Instrumente PICA Shear Actuator P-112.01) on a single axis normal piezo-stack actuator (Physik Instrumente PICMA Chip Actuator PL-055.30).

The experimental parameters used during the stepped-sine tests are given in Table 3.1. The z stack of Actuator 2 exhibits approximately ten times larger displacements than the other tested stacks do. Accordingly, the excitation voltages of 1, 6, 11 and 16 V is used for this specific stack.

3.4.1 Results of the Stepped-Sine Testing

Figure 3.4(a) illustrates a typical response amplitude data (in logarithmic scale) that is acquired through stepped-sine testing approach. The response amplitude is obtained by exciting the x stack of the Actuator 1 with an amplitude of 160 V and measuring the responses along the x_m axis (i.e., $A_{ki}(\omega, \omega_{ex}, 160V)$ for $k = x_m$ and $i = x$). The axis labeled as ω represents the measurement frequency (only the 1-25 kHz range is shown), and the axis labeled as ω_{ex} represents the excitation frequency. The response amplitude obtained for the excitation step with the excitation frequency of 3 kHz is shown in Fig. 3.4(b). Similar plots can also be generated for the phase of the measured responses.

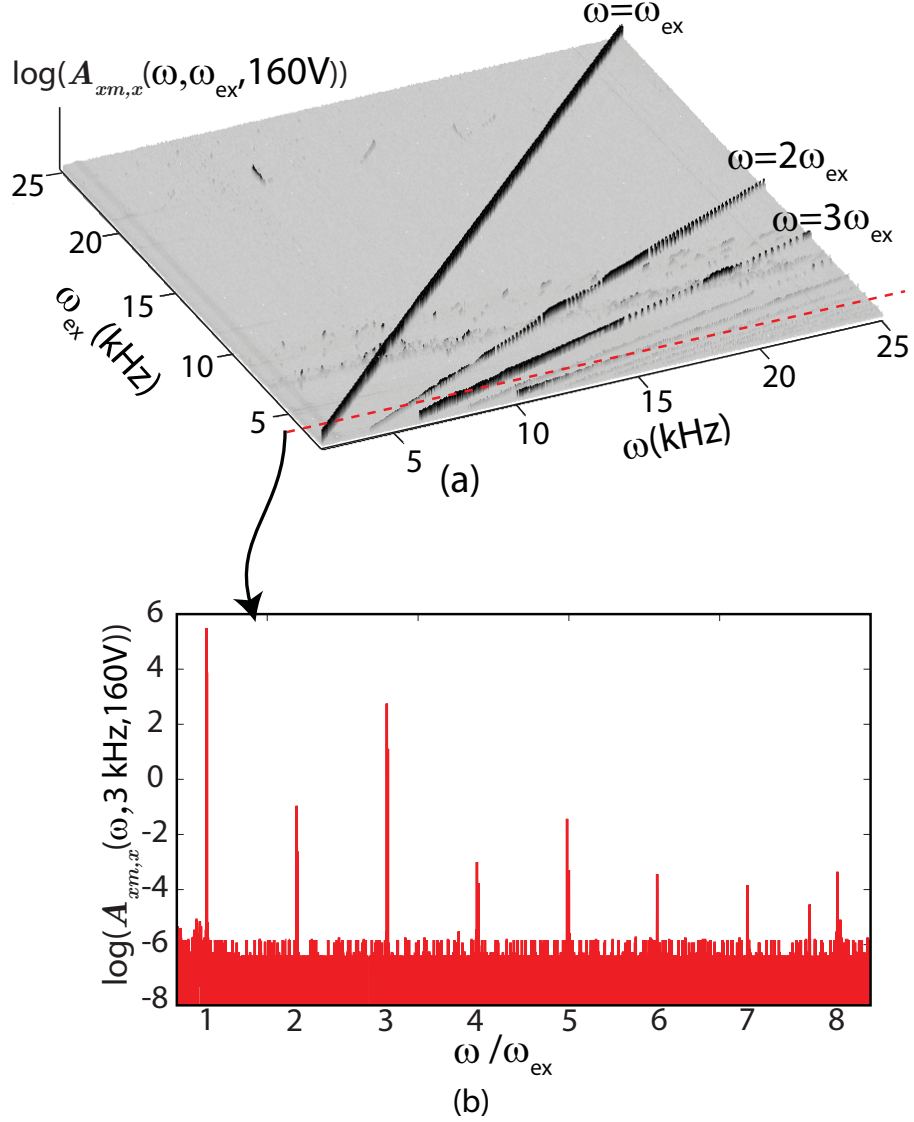


Figure 3.4: (a) A typical response amplitude (in logarithmic scale) as function of the excitation and response frequencies, and (b) the response amplitude corresponding to a particular excitation step at $\omega_{ex} = 3$ kHz, indicating the responses at the harmonics of the excitation frequency.

The distinct lines with higher amplitudes seen in Fig. 3.4(a) corresponds to amplitudes of the harmonics of the excitation frequency. In Fig. 3.4(b), the measurement frequency is normalized with respect to the excitation frequency to highlight the response observed at the harmonics of the excitation frequency. It can be seen that the response amplitude has distinct peaks at the integer multiples of the excitation frequency. Those peaks correspond to the single-tone harmonic response components.

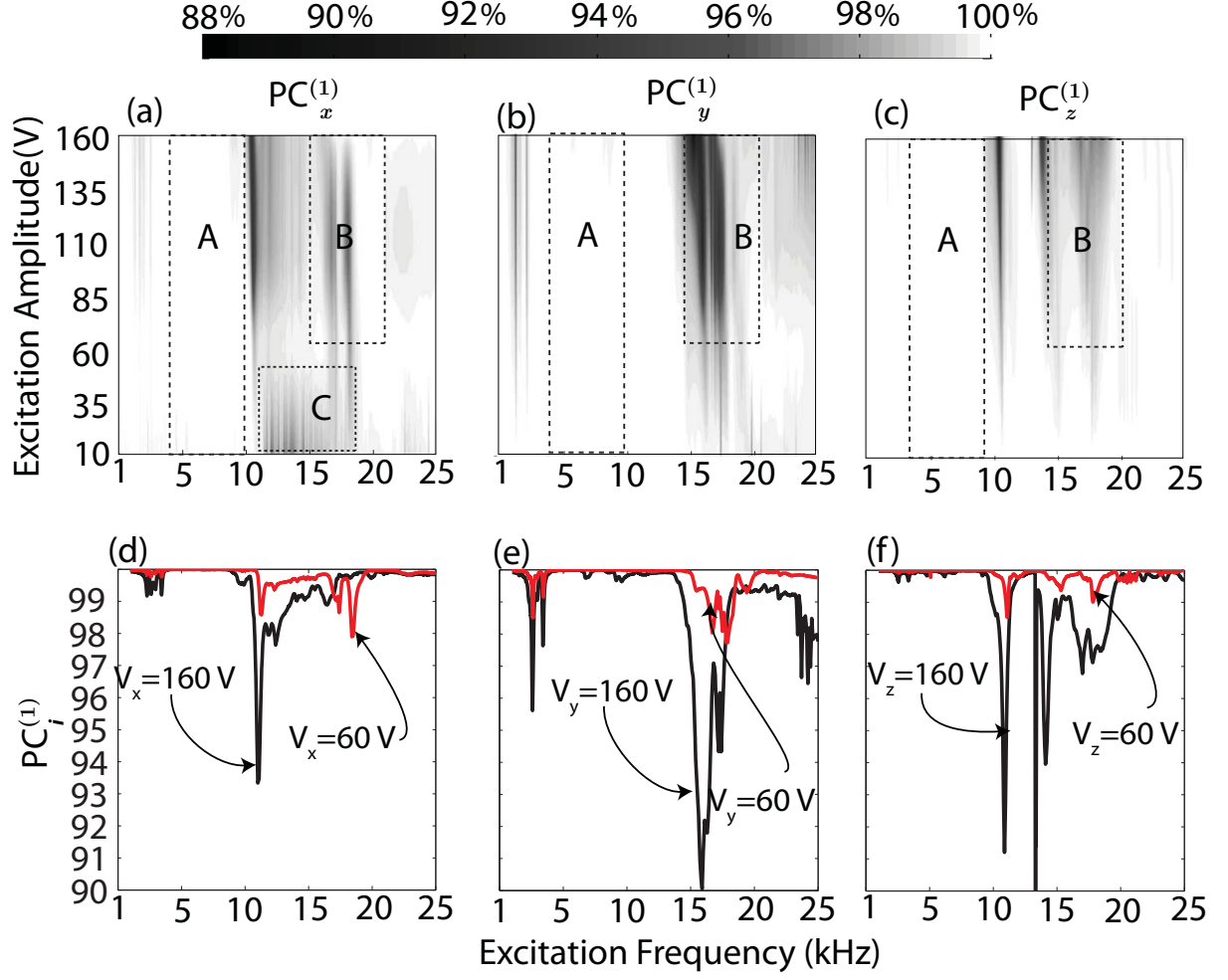


Figure 3.5: Percent contribution of the fundamental response component to the total response power for Actuator 1: (a)-(c) As a function of both the excitation frequency and amplitude to excitation of stacks x , y and z , respectively; (d)-(f) as a function of the excitation frequency at excitation amplitudes of 160 V and 60 V given for responses to excitation of stacks x , y and z , respectively.

3.4.2 Power Analysis

In this section application of the power analysis is demonstrated. For this purpose, percent contributions (PC_i) of each response component are plotted as a function of excitation frequency and amplitude.

The percent contribution of the fundamental response component as a function of the excitation frequency and amplitude ($PC_i^{(1)}(\omega_{ex}, V_i)$) for Actuator 1 is given in Fig. 3.5(a)-(c). Each of the three plots presents the data obtained when a different stack of the actuator is excited. The data corresponding to the excitation amplitudes between the tested excitation amplitude values is obtained through spline interpolation. Fig. 3.5(d)-(f) gives

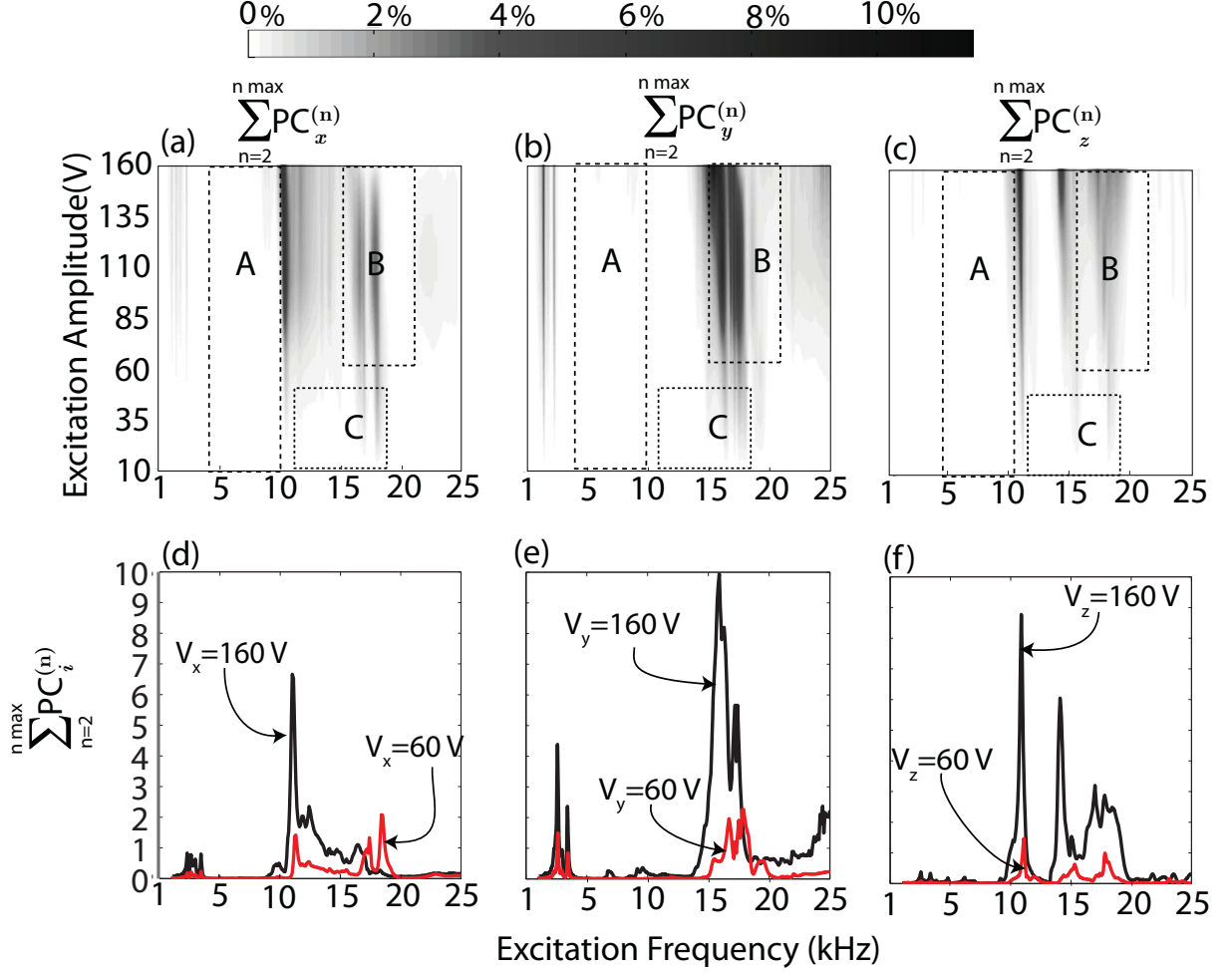


Figure 3.6: Cumulative percent contribution of the higher harmonic response components to the total response power for Actuator 1: (a)-(c) As a function of both the excitation frequency and amplitude to excitation of stacks x , y and z , respectively; (d)-(f) as a function of the excitation frequency at excitation amplitudes of 160 V and 60 V given for responses to excitation of stacks x , y and z , respectively.

the percent contributions for the excitation amplitudes of 60 V and 160 V as a function of excitation frequency. Similarly, the cumulative percent contribution of the higher harmonic response components ($\sum_{n=2}^{n_{\max}} PC_i^{(n)}(\omega_{ex}, V_i)$) and the non-harmonic response component ($PC_i^{nh}(\omega_{ex}, V_i)$) are presented by Figs. 3.6 and 3.7, respectively.

The contribution of the fundamental response component above 90% of the total power for the tested excitation frequency and amplitude ranges. However, the amount of contribution of various response components varies with excitation frequency and amplitude. The region marked as A in Figs. 3.5 and 3.6 corresponds to the excitation frequency and amplitude ranges of 5 kHz to 10 kHz and 10 V to 160 V, respectively. Within this region, the

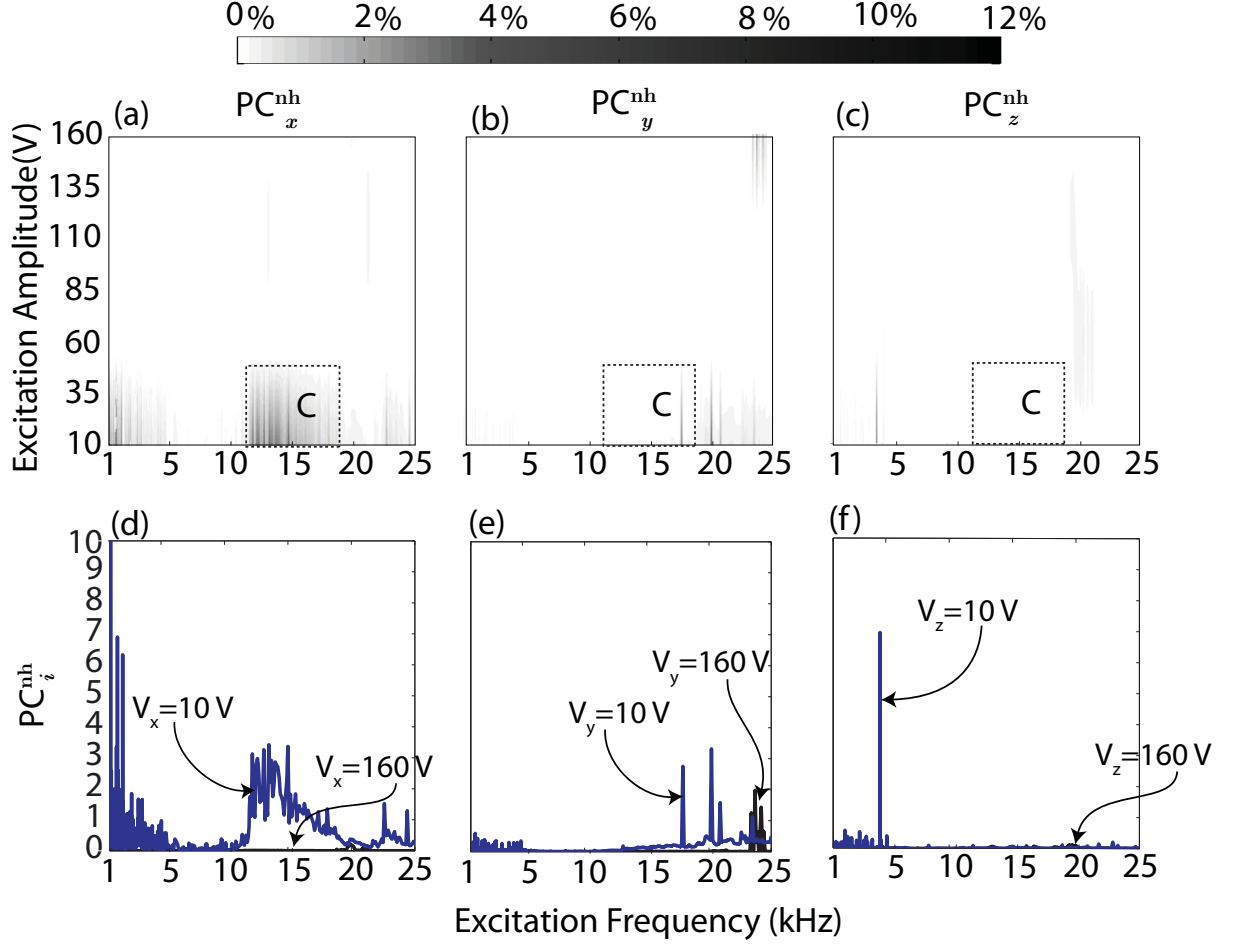


Figure 3.7: Percent contribution of the non-harmonic response component to the total response power for Actuator 1: (a)-(c) As a function of both the excitation frequency and amplitude to excitation of stacks x , y and z , respectively; (d)-(f) as a function of the excitation frequency at excitation amplitudes of 160 V and 60 V given for responses to excitation of stacks x , y and z , respectively.

percent contribution of the fundamental response component is more than 99.03 %, 99.63 % and 98.88 % for the excitation of the x , y and z stacks, respectively. Accordingly, when used within region A, the dynamic response of Actuator 1 can be accurately represented by only the fundamental response component.

Region B corresponds to the excitation frequency and amplitude ranges of 15 kHz to 20 kHz and 60 V to 160 V, respectively. In this region, the cumulative percent contribution of higher harmonic response components reaches 3.37 %, 9.94 % and 3.19 % for x , y and z stacks, respectively. Therefore, accurate representation of the dynamic response within this region requires inclusion of higher harmonic response components.

Region C corresponds to the excitation frequency and amplitude ranges of 11 kHz to 19

Table 3.2: Percent contributions of harmonic response components corresponding to the excitation of the y stack with an excitation frequency and amplitude of 16 kHz and 160 V, respectively.

$PC_y^{(2)}$	$PC_y^{(3)}$	$PC_y^{(4)}$	$PC_y^{(5)}$	$PC_y^{(6)}$	$PC_y^{(7)}$	$PC_y^{(8)}$
6.172	3.7433	0.0001	0.0259	4.1573E-5	0.0001	1.7519E-5

kHz and 10 V to 50 V, respectively. The percent contribution of the non-harmonic response component is up to 4 % in this region, particularly when exciting the x stack. Therefore, the dynamic response representation in this range should include all of the fundamental, harmonic and non-harmonic components.

Generally speaking, the percent contribution of the harmonic response components reduces with the increasing harmonic number. To determine which harmonics are critical to include in describing the dynamic behavior of the piezo-stack actuators, relative contributions of individual harmonic response components can be studied. As an example, Table 3.2 presents the percent contributions corresponding to different harmonic response components for the excitation of y stack at 16 kHz frequency and 160 V amplitude. It is important to note that, for this case, the cumulative percent contribution of the higher harmonics is as high as 10 %. The contribution of the harmonic response components decrease considerably for harmonic numbers above three. For this particular case, cumulative percent contribution of the first three harmonic (i.e. fundamental, second and the third harmonic) response components is equal to 99.96 %.

The percent contributions of the fundamental response component is given for Actuator 2 in Fig. 3.8. For this actuator, the contribution of the fundamental component is as low as 88% within region given by the excitation frequency range of 5 kHz to 10 kHz and the excitation amplitude range of 60 V to 160 V (6 to 10 V for the z stack). In this region, the contribution of higher harmonic response components is higher compared to rest of the excitation frequency and amplitude ranges. For the case where the z stack is excited, the contribution of the fundamental component lower for excitation amplitudes less than about 4 V compared to higher excitation amplitude range. This decrease is due to the increase of the non-harmonic response component contribution.

3.4.3 Analysis of extended-FRFs

This section presents the extended FRFs (nFRFs and nhFRFs) calculated using the experimental characterization data. Through the examination of the obtained extended-FRFs, observations are made regarding the dynamic response characteristics of the tested piezo-

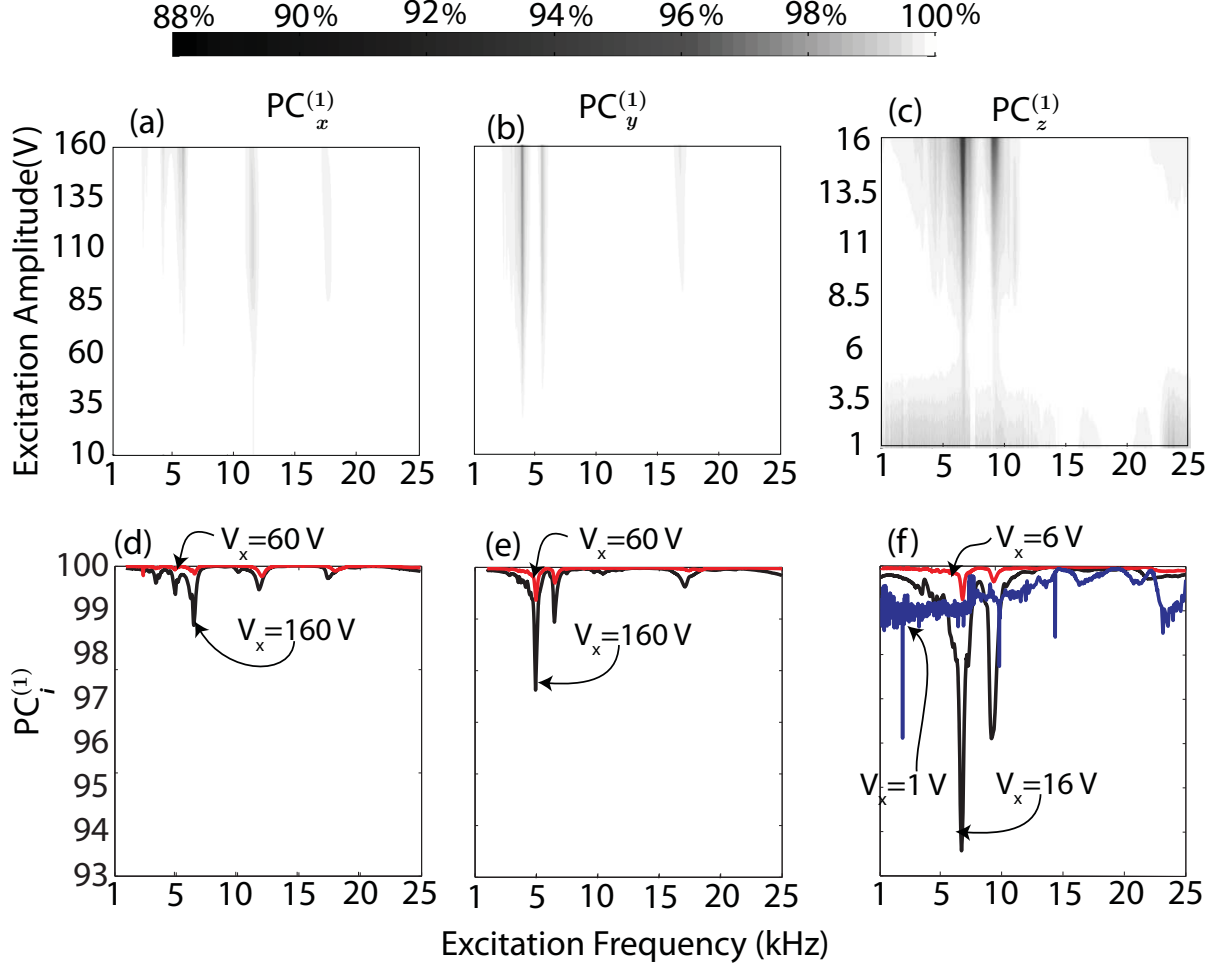


Figure 3.8: Percent contribution of the fundamental response component to the total response power given for Actuator 2: ((a)-(c) As a function of both the excitation frequency and amplitude to excitation of stacks x , y and z , respectively; (d)-(f) as a function of the excitation frequency at excitation amplitudes of 160 V and 60 V given for responses to excitation of stacks x , y and z , respectively.

stack actuators, particularly the behavior of different response components within different ranges of excitation frequencies and amplitudes.

Figs. 3.9(a)-(c) show the amplitude ratio of the fundamental FRFs for Actuator 1 as a function of excitation frequency and amplitude (i.e $\mathbf{G}_{k,x}^{(1)}(\omega_{ex}, V_x)$ for $k = x_m, y_m, z_m$) in logarithmic scale when exciting the x stack. The values of the amplitude ratio between the tested excitation amplitudes are calculated by spline interpolation. Figures 3.9 (d)-(f) present the amplitude ratio as a function of excitation frequency at the tested amplitude levels. The variation of the fundamental FRFs with the excitation amplitude is a clear indication of the non-linear dynamic behavior. The black and white strips represent the resonance and anti-resonance peaks corresponding to the fundamental response component.

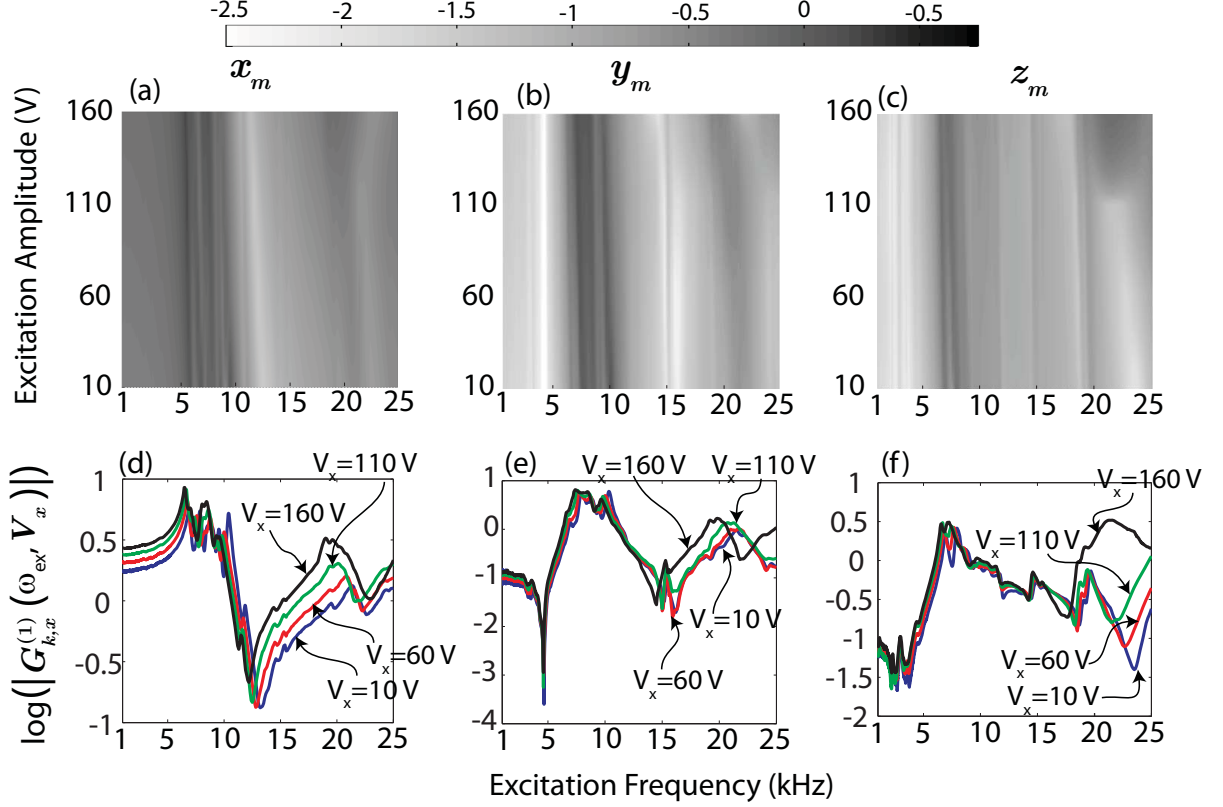


Figure 3.9: Amplitude ratios of fundamental nFRFs corresponding to the excitation of the x stack for Actuator 1: (a)-(c) As a function of the excitation frequency and amplitude measured along x_m , y_m and z_m directions, respectively, and (d)-(f) as a function of the excitation frequency at the tested excitation amplitudes measured along x_m , y_m and z_m directions, respectively.

Observations can be made regarding the three-dimensional nature of the dynamic piezo-stack motions through fundamental FRFs. It can be seen that within the 1–5 kHz excitation frequency range, the amplitude of the fundamental response component along the x_m axis is an order of magnitude higher compared to the other axes. This indicates that the motion generated by the excitation of the x stack is aligned mostly with the x_m axis within this excitation frequency range. At higher excitation frequencies, significant changes in the response direction can be observed. For instance, within the 5 kHz to 10 kHz range, the amplitude ratios measured along the x_m and y_m are comparable, which indicates that the motion makes an (close to 45°) angle with the x_m direction. Therefore even though the quasi-static response of a piezo-stack actuator can be considered one-dimensional, for operation at higher frequencies, three-dimensional nature should be taken into consideration.

Amplitude ratios of nFRFs corresponding to the first three harmonic response compo-

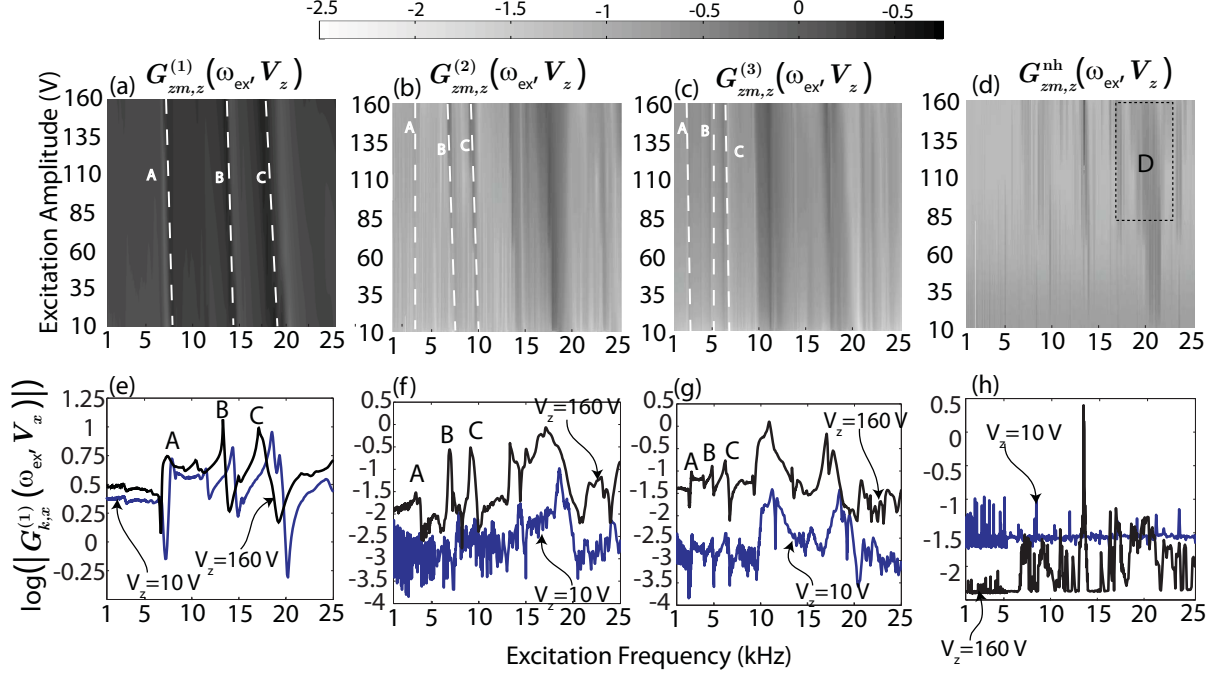


Figure 3.10: Amplitude ratios of to the first three nFRFs and nhFRF corresponding to the excitation of z stack and response along the z_m axis for Actuator 1: (a)-(d) As a function of the excitation frequency and amplitude. (e)-(h) as a function of the excitation frequency for the excitation amplitudes of 10 V and 160 V.

nents, as well as the amplitude ratio of nhFRF, for Actuator 1 are given in Figures 3.10 (a)-(d) in logarithmic scale, which correspond to the excitation of the z stack and the response measured along the z_m axis. The amplitude ratios calculated at the excitation amplitudes of 10 V and 160 V are given with respect to the excitation frequency in Figures 3.10 (e)-(h). The resonance strips corresponding to the second and third nFRFs can be identified as the ranges of excitation amplitude and frequency for which the non-linear dynamic behavior is observed. In fact, the contribution of the harmonic response components to the total dynamic response is higher within the ranges including the corresponding resonance strips.

First three resonance strips corresponding to the presented nFRFs are marked as A, B and C in Figures 3.10 (a)-(c) as well as the corresponding peaks in Figures 3.10 (e)-(g). Examining the excitation frequencies at which the first three resonances occur for each nFRF, following observation can be made: If a resonance peak corresponding to the fundamental nFRF occur at around the excitation frequency of ω_{ex} , the corresponding resonance peaks for the n^{th} nFRFs are seen at around the excitation frequency of ω_{ex}/n . For instance, for an excitation amplitude of 160 V the resonant peak A occurs around 13.3 kHz,

6.9 kHz and 4.8 kHz for the fundamental, second and third harmonic response components, respectively. The contribution of higher harmonic response components are higher within the ranges of excitation frequency and amplitude including the corresponding resonant peaks. Accordingly, accurate representation of the dynamic response within the excitation frequency ranges that are below resonance for the fundamental response component requires inclusion of the higher harmonic response components due to the aforementioned behavior of resonant frequencies.

At low excitation amplitudes, the amplitude ratios of nhFRFs are higher as compared to that at higher excitation amplitudes, as illustrated in Figs. 3.10 (d) and (h). This may be explained by considering the fact that the measurement noise that contributes to the non-harmonic component has a constant amplitude throughout the excitation amplitude range. Accordingly the amplitude ratio is higher when this constant amplitude is divided by a lower excitation amplitude. At higher excitation amplitudes, the excitation frequency ranges within which the amplitude ratio of nhFRFs are high such as the region D in Fig.3.10 (d), are the ranges within which specific non-harmonic response components are prominent. In fact, within these ranges, the spectral flatness of the non-harmonic power spectral density is determined to be as low as -100 dB, whereas more than -10 dB spectral flatness is observed in the ranges where the specific non-harmonic components are not observed.

The first three nFRFs along with the nhFRF for the excitation of the y stack of Actuator 2 and the measured responses along the y_m axis is given in Fig. 3.11. It can be observed that for this actuator the first resonant peaks occur at higher frequencies compared to Actuator 1 for each harmonic response component.

3.5 Analysis of Measurement Errors

The fidelity of the characterization and representation methods presented in this work depends critically upon the accuracy of the measurement approach. In particular, there are three possible error sources that could affect the measurements: (1) Electrical noise and errors of the LDV controller/decoder and of the data acquisition system; (2) optical reflection, focusing and mutually-orthogonal alignment of the LDVs, and (3) motions of the measurement frame as a response to piezo-stack excitations and external noise. Among these, the measurement-frame vibrations are the largest contributor to the measurement errors. Although a formal uncertainty quantification of the characterization technique including an analysis of contribution from each of those sources is beyond the scope of this work, an experimental analysis of cumulative measurement errors from all of the afore-

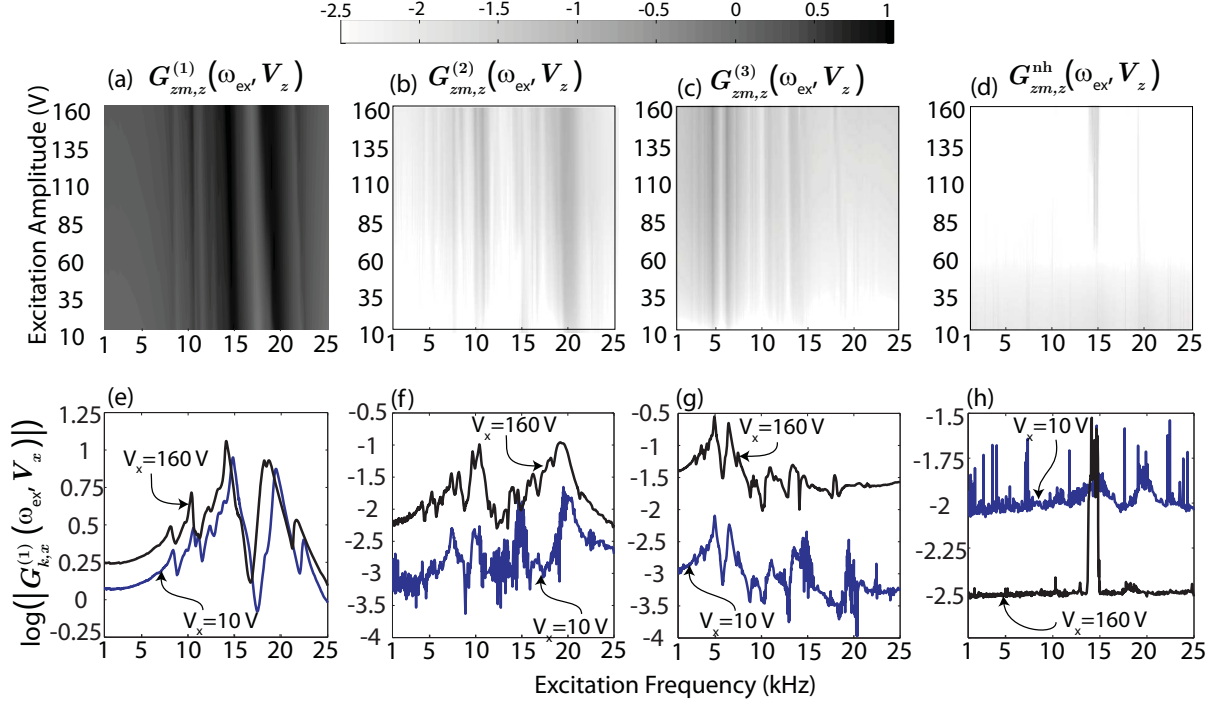


Figure 3.11: Amplitude ratios of to the first three nFRFs and nhFRF (in log scale) corresponding to the excitation of z stack and response along the z_m axis for Actuator 2: (a)-(d) As a function of the excitation frequency and amplitude. (e)-(h) as a function of the excitation frequency for the excitation amplitudes of 10 V and 160 V.

mentioned sources considering the worst-case scenarios is conducted to enable assessing the measurement technique. It is noted here that this analysis covers 1 kHz to 25 kHz range, which is the frequency range of interest in this work. Since the characterization method is based on frequency-domain representation, the errors are considered separately for the harmonic (including the fundamental) and non-harmonic response components.

A set of stepped-sine tests were conducted to identify the compounded measurement error considering the worst-case scenario. For this purpose, each of the three piezo-stacks (x , y and z) of Actuator 1 are excited separately with the largest excitation voltage considered in this work (160 V). A large steel mass (100 mm x 130 mm x 300 mm) is bolted down on the optical table. Each of the three lasers is shined onto the large mass. Since the relative vibrations between the large mass and the optical table can be assumed to be negligible in this configuration, any non-zero displacement measurement may be considered as the cumulative measurement error.

To determine the measurement errors corresponding to harmonic and non-harmonic response components, the PSD of the measured displacements (errors) are first calculated using Eq. (3.1). Using the PSD, the power corresponding to the n^{th} harmonic component of

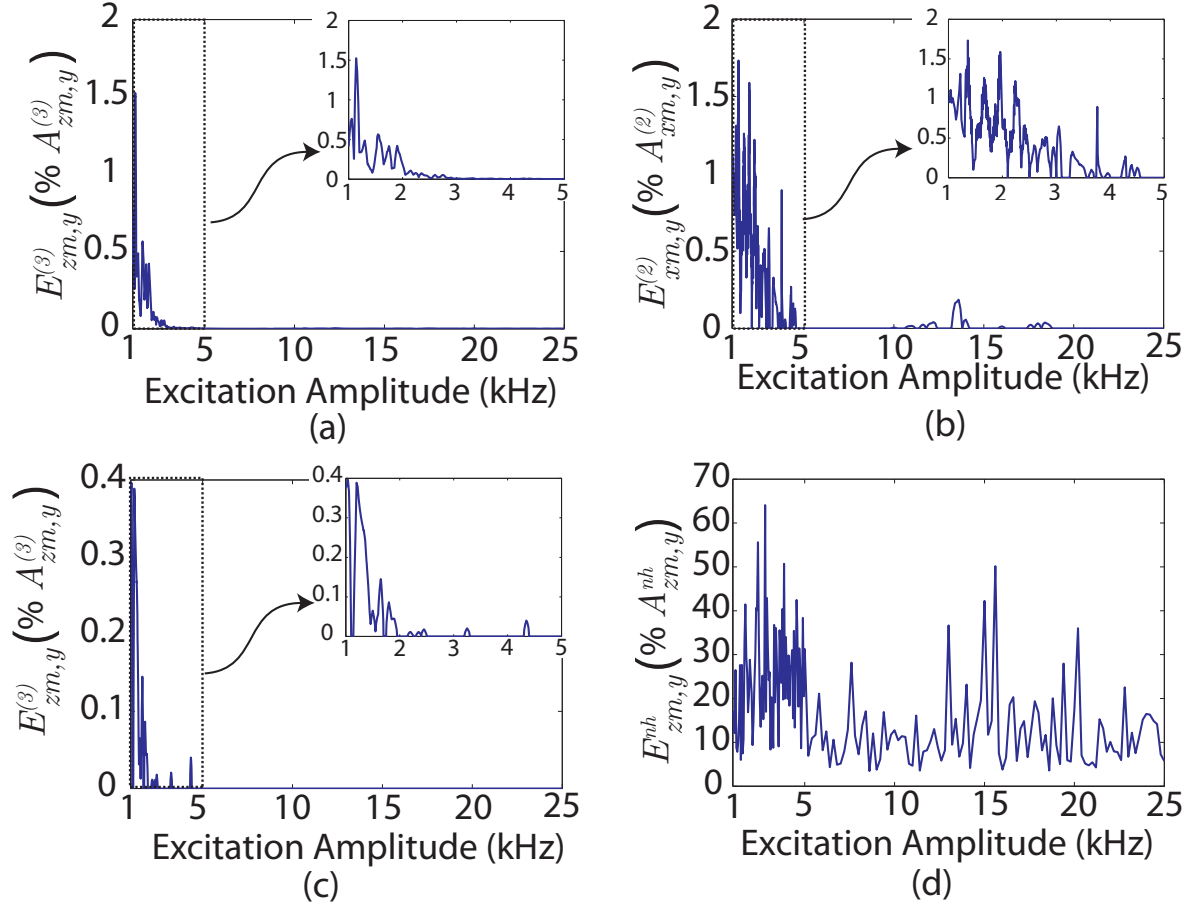


Figure 3.12: Percent harmonic and non-harmonic error amplitudes as functions of the excitation frequency (a)-(c) Percent amplitude errors for the first three harmonic error components (d) Percent amplitude errors for the non-harmonic error components

the error motions is then calculated using Eq. (3.2) within the frequency band $n\omega_{ex} \pm 3\Delta\omega$. Similarly, the power corresponding to the non-harmonic components of the error motions is calculated using Eq. (3.3). Next, the amplitudes of the harmonic ($E_{ki}^{(n)}(\omega_{ex}, 160V)$) and non-harmonic ($E_{ki}^{nh}(\omega_{ex}, 160V)$) components of the error motions are calculated by taking the square root of the corresponding powers. Considering the worst-case scenario, the actual amplitude of the harmonic and non-harmonic response components are expected to lie within the ranges $A_{ki}^{(n)}(\omega_{ex}, V_i) \pm E_{ki}^{(n)}(\omega_{ex}, 160V)$ and $A_{ki}^{nh}(\omega_{ex}, V_i) \pm E_{ki}^{nh}(\omega_{ex}, 160V)$, respectively.

To determine the amount of error on the amplitude of harmonic components, the ratio (percent) of the calculated error amplitudes to the response (from the piezo-stack measurements) amplitudes are calculated for each of the first five harmonics. This calculation is performed at each excitation frequency while exciting each of the three piezo-stacks and

Table 3.3: Largest error amplitudes and ratios for the first five harmonic and non-harmonic response components.

	$\max(E_{kx}^{(n)})$		$\max(E_{ky}^{(n)})$		$\max(E_{kz}^{(n)})$	
n	nm	% $A_{ki}^{(n)}$	nm	% $A_{ki}^{(n)}$	nm	% $A_{ki}^{(n)}$
1	0.0833	0.88	0.1489	1.59	0.5824	0.21
2	0.0038	1.47	0.011	1.47	0.0089	2.62
3	0.01	11.41	0.0032	0.4	0.0032	0.36
4	0.0032	13.27	0.0032	5.12	0.0032	5
5	0.002	1.06	0.0032	1.2	0.003	0.65
	$\max(E_{kx}^{nh})$		$\max(E_{ky}^{nh})$		$\max(E_{kz}^{nh})$	
	nm	% A_{ki}^{nh}	nm	% A_{ki}^{nh}	nm	% A_{ki}^{nh}
	0.3308	52.30	0.8398	64.07	0.3816	57.37

measuring from each measurement axis. Figure 3.12(a)-3.12(c) provide the error ratios for the first three harmonics for the excitation of the y stack and the measurement axes along which the largest error amplitudes are observed for each case. For the first five harmonic components, the largest error amplitudes and ratios are given in Table 3.3.

It is seen that, for the excitation of a particular stack, the measurement axis along which the maximum error occurs varies for different harmonics. Furthermore, the largest error ratios (percentages) are observed within 1 kHz to 2 kHz range, which is the range that includes several resonant frequencies of the measurement frame (as identified separately through modal tests on the frame). This observation highlights the large contribution of frame vibrations to the measurement error. The maximum percent error for the fundamental frequency is below 1.59%. For the higher harmonic components, although the percent errors of up to 13.27% are observed, they correspond to the cases where the absolute error is less than 0.01 nm.

Similarly, amplitude ratio of the non-harmonic error components to the non-harmonic response components are calculated at each excitation frequency. Figure 3.12(d) gives the percent non-harmonic error for the case that yields the largest non-harmonic error ratio (excitation of y stack and measurement along the z_m axis). The absolute and percent non-harmonic errors amplitudes are also given in Table 3.3. The amplitude of the non-harmonic error components can reach up to 64.07% of the non-harmonic response amplitudes: this may be interpreted as the measurement error being the major contributor to the measured non-harmonic response (thus, the actual non-harmonic motions of the piezo-stack actuators are significantly lower than they were measured). In contrast to those large errors for its broadband portion, the percent non-harmonic amplitude error corresponding to *specific* (single-frequency) non-harmonic response components are comparable to those observed for

the harmonic components. For instance, a specific non-harmonic response observed at 13.4 kHz has a non-harmonic amplitude error of 0.36%.

3.6 Summary and Conclusions

This chapter has presented a method for characterization and representation of piezo-stack actuator dynamics. This LDV-based method captures the nonlinear multi-dimensional dynamic behavior of piezo-stack actuators, including three-dimensional, multi-frequency, and amplitude-dependent response characteristics. The method involves the use of a metrology system for accurate measurement of motions, a stepped-sine modal testing technique, and a representation of the dynamic behavior through a newly developed extended-FRF approach. To determine the contribution of different frequency components in the response, and thus, to enable obtaining simplified dynamic representations, a power-based analysis has also been outlined. The application of the presented method is demonstrated by characterizing two different three-axis piezo-stack actuators.

Following conclusions are drawn from this work:

- Piezo-stack actuators do not possess stationary physical motion axes: The response is three-dimensional, and its direction for a given excitation varies mainly with the excitation frequency and secondarily with the excitation amplitude. This is an important departure from the conventional quasi-static behavior of piezoelectric actuators. Therefore, obtaining specific high-accuracy motions from piezo-stack actuators necessitates three-dimensional characterization of their dynamic behavior within a broad range of frequencies and excitation amplitudes. The presented method successfully addresses this need.
- The dynamic response of piezo-stack actuators involves relatively strong components at the harmonics of the excitation frequency, and a broad-band response at non-harmonics frequencies. This behavior, and the amplitude-dependent nonlinearities, can be effectively captured through the presented LDV-based 3D characterization technique.
- Contribution of different response (frequency) components can be analyzed through the presented power-based approach. This analysis enables identifying dominant response components, and thus, representing the dynamic behavior in a simplified fashion.

- The proposed extended-FRF technique successfully represents the 3D non-linear dynamics of piezo-stack actuators within a simplified framework. This representation can be used to facilitate obtaining accurate motions from piezo-stack actuators within a broad range of frequencies and amplitudes.
- The measurement errors associated with the presented technique are characterized. The maximum error for the amplitude at the fundamental frequency is less than 1.5% of the response amplitude. Although higher error percentages are observed for higher harmonics, their corresponding response amplitude is in the pico-meter range. It is also concluded that the measurement noise and error accounts for a major portion of the measurements of (the broadband portion of) the non-harmonic response.

Chapter 4

A Method for Open-loop Control of Dynamic Motions of Piezo-stack Actuators

The work presented in Chapter 3 yielded a mathematical representation of the non-linear dynamic response of the piezo-stack actuators. In this chapter, an open-loop control method based on this representation is devised to generate desired single-frequency motions. The technical contribution of the work presented in this chapter is the capability to generate accurate nanotool rotations.

4.1 Introduction

Piezoelectric actuators are essential tools in nanotechnology and precision engineering due to their capability of generating nano-scale motions with sub-nanometer resolution. This capability has been applied in a wide variety of applications including scanning-probe microscopy [8], nano-fabrication [61] and nano-manipulation [78]. To obtain larger motion amplitudes, piezoelectric actuators are commonly implemented in a *stack* configuration, where multiple layers of piezo-electric material are connected in series [79]. Multi-dimensional motions can be obtained by combining piezo-stack actuators in a multi-axis configuration.

The implementation of piezo-stack actuators to obtain accurate motions is challenged by a number of factors. Firstly, motions of piezo-stack actuators have a three-dimensional nature, especially during dynamic operation [80] due to their complex deformation modes that strongly depend upon their mechanical assembly and boundary conditions. Secondly,

the piezo-stack actuators exhibit non-linear response behavior that is usually expressed in the form of hysteresis and creep. In dynamic operation, the response of the piezo-stack actuators to sinusoidal excitations includes components at not only the intended excitation frequency, but also its harmonics [70]. Furthermore, the frequency response characteristics of piezo-stack actuators strongly depend upon the excitation amplitudes [68]. Therefore, to obtain accurate three-dimensional motions at high frequencies, the nonlinear nature of dynamic motions of piezo-stack actuators should be well-understood and controlled through methods that comprehensively address the aforementioned complexities.

Several open-loop and closed-loop control strategies have been proposed to specifically address the hysteresis and creep behavior of piezoelectric actuators [80]. Open-loop methods aim to linearize the actuator behavior by compensating for the hysteresis. To implement the open-loop control methods, the hysteretic behavior of the actuators are modeled various approaches, including Prandtl-Ishlinski [81,82], Bouc-Wen [83], and Preisach [65] methods. Constitutive-memory based methods, such as in [84], are also used. Inverse of the determined hysteresis model is implemented as the open-loop controller. Iterative methods for compensation of hysteresis are also demonstrated in the literature [85]. Feedback control of piezoelectric actuator motions is also demonstrated using non-linear control methods such as sliding-mode control [63,78] and robust control methods such as H_∞ control [86]. It has been shown that the feedback-only motion control is typically efficient at low frequency operation, providing successful compensation of the creep behavior [79]. Improved performance of closed-loop methods at high frequencies is achieved through the implementation of the inverse hysteresis models as feedforward controllers [79,87,88]. The need for external sensors for position feedback can be eliminated by indirectly measuring the motions through the charge induced by the actuator [89,90].

Although satisfactory control performance have been obtained in a wide-frequency range using closed-loop methods, their implementation for miniature actuators is limited due to the need for bulky and expensive sensors and complex circuitry for position feedback [82]. On the other hand, the open-loop methods presented in the literature describe both the amplitude and frequency based non-linear dynamic characteristics of piezo-stack actuators through time-domain hysteresis models with high complexity; resulting models are commonly subject to errors from variety of sources [80]. To date, frequency domain characterization, and the associated open-loop compensation, of the nonlinear dynamics of the piezo-stack actuators have not been addressed. Most importantly, there is a strong need for better understanding of three-dimensional motion behavior and multi-axis, MIMO control models for piezo-stack actuators [80].

In this paper, we present a frequency domain method for open-loop control of three-dimensional dynamic motions of piezo-stack actuators. The nonlinear dynamic behavior of the piezo-stack actuator is described through an LDV-based dynamic characterization method [91] explained in the previous chapter. That work yielded a new frequency-domain description of non-linear response behavior, referred to here as the *harmonic frequency response function* (hFRF) approach. The hFRF approach describes the three-dimensional dynamic behavior using components at the excitation frequency and its harmonics (due to non-linearity). Based on the hFRF approach, the open-loop control method presented here aims to generate arbitrary single-frequency motions in three-dimensions. For this purpose, each axis of the piezo-stack actuator is supplied with *both* (1) an excitation component at the motion frequency to generate the desired motion, *and* (2) compensatory excitation components at the harmonics of the motion frequency to compensate for the (undesired) harmonic response components. The excitation components are determined by using the hFRF-based response representations. To compensate for higher-order harmonic response, an additional iterative procedure is described. The performance of the method is evaluated through experimentation using two different three-axis piezo-stack actuators. A set of motion metrics is defined to quantify the accuracy of the presented technique in creating single-frequency motions.

4.1.1 Calculation of response to arbitrary excitations

As noted in Chapter 3, the first few harmonic response components constitutes to more than 99% of the overall response. Accordingly, throughout the development of the control method, the response representation including only a limited number of harmonic response components will be considered.

Using the hFRFs, the harmonic components of the response to arbitrary sinusoidal excitations can be determined. Frequency domain representation of an arbitrary sinusoidal excitation provided to the stack i of the piezo-stack actuator is given by $E_i(\omega) = V_i \delta(\omega - \omega_{ex})$, where $V_i = |V_i| e^{j\angle V_i}$ is the complex amplitude of the excitation and δ is the dirac delta function. The complex amplitude of the n^{th} harmonic component of the response to this excitation can be represented by a 3×1 vector $\mathbf{R}^{(n)} = \{R_k^{(n)}\}$, where $R_k^{(n)}$ is the complex amplitude of the response component along the measurement frame axis k :

$$R_k^{(n)} = G_{ki}^{(n)} \Big|_{\omega_{ex}, |V_i|} S_i^{(n)} V_i, \quad (4.1)$$

where $S_i^{(n)} = e^{j(n-1)\angle V_i}$ is the n^{th} harmonic phase shift operator that is needed to obtain the correct phase shift at the n^{th} harmonic response component due to the phase shift of the excitation.

For a three-axis piezo-stack actuator, the excitation is represented in vector form as $\mathbf{E}(\omega) = \mathbf{V}\delta(\omega - \omega_{ex})$, where $\mathbf{V} = \{V_i\}$ is a 3×1 complex excitation amplitude vector, elements of which are the excitations supplied to individual stacks ($i = x, y, z$). The n^{th} harmonic component of the response to this excitation is given by

$$\mathbf{R}^{(n)} = \mathbf{G}^{(n)} \Big|_{\omega_{ex}, |\mathbf{V}|} \mathbf{S}^{(n)} \mathbf{V}, \quad (4.2)$$

where $\mathbf{G}^{(n)}(\omega_{ex}, |\mathbf{V}|) = [G_{ki}^{(n)}(\omega_{ex}, |V_i|)]$ is the 3×3 hFRF matrix and $\mathbf{S}^{(n)} = \text{diag}\{S_i^{(n)}\}$ is the 3×3 n^{th} harmonic phase shift operator.

Following the simplified response representation and using Eq. (4.2), the total response of the actuator is given in the frequency domain as

$$\mathbf{R}(\omega) = \mathbf{R}^{(1)}\delta(\omega - \omega_{ex}) + \sum_{n=2}^{n_{max}} \mathbf{R}^{(n)}\delta(\omega - n\omega_{ex}), \quad (4.3)$$

where n_{max} is the highest harmonic number included in the simplified response representation. The first term in Eq.(4.3) represents the fundamental response component, whereas the second term represents the higher harmonic response components.

4.2 Definition of the control problem

The goal of the open-loop control method is to determine the excitation signals to the individual stacks of the piezo-stack actuators that will produce the desired three-dimensional motions. In this study, the discussion is limited to single frequency motions, which can be described geometrically by a family of Lissajous curves in an arbitrary plane within the measurement reference frame, as illustrated in Figure 4.1. A *nominal motion frame of reference* $[\gamma, \eta, \zeta]$ is defined by assigning the ζ axis to be normal to the motion plane. A parametric representation of such motions within the nominal motion frame can be given as

$$d_\eta(t) = |D_\eta| \sin(\omega_f t + \angle D_\eta) \quad d_\gamma(t) = |D_\gamma| \sin(\omega_f t + \angle D_\gamma), \text{ and } d_\zeta(t) = 0, \quad (4.4)$$

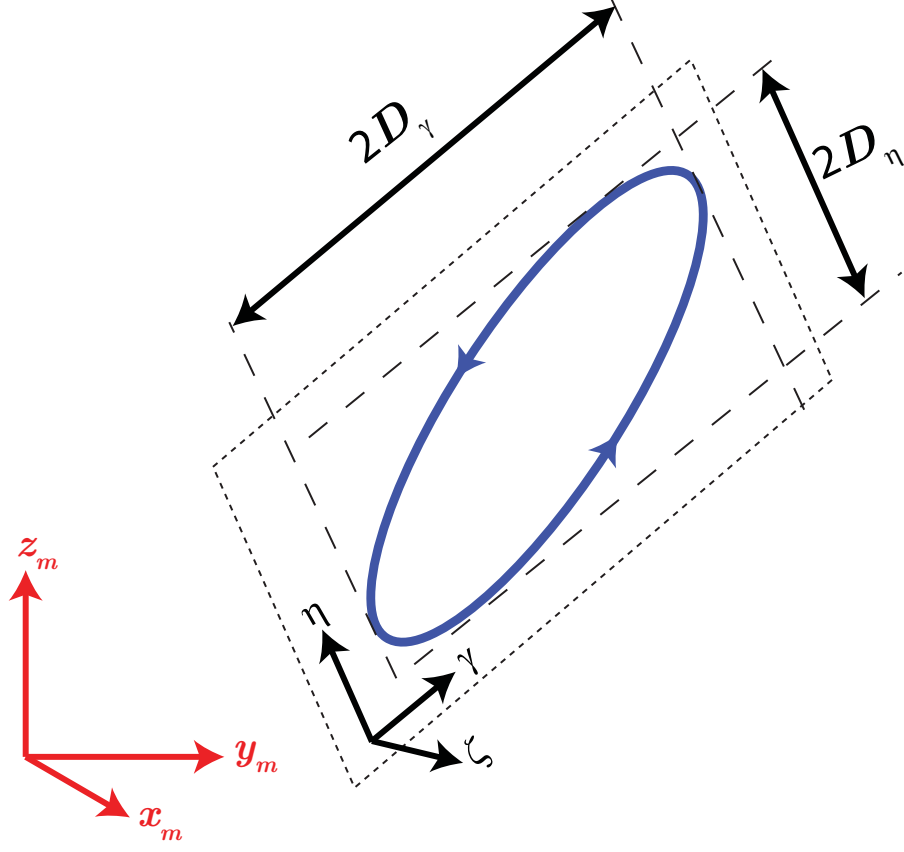


Figure 4.1: Geometric description of three-dimensional single frequency motions

where ω_f is the fundamental motion frequency, and D_η and D_γ are the complex amplitudes of the motion along the η and γ directions, respectively. It should be noted that the motion follows an elliptical path if $\angle D_\eta = \angle D_\gamma + \pi/2$. If additionally, $|D_\eta| = |D_\gamma|$, the motion follows a circular path. When $\angle D_\eta = \angle D_\gamma$, the motion is along a line segment.

As given in Eq. (4.3), if the actuator is excited at the fundamental motion frequency with a single frequency excitation, the response will include components not only at the fundamental frequency but also at its harmonics. Thus, in the proposed method, to generate a given single-frequency motion, the piezo-stack actuator is excited at both the fundamental motion frequency and its harmonics. The purpose of the excitation at the harmonics is to compensate for the unwanted higher harmonic components. The frequency domain representation of this excitation is given by

$$\mathbf{V}(\omega) = \mathbf{V}^{(1)}\delta(\omega - \omega_f) + \sum_{n=2}^{n_{max}} \mathbf{V}^{(n)}\delta(\omega - n\omega_f), \quad (4.5)$$

where $\mathbf{V}^{(1)} = \{V_i^{(1)}\}$ is the complex amplitude of the *fundamental excitation component* at

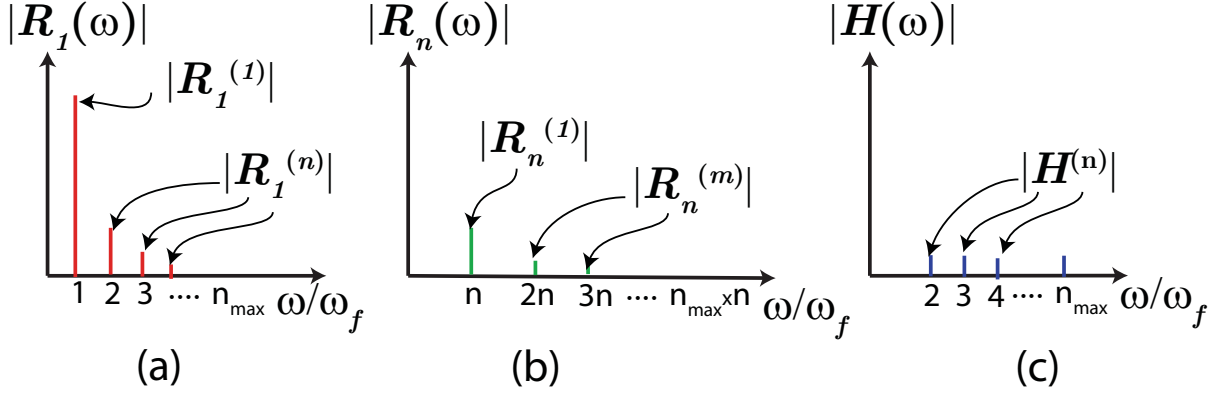


Figure 4.2: Frequency domain representations of the response terms (a) $\mathbf{R}_1(\omega)$ (b) $\mathbf{R}_n(\omega)$ and (c) $\mathbf{H}(\omega)$

the fundamental motion frequency. The fundamental excitation component is selected such that the response at the fundamental frequency is equal to the desired motion. Excitation components that are supplied at the harmonics are referred to as the *compensatory excitation components*, the complex amplitude of which are given by $\mathbf{V}^{(n)} = \{V_i^{(n)}\}$ for $n = 2 \dots n_{max}$.

Considering the non-linear behavior, the response of the piezo-stack actuator to the multi-harmonic excitation is given by summation of three response terms in the frequency domain as

$$\mathbf{R}(\omega) = \mathbf{R}_1(\omega) + \sum_{n=2}^{n_{max}} \mathbf{R}_n(\omega) + \mathbf{H}(\omega), \quad (4.6)$$

where $\mathbf{R}_1(\omega)$ and $\mathbf{R}_n(\omega)$ are the individual responses to the fundamental and the n^{th} harmonic compensatory excitation component, respectively. The term $\mathbf{H}(\omega)$ is the higher-order (non-linear) response terms that arise due to simultaneous the excitation of the (non-linear) actuator by the fundamental and compensatory excitation components. From Eq. (4.3), the response term $\mathbf{R}_1(\omega)$ can be calculated as

$$\mathbf{R}_1(\omega) = \mathbf{R}_1^{(1)} \delta(\omega - \omega_f) + \sum_{n=2}^{n_{max}} \mathbf{R}_1^{(n)} \delta(\omega - n\omega_f), \quad (4.7)$$

where from Eq. (4.2), $\mathbf{R}_1^{(n)} = \mathbf{G}^{(n)}(\omega_f, |\mathbf{V}^{(1)}|) \mathbf{S}^{(n)} \mathbf{V}^{(1)}$. The amplitudes of the individual components of term $\mathbf{R}_1(\omega)$ is schematically represented in Fig. 4.2(a), where the frequency axis is normalized with respect to the fundamental frequency.

The response to the n^{th} harmonic compensatory excitation component $\mathbf{R}_n(\omega)$ can also

be calculated through Eq. (4.3) as

$$\mathbf{R}_n(\omega) = \mathbf{R}_n^{(1)}\delta(\omega - n\omega_f) + \sum_{m=2}^{n_{max}} \mathbf{R}_n^{(m)}\delta(\omega - nm\omega_f), \quad (4.8)$$

where $\mathbf{R}_n^{(m)} = \mathbf{G}^{(m)}(n\omega_f, |\mathbf{V}^{(n)}|)\mathbf{S}^{(m)}\mathbf{V}^{(n)}$. Similarly, the amplitudes of the individual components of the term $\mathbf{R}_n(\omega)$ is schematically represented in Fig. 4.2(b). The component $\mathbf{R}_n^{(1)}$ is used to compensate for harmonic distortions due to fundamental excitation ($\mathbf{R}_1^{(n)}$) at frequency $n\omega_f$. The components $\mathbf{R}_n^{(m)}$ for $m = 2 \dots n_{max}$ occur at the higher harmonics of the n^{th} harmonic frequency (namely at frequencies $nm\omega_f$) due to non-linearity.

Referring to the actuator characteristics presented in [91], the cumulative power contribution of the higher harmonic components of the response to the fundamental excitation (i.e, the second term in Eq. (4.7)) is approximately an order of magnitude smaller than that of the fundamental response component ($\mathbf{R}_1^{(1)}$). Therefore, the amplitude of the compensatory excitation components will be considerably smaller than that of the fundamental excitation component. The contribution of higher harmonic components was also seen to further decrease at lower excitation amplitudes. Accordingly, the response at the harmonics of the harmonics (i.e., $nm\omega_f$) is expected to be very small, and will thus be neglected in this work. With this assumption, Eq. (4.8) is reduced to $\mathbf{R}_n(\omega) = \mathbf{R}_n^{(1)}\delta(\omega - n\omega_f)$.

The response of the actuator with the non-linear dynamic behavior to the simultaneous excitation at multiple frequencies will deviate from the superposition of the individual responses to the excitations at each frequency. This deviation is captured by the higher-order response ($\mathbf{H}(\omega)$) throughout the entire frequency range. The individual responses to fundamental and compensatory excitation components ($\mathbf{R}_1(\omega)$ and $\mathbf{R}_n(\omega)$) simultaneously contribute to the total response only at the frequencies $n\omega_f$ for $n = 2 \dots n_{max}$. Thus, in this work, the higher-order response is assumed to be negligible in the rest of the frequency range as shown in Fig. 4.2(c). Therefore,

$$\mathbf{H}(\omega) = \sum_{n=2}^{n_{max}} \mathbf{H}^{(n)}\delta(\omega - n\omega_f). \quad (4.9)$$

Considering the aforementioned simplifications, the expression for the total response can

be given in terms of the components at the fundamental frequency and its harmonics as

$$\mathbf{R}(\omega) = \mathbf{R}_1^{(1)}\delta(\omega - \omega_f) + \sum_{n=2}^{n_{max}} \mathbf{\Gamma}^{(n)}\delta(\omega - n\omega_f), \quad (4.10)$$

where

$$\mathbf{\Gamma}^{(n)} = \mathbf{R}_1^{(n)} + \mathbf{R}_n^{(1)} + \mathbf{H}^{(n)}. \quad (4.11)$$

are the complex amplitude vectors for the higher harmonic response components.

4.3 Determination of the excitations to generate arbitrary single-frequency motions

The goal of the proposed open-loop control method can now be restated as the determination of the fundamental and compensatory excitation components such that the fundamental response component is equal to the desired motion and the higher harmonic response components are reduced to sufficiently low levels. Fundamental and compensatory excitation components are separately determined using the fundamental and harmonic FRFs.

4.3.1 Determination of the fundamental excitation component

The frequency domain representation of the desired response is given by $\mathbf{D}\delta(\omega - \omega_f)$ where $\mathbf{D} = \{|D_k|e^{j\angle D_k}\}$ is the complex amplitude vector corresponding to the desired response at the fundamental motion frequency. The vector \mathbf{D} is defined in the measurement frame and may be obtained from Eq. (4.4) through a coordinate transformation.

The fundamental response component depends only on the fundamental excitation component. Accordingly, by setting the complex amplitude of the fundamental response component equal to the complex amplitude of the desired response (\mathbf{D}), the fundamental excitation can be determined as

$$\mathbf{V}^{(1)} = \left[\mathbf{G}^{(1)} \Big|_{\omega_f, |\mathbf{V}^{(1)}|} \right]^{-1} \mathbf{D}. \quad (4.12)$$

Since, due to non-linear behavior, $\mathbf{G}^{(1)}$ matrix is a function of the excitation amplitude $|\mathbf{V}^{(1)}|$, Eq. (4.12) is an implicit equation and should be solved iteratively. For the iterative solution, the identity matrix is used as an initial estimate for the $\mathbf{G}^{(1)}$ matrix is approx-

imated to be an identity matrix, yielding the initial approximation for the fundamental excitation component $\mathbf{V}^{(1)} = \mathbf{D}$. The corresponding $\mathbf{G}^{(1)}$ matrix (amplitude ratio and relative phase) are then calculated using the fundamental FRFs obtained from the characterization tests. Since the fundamental FRFs are available at only distinct excitation frequencies and amplitudes, spline interpolation is used to determine $\mathbf{G}^{(1)}$ for a given $|\mathbf{V}^{(1)}|$ and ω_f . Next, Eq. (4.12) is solved and the next iteration of $\mathbf{V}^{(1)}$ is calculated. An error vector is also calculated as the difference between the guessed and calculated $\mathbf{V}^{(1)}$ vectors. At every iteration step, the $\mathbf{V}^{(1)}$ vector calculated at the previous step is used as the next guess to calculate the $\mathbf{G}^{(1)}$ matrix. The above procedure is repeated until the amplitude of each element of the error vector reduces to less than 0.1% of the corresponding element of the $\mathbf{V}^{(1)}$ vector determined as a result of the last iteration.

4.3.2 Determination of the compensatory excitation components

As shown in Eq. (4.11), the compensatory excitation components ($\mathbf{V}^{(n)}$) should be selected such that the compensating response component $\mathbf{R}_n^{(1)}$ cancels out the harmonic components of the response to the fundamental excitation ($\mathbf{R}_1^{(n)}$) and the higher-order response terms ($\mathbf{H}^{(n)}$). The component $\mathbf{R}_1^{(n)}$ can be calculated through the determined fundamental excitation component and the hFRFs. However, the higher-order terms cannot be predicted; therefore, a direct analytical solution (similar to Eq. (4.12)) cannot be obtained for the compensatory excitation components that will simultaneously compensate for $\mathbf{R}_1^{(n)}$ and $\mathbf{H}^{(n)}$. In this chapter, an alternative harmonic compensation scheme is adopted, where the *first-order harmonic compensation* is used to compensate for only the component $\mathbf{R}_1^{(n)}$. Higher-orders of harmonic compensation are determined through an iterative experimental method. Increasing orders of harmonic compensation successively reduce the effect of the higher-order response terms.

The first-order compensatory excitation component $\mathbf{V}_1^{(n)}$ can be analytically calculated by solving $\mathbf{R}_1^{(n)} + \mathbf{R}_n^{(1)} = 0$ as

$$\mathbf{V}_1^{(n)} = -\left[\mathbf{G}^{(1)}\Big|_{n\omega_f, |\mathbf{V}_1^{(n)}|}\right]^{-1} \mathbf{G}^{(n)}\Big|_{\omega_f, |\mathbf{V}^{(1)}|} \mathbf{S}^{(n)} \mathbf{V}^{(1)}. \quad (4.13)$$

According to Eq. (4.11), when the actuator is excited with the fundamental and the first-order compensatory excitation components, the residual harmonic response component will be equal to the higher-order terms only ($\mathbf{\Gamma}^{(n)} = \mathbf{H}^{(n)}$). Therefore, an analysis of the residual harmonic response will enable identifying the need for additional compensation to reduce the effect of the higher-order terms. Harmonic response power may be used for such an

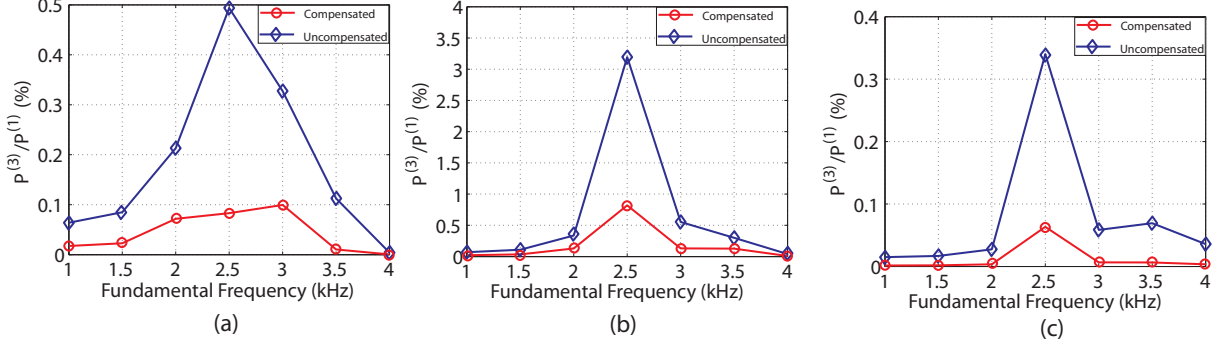


Figure 4.3: The reduction of third harmonic power through first level harmonic compensation for the cases where the fundamental excitation of 160 V amplitude is supplied to the (a) x -stack (b) y -stack and (c) z -stack of the actuator.

analysis. The harmonic response power is defined as:

$$P^{(n)} = \sum_{k=x_m, y_m, z_m} |\Gamma_k^{(n)}|^2, \quad (4.14)$$

where $\Gamma_k^{(n)}$ is the complex amplitude of the n^{th} harmonic component of the response measured along the measurement frame axis k .

Figure 4.3 shows the third harmonic response power, as a percentage of the response power of the fundamental component ($P^{(3)}/P^{(1)}$), both before and after the first-order harmonic compensation for three representative cases. It should be noted that without any compensatory excitation, the harmonic response will be equal to the components in response to the fundamental excitation only ($\Gamma^{(n)} = \mathbf{R}_1^{(n)}$). Each plot included in this figure corresponds to a case where the fundamental excitation with an amplitude of 160 V and a range of frequencies between 1 kHz to 4 kHz is supplied only to one axis of a three-axis piezo-stack actuator (e.g. $\mathbf{V}^{(1)} = [160 \ 0 \ 0]V$ in Fig. 4.3(a)). The first-order compensatory excitation components calculated through Eq. (4.13) are supplied to all three axis for each case. As seen in these examples, for most of the tested fundamental frequencies, the first-order harmonic compensation is able to compensate for at least 80% of the harmonic response power, reducing the power of the third harmonic response component down to less than 0.1% of that of the fundamental component. In such a case, the first-order compensation of the harmonic components can be considered as sufficient. However, there are other cases, (e.g., around 2.5 kHz, where the fundamental excitation is provided to the y stack of the actuator), where the response power of the higher-order terms is as high as 1% of the harmonic response power of the fundamental component. Obtaining accurate motions in such cases necessitates higher-orders of harmonic compensation.

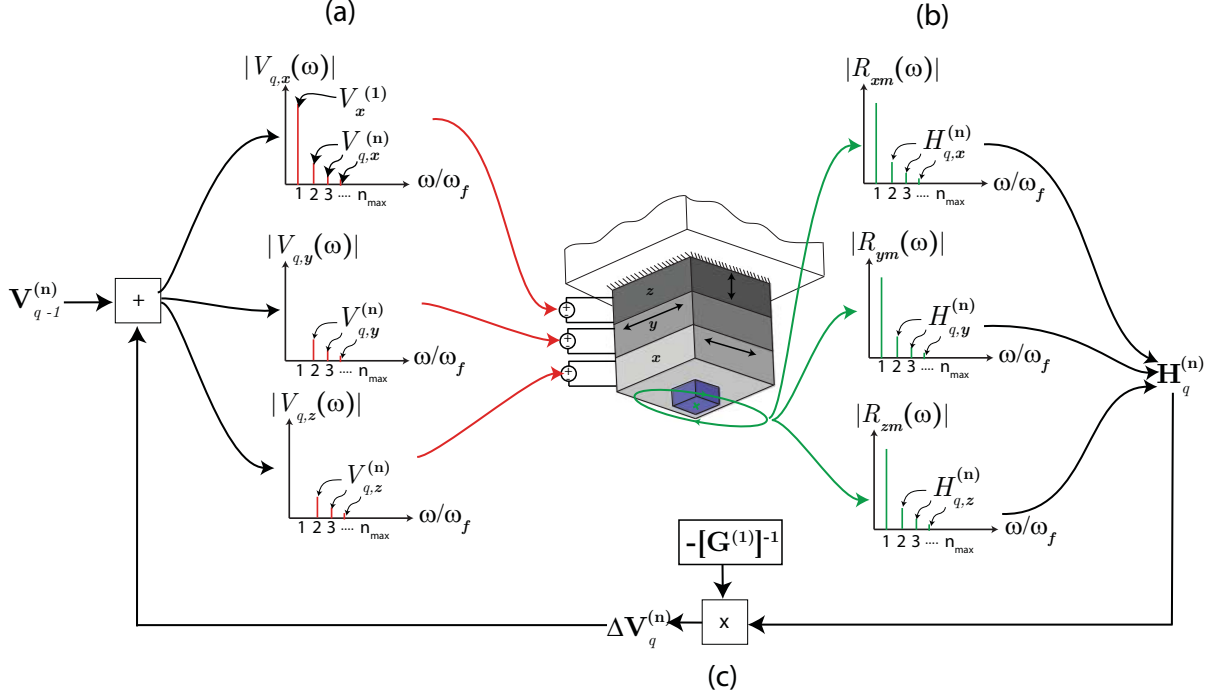


Figure 4.4: Description of the multi-level stepped-sine testing procedure. The fundamental excitation is supplied to x stack as an example.

To determine the higher-order compensatory excitation components, an iterative experimental procedure is adopted. The higher-order compensatory excitation components are empirically correlated to the fundamental excitation as

$$\mathbf{V}_q^{(n)} = \mathbf{C}_q^{(n)} \Big|_{\omega_f, |\mathbf{V}^{(1)}|} \mathbf{S}^{(n)} \mathbf{V}^{(1)}, \quad (4.15)$$

where $\mathbf{C}_q^{(n)}$ is the q^{th} order 3×3 compensation matrix. The compensation matrices can be decomposed into three column vectors as $\mathbf{C}_q^{(n)} = [\lambda_{q,x}^{(n)} : \lambda_{q,y}^{(n)} : \lambda_{q,z}^{(n)}]$, where $\lambda_{q,i}^{(n)}(\omega_f, |\mathbf{V}_i^{(1)}|)$ are the q^{th} order *compensation vectors* corresponding to the stack i . The compensation vectors correlate the fundamental excitation supplied to a particular stack to the corresponding compensatory excitation and are separately determined through an experimental procedure.

To determine the higher order compensation vectors for various fundamental frequencies and excitation amplitudes, a stepped-sine testing method is used (see Fig. 4.4) where a fundamental excitation with no added phase ($\phi_i = 0$) is supplied to only one stack of the

piezo-stack actuator. In such a case, Eq. (4.15) reduces to

$$\mathbf{V}_q^{(n)} = \lambda_{q,i}^{(n)} \Big|_{\omega_f, |V_i^{(1)}|} |V_i^{(1)}|, \quad (4.16)$$

where i corresponds to the stack to which the fundamental excitation is supplied. During the stepped-sine testing, the fundamental frequency (ω_f) is varied incrementally at each excitation step within the predetermined range, while keeping the fundamental excitation amplitude constant. To determine the compensation vector with the order $q + 1$, at each excitation step in addition to the fundamental excitation, the q^{th} order compensatory excitations are provided to *all three stacks* at frequencies $n\omega_f$ where $n = 2 \dots n_{max}$ (Fig. 4.4(a)). To determine the 2^{nd} -order compensation vectors, analytically determined first-order compensatory excitations ($\mathbf{V}_1^{(n)}$) calculated through Eq. (4.13) are used. The response of the piezo-stack actuator is then measured in three-dimensions (Fig. 4.4(b)) and the residual higher-order response terms corresponding to each harmonic is determined.

The second and higher order compensatory excitation components are obtained by adding a refining excitation component to the one lower order compensatory excitation as

$$\mathbf{V}_q^{(n)} = \mathbf{V}_{q-1}^{(n)} + \Delta \mathbf{V}_q^{(n)}. \quad (4.17)$$

Referring to Eq. (4.8) and associated simplification, the individual harmonic response to the refining excitation component is given by $\Delta \mathbf{\Gamma}_q^{(n)} = \mathbf{G}^{(1)}(n\omega_f, |\Delta \mathbf{V}^{(n)}|) \Delta \mathbf{V}_q^{(n)}$. The refining excitation $\Delta \mathbf{V}_q^{(n)}$ is selected such that this response compensates for the residual higher order terms measured as a result of the lower order harmonic compensation ($\mathbf{H}_{q-1}^{(n)}$). Accordingly, as depicted by Fig. 4.4(c), the refining excitation is calculated by solving $\Delta \mathbf{\Gamma}_q^{(n)} + \mathbf{H}_{q-1}^{(n)} = 0$ as,

$$\Delta \mathbf{V}_q^{(n)} = - \left[\mathbf{G}^{(1)} \Big|_{n\omega_f, |\Delta \mathbf{V}^{(n)}|} \right]^{-1} \mathbf{H}_{q-1}^{(n)}. \quad (4.18)$$

The compensation vectors of a particular order can then be calculated using Eq. (4.16) by dividing the calculated compensatory excitation by the amplitude of the fundamental excitation.

As a result of a step-sine testing procedure, the compensation vectors ($\lambda_{q,i}^{(n)}$) corresponding to a particular stack i are obtained at the tested fundamental frequencies for various orders q . This procedure is repeated to obtain $\lambda_{q,i}^{(n)}$ at different fundamental excitation amplitudes. Finally, the compensation vectors corresponding to all the stacks of

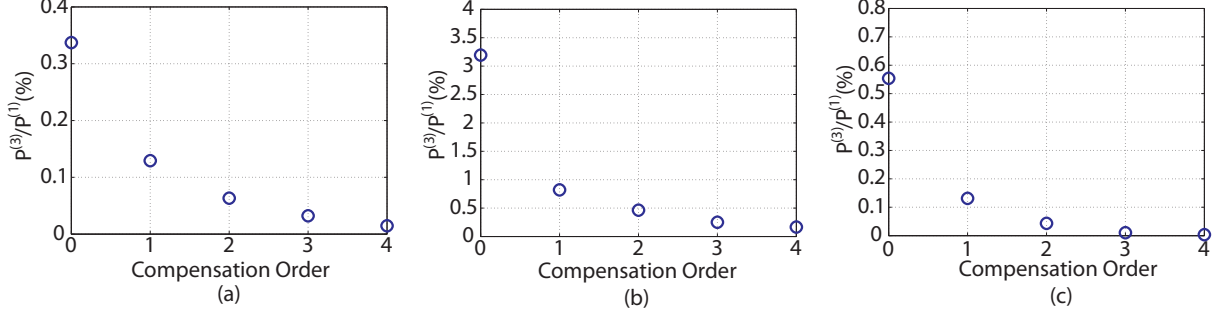


Figure 4.5: Reduction of the third harmonic response power through four levels of harmonic compensation for the cases where the y -stack of the actuator is excited with a fundamental excitation of 160 V amplitude at (a) 2.5 kHz (b) 3 kHz and (c) 3.5 kHz.

the actuator, and thus, the entire compensation matrix, can be obtained by supplying the fundamental excitation to each stack and following the same procedure.

Figure 4.5 illustrates the reduction of the third harmonic response power with higher-order harmonic compensation. Three cases with the highest residual harmonic response power in Fig. 4.3 are considered, where the single axis fundamental excitation with amplitude of 160 V and frequencies of 2.5 kHz, 3 kHz and 3.5 kHz are supplied to the y axis of the piezo-stack actuator. Order zero represents the case where no compensatory excitation is used. As shown, the harmonic response power is reduced to or less than 0.1% of the fundamental response power as a result of the fourth order harmonic compensation.

The complete procedure to determine the voltages that will be supplied to the piezo-stack actuator can be summarized as follows: For a specific desired motion, the complex amplitude vector corresponding to the fundamental excitation component ($\mathbf{V}^{(1)}$) is first determined through Eq. (4.12). Next, the complex amplitude vectors corresponding to the higher harmonic excitation components ($\mathbf{V}^{(n)}$) are calculated through Eq. (4.15) using the $\mathbf{V}^{(1)}$ vector. Since discrete levels of fundamental excitation amplitudes and fundamental frequencies are considered during the multi-level stepped-sine procedure, the compensation matrices are determined through spline interpolation. Accordingly, amplitude and phase of each element of the compensation matrices are interpolated with respect to the tested fundamental frequencies and the fundamental excitation amplitudes. From the complex amplitudes of the fundamental and compensatory excitation components, the time domain voltage signal to be supplied to each stack of the actuator can be constructed as,

$$v_i(t) = \sum_{n=1}^{n_{max}} |V_i^{(n)}| \sin(n\omega_f t + \angle V_i^{(n)}) \text{ for } i = x, y, z. \quad (4.19)$$

4.4 Evaluation of the control method

To evaluate the proposed open-loop control approach for generating 3D single frequency motions, a set of tests were performed on two different three-axis piezo-stack actuators. The evaluation tests were carried out by selecting different motion paths as targetted motions, calculating the required excitations using the presented approach, supplying those excitations to the actuators, and measuring the resultant motions. The measured motions are then compared to the targeted motions, and a quantitative assessment of the open-loop control approach is completed by using a set of quality metrics.

4.4.1 Experimental Details

Two three-axis piezo-stack actuators with different mechanical construction are tested. The first actuator (Actuator 1) is a three-axis piezo-stack actuator (Physik Instrumente PICA Shear Actuator P-123.01). The second actuator (Actuator 2) is constructed by manually combining the z -stack of P-123.01 with a two-axis piezo-stack actuator (Physik Instrumente PICA Shear Actuator P-112.01).

The first step for applying the presented open-loop control is the determination of dynamic response behavior in the form of hFRFs. This was accomplished by using the method outlined Chapter 3 above. An excitation frequency range of 1 kHz to 25 kHz and excitation amplitudes of 1 V, 10 V, 60 V, 110 V and 160 V are used during the characterization tests. The analysis of the obtained response indicated that for both actuators, the power contribution of the fundamental response component is more than 90% throughout the tested excitation frequency and amplitude ranges. The simplified response representation for each actuator is selected to include only the first five harmonic response components.

During all the evaluation tests, fourth-order harmonic compensation is used. To determine the compensation matrix $\mathbf{C}_4^{(n)}$ (see Eq. (4.15)), a set of stepped-sine tests was conducted for each actuator. Based on the excitation frequency range used during the characterization and the highest harmonic included in the response representation, a fundamental frequency range of 1 kHz to 5 kHz were considered at the excitation amplitudes of 1 V, 10 V, 60 V, 110 V and 160 V.

During the evaluation tests, the fundamental and compensatory excitations are calculated for a set of desired motions of various shapes and frequencies. Each calculated excitation is applied for a total duration of 1 s, and the actuator response is measured using the LDV-based measurement system. Hardware-synchronized digital excitation output

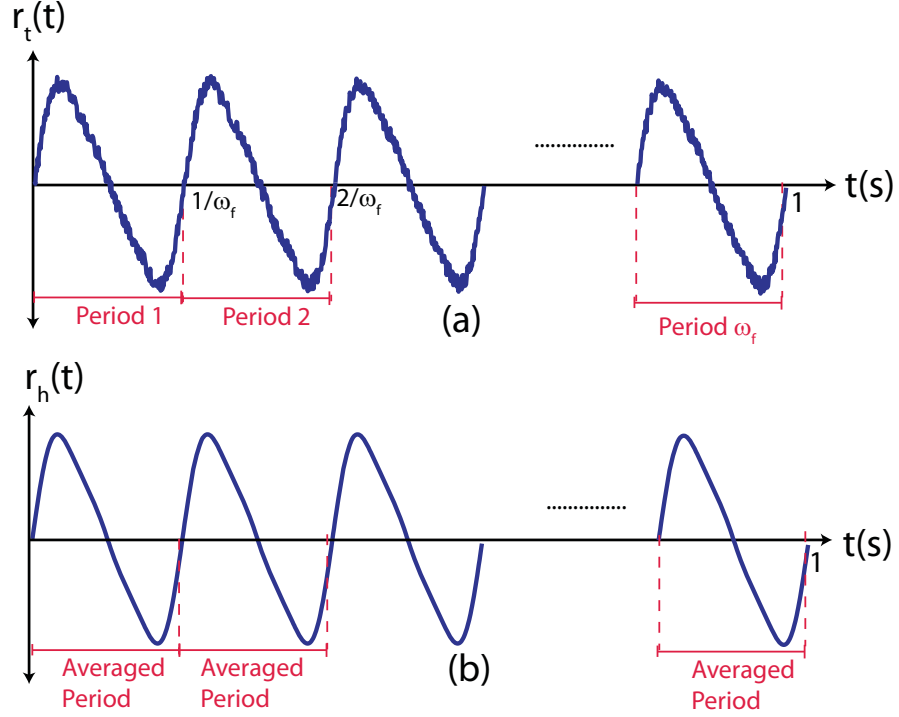


Figure 4.6: Determination of harmonic motions: (a)total motion (b)harmonic motion obtained as a result of the sample-by-sample averaging

and response acquisition are performed using a sampling rate of 400 kHz. The acquired responses are filtered through a zero phase-shift high-pass filter with a cut-off frequency of 1 kHz to eliminate the low frequency noise from the LDV system.

4.4.2 Evaluation Method

The motions measured during the evaluation tests are compared to the desired motions to evaluate the performance of the open-loop control method. To perform this analysis, each measured motion is decomposed into its harmonic and non-harmonic parts. Since the desired motions are purely harmonic, any deviation of the harmonic part of the motion from the desired motion is considered as the *harmonic motion error*. Similarly, the entire non-harmonic motion is considered as the non-harmonic motion error. The harmonic and non-harmonic motion errors are analyzed within the nominal motion frame of the desired motion along the $[\gamma, \eta, \zeta]$ axes (see Fig. 4.1) by performing a coordinate transformation between the measurement and nominal motion frames.

An accepted method for isolating the harmonic part of the measured motions in time domain is to use synchronous averaging [92]. This approach is illustrated in Fig. 4.6. The

measured response (after coordinate transformation) along a particular axis of the nominal motion frame is shown in Fig. 4.6(a), where the period of the motion at fundamental frequency is easily identified. Considering the fact that the sampling rate may not be an integer multiple of the period, the signal is resampled to obtain signals at specific time instants. The data corresponding to the same instant within each period is then averaged. Finally, the replicates of the averaged response period are combined back-to-back in time domain to construct the harmonic response of 1 s total duration as shown in Fig. 4.6(b).

The method used to evaluate the harmonic motions is described in Figures 4.7(a) and (b). The quantitative evaluation of the harmonic part of the motions is performed in polar coordinates within the nominal motion frame. The *actual path* is defined by the harmonic part of the measured motion. The *nominal path* is the desired motion path, which is parametrically represented by $d_\gamma(t)$ and $d_\eta(t)$ as given in Eq. (4.4). The descriptions in Fig. 4.7(a) are adopted from ISO 230-4:2005 standard [93] by extending the error definitions for the circular motions to those for general Lissajous-shaped motions. For this purpose, three additional paths having parametric representations that are scaled versions of that of the nominal path ($\alpha d_\gamma(t)$, $\alpha d_\eta(t)$) are defined: The scaling factors (α) for the two *minimum zone paths* are selected such that they envelope the actual path as shown. The *least-squares path* is obtained by selecting the scaling factor that minimizes the least-squares error between this path and the actual path. By definition, all the paths are concentric with the center located at (0,0) within the $[\eta, \gamma]$ plane.

The angular position θ of a particular point on any given path is defined as the angle between the γ axis and the vector connecting this point to the path center. The radial distance between the actual path and the nominal path at a given angular position is defined as the *radial deviation* $F(\theta)$, which has a positive value when the actual radial distance is larger than the nominal radial distance. The radial distance between the nominal path and the least-squares path is defined as the *mean radial deviation* $D(\theta)$, and the radial distance between the minimum zone paths is defined as the *path deviation* $G(\theta)$. Each quantity is normalized with respect to the radial distance of the nominal path $r(\theta)$, and the normalized quantities are denoted with an overbar. Since the minimum zone paths and the least-squares path are obtained by integer scaling of the parametric representation of the nominal path, \bar{D} and \bar{G} do not vary with angular orientation θ . Since the nominal motions are within the $[\gamma, \eta]$ plane, any non-zero motion along the ζ direction is considered to be entirely an error. This error is represented as a total *out-of-plane deviation* and denoted as N , (as seen in Fig. 4.7(b)). The out-of-plane deviation is normalized by the length of the nominal path defined by $L = 2 \max(r(\theta))$ to obtain normalized normal deviation (\bar{N}).

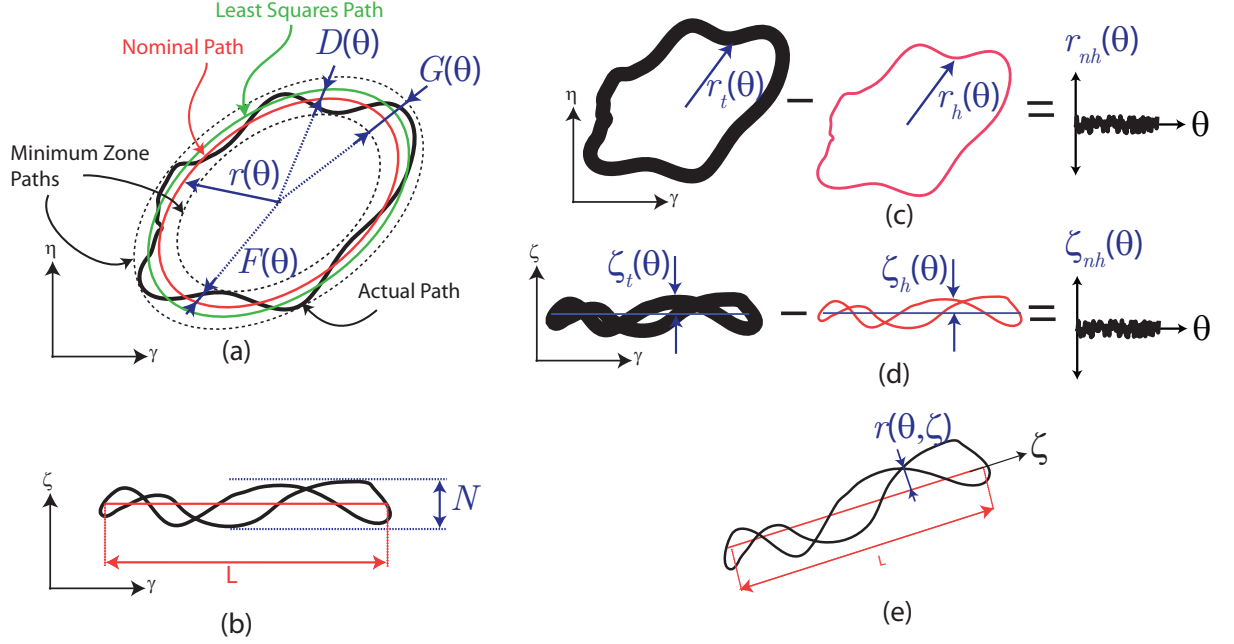


Figure 4.7: Definition of deviation metrics (a) In-plane harmonic evaluation metrics for non-linear motions (b) Out-of-plane harmonic evaluation metrics for non-linear motions (c) Determination of in-plane non-harmonic deviation (d) Determination of out-of-plane non-harmonic deviation (e) Harmonic evaluation metrics for linear motions

The non-harmonic part of the measured motions which, by definition, are error motions, are also determined in the polar coordinates. The radial non-harmonic motion ($r_{nh}(t)$) is calculated as the difference between the radial positions of the total ($r_t(t)$) and the harmonic motions ($r_h(t)$) at a particular angular position θ in the $[\gamma, \eta]$ plane, as shown in Fig. 4.7(c). The out-of-plane non-harmonic motion is defined as the difference between total and the harmonic motions along the ζ direction (see Fig. 4.7(d)). Considering the wide-band nature of the non-harmonic motions, *radial non-harmonic deviation* (σ_r) and *out-of-plane non-harmonic deviation* (σ_ζ) are defined as the standard deviations radial and normal non-harmonic motions, respectively.

For linear motions, the error descriptions given above cannot be applied since the nominal motion frame is not uniquely defined. Accordingly, measured linear motions are described in cylindrical coordinates $[r, \theta, \zeta]$, where the ζ axis is defined along the desired motion, as shown in Fig. 4.7(e). The normalized path deviation for linear nominal paths is calculated by dividing the diameter of the smallest cylinder that encloses the actual path by the nominal motion length ($\bar{G} = 2 \max(r(\theta, \zeta))/L$). The radial non-harmonic motion is similarly calculated as the difference between the total and the harmonic motions in cylindrical coordinates. The radial non-harmonic deviation is expressed as the standard deviation of the

Case	1	2	3	4	5	6
Actuator	1	1	1	1	1	1
D_γ (nm)	180	60	240	60	130	240
D_η (nm)	$120e^{j\frac{\pi}{2}}$	$120e^{j\frac{\pi}{3}}$	$120e^{j\frac{\pi}{4}}$	$60e^{j\frac{\pi}{2}}$	$130e^{j\frac{\pi}{2}}$	$60e^{j\frac{\pi}{2}}$
$\angle\zeta, x_m$ (deg)	0	0	90	90	90	90
$\angle\zeta, y_m$ (deg)	90	90	0	90	0	0
$\angle\zeta, z_m$ (deg)	90	90	90	0	90	90
Freq(kHz)	3	1.5	4	5	2.5	2
\bar{D}	0.1(0.6)	1.0(1.3)	0.9(1)	4.1(4.2)	0.2(0.8)	0.7(0.3)
\bar{G}	2.1(6.0)	2.4(3.0)	3.6(4.8)	5.8(6.1)	5.4(20.2)	2.4(15.4)
$\max(\bar{F}(\theta))$	1.2(4.4)	2.4(2.7)	3.0(2.8)	6.9(7.0)	2.4(10.2)	0.7(7.6)
$\min(\bar{F}(\theta))$	-0.9(-2.2)	-0.02(-0.3)	-0.6(-2.0)	1(0.8)	-3.0(-10.0)	1.7(7.8)
\bar{N}	3.2(5.6)	3.7(3.4)	1.1(0.8)	3.0(3.0)	2.3(8.2)	0.5(2.4)
σ_r (nm)	0.2(0.2)	0.6(0.7)	0.3(0.4)	0.2(0.3)	0.4(0.3)	0.6(0.3)
σ_ζ (nm)	0.2(0.2)	0.2(0.2)	0.3(0.3)	0.2(0.3)	0.2(0.2)	0.2(0.2)

Case	7	8	9	10	11	12
Actuator	2	2	2	2	2	2
D_γ (nm)	240	160	80	40	200	$10e^{j\frac{\pi}{2}}$
D_η (nm)	$240e^{j\frac{\pi}{2}}$	$80e^{j\frac{\pi}{2}}$	$160e^{j\frac{\pi}{6}}$	$160e^{j\frac{\pi}{2}}$	$140e^{j\frac{\pi}{3}}$	10
$\angle\zeta, x_m$ (deg)	54.74	70.53	48.19	65.91	48.19	45
$\angle\zeta, y_m$ (deg)	54.74	48.19	70.53	65.91	48.19	90
$\angle\zeta, z_m$ (deg)	54.74	48.19	48.19	35.26	70.53	45
Freq(kHz)	3	2.5	5	2.5	4	1.5
\bar{D}	0.3(0.01)	0.02(0.1)	0.1(0.4)	0.2(0.2)	0.5(0.2)	0.6(0.7)
\bar{G}	1.2(3.8)	1.5(5.1)	3.2(7.3)	1.8(3.7)	2.1(15.1)	4.0(3.8)
$\max(\bar{F}(\theta))$	0.2(1.5)	0.9(2.2)	2.0(4.2)	0.9(1.2)	0.5(7.9)	2.2(2.7)
$\min(\bar{F}(\theta))$	-1(-2.3)	-0.7(-2.9)	-1.2(-3.1)	-0.9(-2.5)	1.6(-7.2)	-1.8(-1.1)
\bar{N}	1.1(4.5)	1.1(2.2)	0.9(1.1)	0.6(1.4)	1.2(3.1)	1.7(1.7)
σ_r (nm)	0.2(0.3)	0.2(0.2)	0.5(0.4)	0.3(0.4)	0.4(0.4)	0.2(0.2)
σ_ζ (nm)	0.2(0.3)	0.3(0.3)	0.2(0.2)	0.2(0.3)	0.2(0.3)	0.2(0.2)

Table 4.1: Results of the evaluation tests for circular, elliptical and general Lissajous curve shaped motions. Error terms are given in percentages unless noted otherwise.

radial non-harmonic motion.

4.4.3 Results of the Evaluation Tests

In this section, the described evaluation method is used to assess the proposed open-loop control technique by testing two three-axis piezo-stack actuators. A number of single-frequency circle, ellipse, line or general Lissajous shapes, with different dimensions, are considered as the target motions. The nominal motion frames of target motions are varied to evaluate the 3D nature of the control approach.

Table 4.1 provides a quantitative evaluation of the measured actual paths with respect to

Case	1	2	3	4
Actuator	1	1	2	2
D_{x_m} (nm)	180	60	200	20
D_{y_m} (nm)	120	180	200	40
D_{z_m} (nm)	60	120	200	20
Freq(kHz)	5	4	2.5	3
\bar{G}	1.3(2.1)	2.3(2.4)	0.8(1.6)	1.6(2.1)
σ_r (nm)	0.8(1.4)	0.3(0.3)	0.4(0.9)	0.2(0.2)

Table 4.2: Results of the evaluation tests for linear motions. Error terms are given in percentages unless noted otherwise.

the circular, elliptical and general Lissajous shaped nominal paths for a number of representative cases with different fundamental frequencies. Similarly, evaluation corresponding to the tests with linear nominal paths is presented in Table 4.2. The nominal motion frame of each motion is identified by the angles between each of the measurement frame axes and the corresponding ζ axis. The η and γ axes are defined for each case through Gramm-Schmitt orthogonalization [60] of the x_m and y_m axes, respectively, with respect to the defined ζ axis. The values corresponding to each error metric are given in percentages. To study the effect of the compensatory excitation components, each test is conducted both with a fourth-order harmonic compensation ($\mathbf{V}^n = \mathbf{V}_4^{(n)}$) and without an harmonic compensation ($\mathbf{V}^{(n)} = 0$) and , the result of for the latter is given in parenthesis in Tables 4.1 and 4.2.

As a result of the evaluation tests corresponding to Actuator 1, the average values for the mean radial deviation \bar{D} and the normalized path deviation \bar{G} are 1.1% and 4.1%, respectively, after the harmonic compensation. Better performance have been achieved with Actuator 2, with the average values for \bar{D} and \bar{G} of 0.6% and 2.8%, respectively. The average normalized out-of-plane deviation \bar{N} are 2.0% and 1.0% for Actuator 1 and Actuator 2, respectively, after the harmonic compensation. Similar performance have been obtained for the motions with linear shape for which the normalized path deviation \bar{G} is shown to be below 2.3 % and 1.6 % for Actuator 1 and Actuator 2, respectively. The non-harmonic motion deviations for all cases (standard deviations corresponding to the broad-band non-harmonic response) are in sub-nanometer levels and do not show significant variation for different cases and actuators.

The inclusion of the harmonic compensation provided a large improvement on the accuracy particularly for a number of cases. For instance for case 11, the path deviation (\bar{G}) has been reduced from 15.1 % to 2.1 %. Similarly, the out-of-plane deviation has been reduced by the inclusion of the compensatory excitation components. As an example, the radial deviation ($\bar{F}(\theta)$) and the harmonic motion in $[\gamma, \zeta]$ plane for case 5 is given by Figures

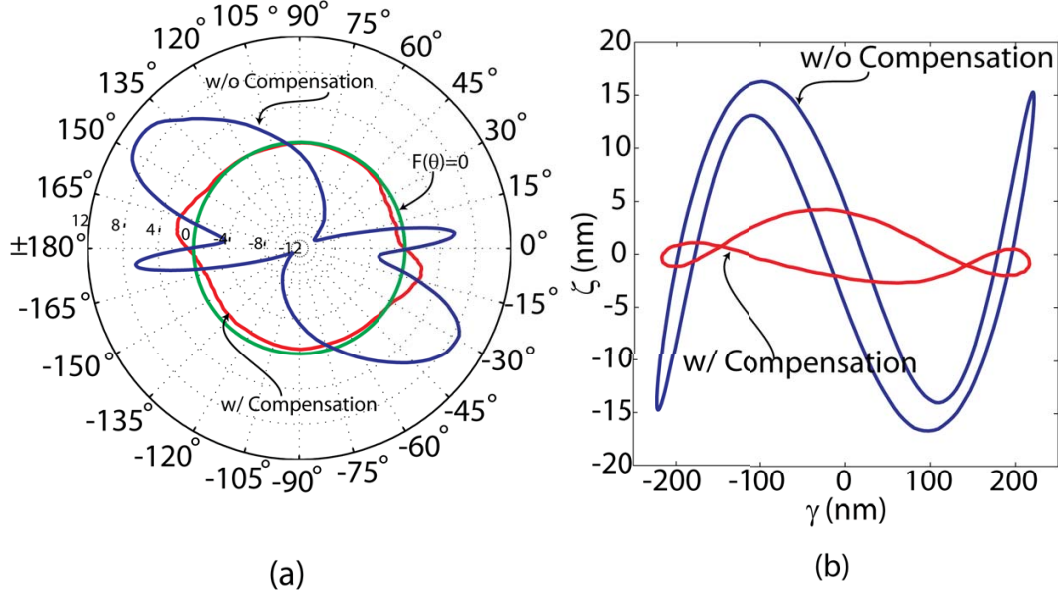


Figure 4.8: Effect of the compensatory excitation on the harmonic errors (a)Radial deviation ($F(\theta)$) plot ,all numbers are in percentile (b)Normal deviation

4.8(a) and (b), respectively. It should be noted for Fig. 4.8(a) that the negative values of the radial deviation is also included, and the zero deviation circle is explicitly shown.

This evaluation shows that the presented harmonic excitation method was able to reduce the higher harmonic response components successfully. Harmonic compensation does not provide significant improvement for the cases especially where the size of the targetted motions are small (e.g. cases 4 and 12). For those cases, both the amplitude of the determined fundamental excitation components and the corresponding harmonic distortions are relatively small, indicating that the behavior is linear and a single frequency excitation is sufficient to achieve the required accuracy.

Frequency domain analysis of the the motion errors showed that after the harmonic compensation, the residual motion errors occur mostly at the fundamental motion frequency. This may be attributed to uncertainties in the obtained fundamental FRFs arising from (i) measurement errors during the characterization and the evaluation tests (see Section 4.5) and (ii) small variations of the actuator characteristics due to environmental disturbances (e.g. temperature fluctuations).

4.5 Analysis of Measurement Errors

The fidelity of the presented control method depends critically upon the accuracy of the performed measurements. In particular, there are three possible error sources that could affect the measurements: (1) Electrical noise and errors of the LDV controller/decoder and of the data acquisition system; (2) optical reflection, focusing and mutually-orthogonal alignment of the LDVs, and (3) motions of the measurement frame as a response to piezo-stack excitations and external noise. As noted earlier, the motion measurements are contaminated with the noise arising from the LDV below 1 kHz (addressed using a high-pass filter). Above 1 kHz, the main contributor of the measurement error is the vibrations of the measurement frame. Although a formal uncertainty quantification including an analysis of contribution from each of those sources is beyond the scope of this work, an experimental analysis of cumulative measurement errors from all of the aforementioned sources is conducted to enable assessing the measurement technique.

The errors corresponding to the determination of harmonic response components have been characterized in [91]. It was shown that the fundamental response component can be characterized with FRF amplitude errors less than 0.6 nm corresponding, to less than 1.6% of the measured amplitude. The amplitude errors corresponding to the higher harmonic components was seen to be less than 0.01 nm.

To experimentally characterize the cumulative measurement error, a number of tests are conducted where the Actuator 2 is excited to generate a select set of motions targeted during the evaluation tests. Each of the three lasers is shined onto a large steel mass (100 mm x 130 mm x 300 mm) that is bolted down on the optical table. Since the relative vibrations between the large mass and the optical table can be assumed to be negligible in this configuration, any non-zero displacement measurement may be considered as the cumulative measurement error.

For the measurements above 1 kHz, the results of measurement error characterization tests are processed to determine their contribution to the evaluation metrics explained in Section 4.4.2. The average contribution of the measurement error on the radial deviation, mean radial deviation, path deviation and normal deviation are determined as 0.05 %, 0.02 %, 0.12 % and 0.03 %, respectively. The largest contribution of the measurement error is determined to be in the fundamental frequency ranges that include several resonant frequencies of the measurement frame. This observation highlights the significant contribution of the frame vibrations on the measurement errors. The average radial and normal non-harmonic deviation corresponding to the measurement error is found to be 0.16 nm and

0.12 nm, respectively. These deviations are more than 50% of the non-harmonic deviation values determined during the evaluation tests, which shows that measurement error is the main contributor of the non-harmonic motion deviations.

4.6 Summary and Conclusions

This chapter presents an open-loop method to control multi-axis piezo-stack actuators in generating accurate three-dimensional single-frequency motions. In determining the necessary excitations, the presented method utilizes the frequency domain representation (in the form of hFRFs) of the piezo-stack actuators obtained from an experimental dynamic characterization. The proposed method for generating the desired responses involves excitation of the actuator at the fundamental (motion) frequency to obtain the desired response and inclusion of a compensatory excitation at the higher harmonics of the fundamental frequency to reduce or eliminate for the higher harmonic response components. Fundamental component of excitation is directly determined using the inverse of the fundamental FRF matrices and the desired response. A multi-order method is used for the harmonic compensation, where the first order compensatory excitation components can be analytically calculated using the higher harmonic FRFs (hFRFs). An experimental procedure is outlined for determining the higher-order compensatory excitation components. The accuracy of the proposed method is then studied through a set of evaluation tests that are conducted on two different three-axis piezo-stack actuators, where motions with different shape, size and frequencies are targetted, and response of the actuators to corresponding excitations are measured. The results of the evaluation tests are processed to determine the harmonic and non-harmonic motion errors.

The harmonic motion errors are evaluated through a number of error metrics defined in this work for target motion amplitudes 10 nm to 240 nm. For Actuator 1, 1.1% average mean radial deviation, 4.1% average path deviation and 2.0% average normal deviation is reported. Better performance is achieved with Actuator 2 for which 0.6% average mean radial deviation 2.8% average path deviation and 1.0% average normal deviation is reported. The harmonic compensation successfully reduced the unwanted higher harmonic response components to acceptably low levels, resulting in more than 75% reduction in path deviation. Sub-nanometer levels of radial and out-of-plane non-harmonic deviations were observed for all cases. An analysis of measurement errors showed that the major contributor of the determined non-harmonic deviations is the measurement error.

The presented method provides a means of controlling the single-frequency dynamic mo-

tions of piezo-stack actuators with high accuracy at nanometric levels. Due to its open-loop nature, the the presented method requires extensive dynamic characterization. However, depending on the accuracy requirements, the ranges of fundamental motion frequency and size, satisfactory results can be obtained with no or low orders of harmonic compensation, which considerably reduces the experimental characterization requirements. Particularly, first-order harmonic compensation which reduces the harmonic response power by more than 80% for many cases, does not necessitate the use of the iterative compensatory step-sine testing procedure.

Chapter 5

Evaluation of the Dimensional Accuracy and Shape Capability

In this chapter, we present a dimensional accuracy evaluation of the nanomilling system through examination of various nanomilled feature geometries on poly(methyl methacrylate) (PMMA) samples. Furthermore capability of nanomilling to create complex shapes, as well as the preliminary observations on the material removal mechanism and feature quality is presented. Through the findings of this work, (1) the dimensional accuracy of the nanomilling process is quantified (2) the hypothesis, "implementation of the high-stiffness nanotool assembly and the controlled nanotool motions will improve the dimensional accuracy and widen the shape capability", is verified.

First, the capability of the system and the nanomilling process in accurately prescribing depth of removal for both in-plane and out-of-plane configurations is evaluated. Next, the ability to fabricate varying feature widths during a single tool-pass when using the in-plane configuration is analyzed. Finally, we demonstrate the general capability of the nanomilling system and process to create complex feature shapes. During these analysis, a silicon AFM tip with a nominal (fresh) radius of less than 10 nm is used. The nanotool motions are prescribed considering the motion control and compensation approaches presented above.

5.1 Accuracy of Feature Depth

To evaluate the depth-prescription capability during the in-plane configuration, a set of seven side-by-side parallel steps with varying depth and 1 μm nominal width were created using circular nanotool motions (in the $x_s - y_s$ plane) with 200 nm diameter at 5 kHz

Prescribed Depth (nm)	50	80	100	80	50	0
Measured Depth (nm)	50.2	80.9	101.1	80.1	51.3	2.5
Standard Deviation (nm)	4.8	3.6	3.6	3.6	4.1	4.5

Table 5.1: Prescribed depths, average depths, and standard deviation of the steps created during in-plane nanomilling.

rotational frequency, while feeding the sample along the x_s direction. As described above, the removal depths for the in-plane configuration are prescribed by the nanopositioning stage. Figure 5.1 shows the AFM image of the fabricated steps and the average cross-sectional profile. The relative average depths of the steps are calculated by comparing the distances between the parallel planes that are determined through curve fitting to each step. To eliminate the uncertainties arising from surface irregularities and contact detection, the first created step (marked as 1 in Figure 5.1) is considered as the reference, and the relative depths of the following steps are determined accordingly. The standard deviation of measured surface points around the fitted planes were also calculated. As seen in Table 5.1, the measured average depths are within 2.5 nm (corresponding to less than 3% error in average depth) with standard deviations less than 4.8 nm, which are comparable to the repeatability of the nanopositioning stage.

In order to assess the capability to control the depth of a created channel during the out-of-plane configuration, channels with different depths were created using circular out-of-plane nanotool motions. It should be noted that, for small depths created through a single tool-pass using the out-of-plane configuration, the depth of removal is prescribed by the piezoelectric actuator (nanotool motions), rather than by the nanopositioning stage as in the in-plane configuration. Three channels were created using out-of-plane circular nanotool motions (in the $y_s - z_s$ plane) with radii 80, 120 and 160 nm at a frequency of 5 kHz, while feeding the sample along the y_s direction. To eliminate the uncertainties arising from surface irregularities and contact detection, first a reference surface is created with a circular out-of-plane motion with 20 nm radius. The channels are then created on the created reference surface. Since the center of the motion is 20 nm above the reference surface, those motions correspond to prescribed depths of 60, 100 and 140 nm, respectively. An AFM image and an average cross-sectional profile of the created channels are given in Figure 5.2. The averaged cross-sections are calculated by averaging the measured channel profiles at a large number of cross-sections. The measured average depths of three channels were seen to be 62.39, 100.97 and 143.64 nm. Thus, depths can be prescribed with less than 4 nm, which is comparable to the the uncertainty level that can be achieved for the direct prescription of depth using the nanopositioning stage.

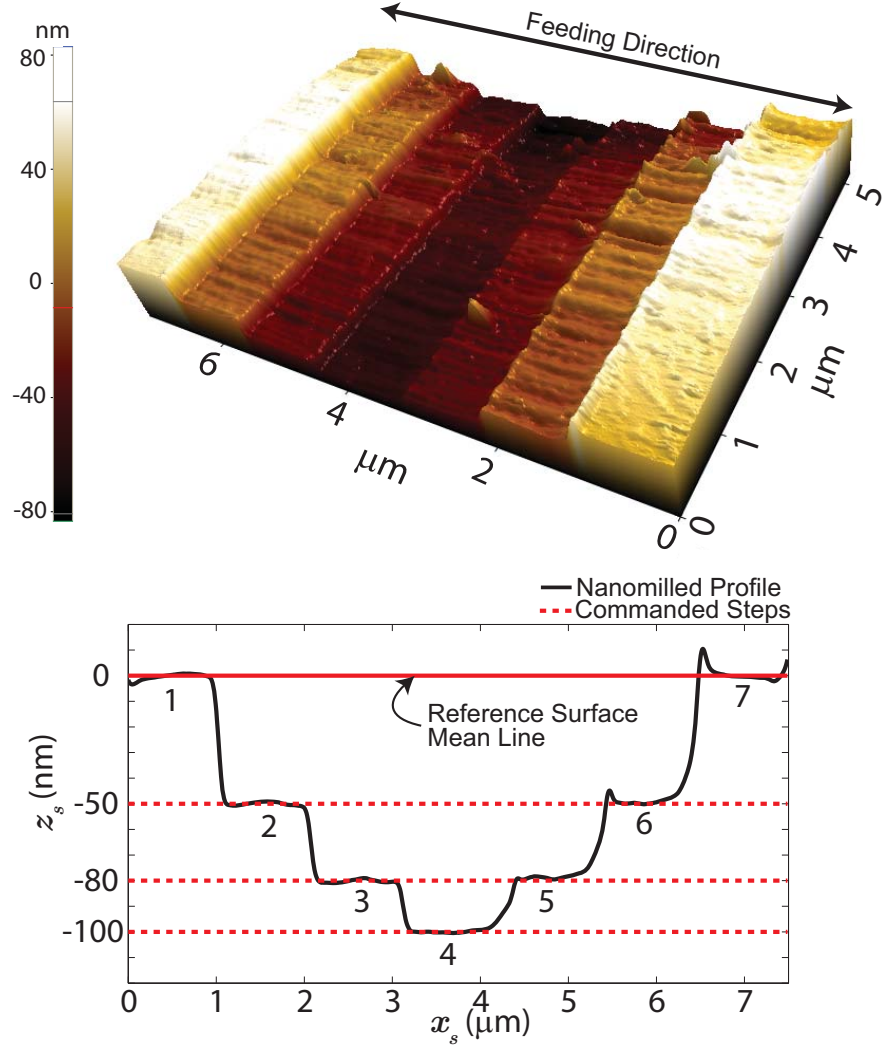


Figure 5.1: An AFM measurement of the steps created on a PMMA surface using the in-plane configuration of the nanomilling process for evaluation of the depth prescription.

5.2 Accuracy of Feature Width

Next, to evaluate the capability of assessing varying widths during a single tool pass of the in-plane nanomilling configuration, channels with linearly increasing width are created. Circular nanotool motions (in the $x_s - y_s$ plane) with frequency of 5 kHz and with increasing

Channel Number	1	2	3	4
Width-Increase Rate (nm/ μm)	51.05	54.71	50.58	54.13
Mean Width Variation (%)	3.15	1.44	2.28	2.41

Table 5.2: The width-increase rates and associated width variation for four V-shaped channels nanomilled using the in-plane configuration to assess the single-pass width capability.

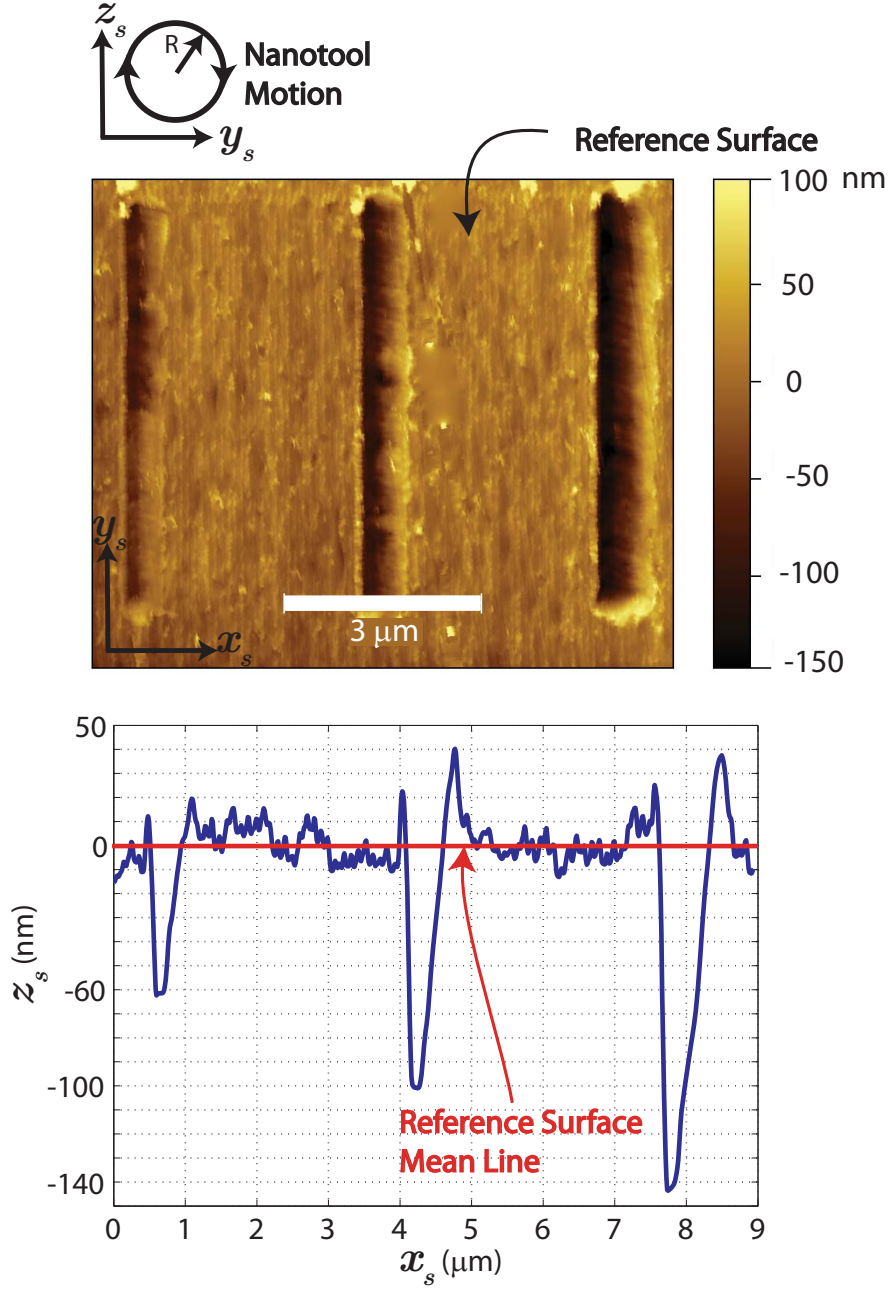


Figure 5.2: An AFM measurement of three channels created on a PMMA surface using the out-of-plane configuration of the nanomilling process. The horizontal axis of the bottom figure is compressed to show all three channels.

diameters from 0 to 320 nm are generated while feeding the sample along the x_s direction to create a $6 \mu\text{m}$ channel, yielding a prescribed width-increase rate (twice the slope of the sidewalls) of $53.3 \text{ nm}/\mu\text{m}$. An AFM image of one of the created channels and the cross-sectional data at certain locations along its length are given in Figure 5.3. The height

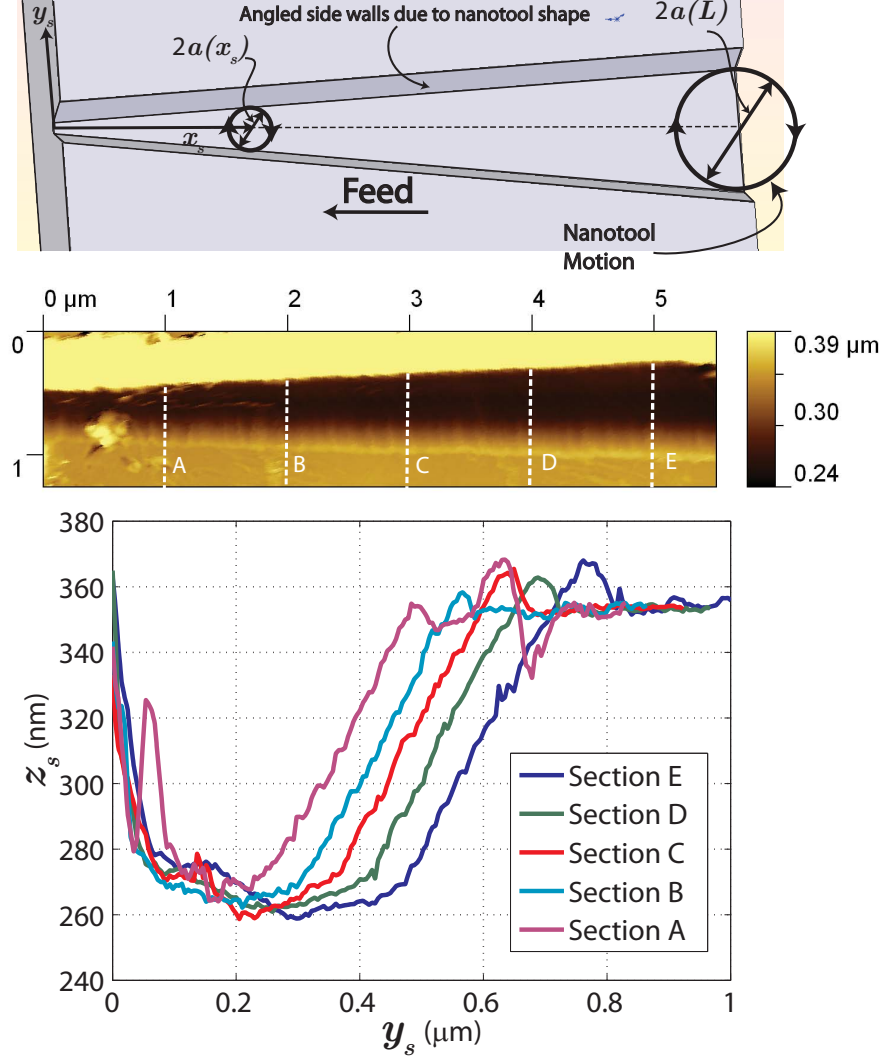


Figure 5.3: The V-shaped trench created to demonstrate the different-width capability during a single nanotool-pass using the in-plane nanomilling configuration.

variation caused by a large chip that is stuck to the top side of the wall is neglected by saturating the color of the AFM image. Considering a plane 60 nm above the channel bottoms as a reference, the resulting width-increase rate are calculated through curve fitting of two lines to the side walls of the channel. The mean of the (absolute value of) width variation with respect to the fitted lines along the channel are also calculated. The results obtained for four of the channels created through this procedure are given in Table 5.2. The presented results show that the targeted width-increase rate can be achieved within 3 nm/ μm . The noted width variation along the channels is potentially due to mechanical factors such as the material removal mechanism, which will be addressed in future research.

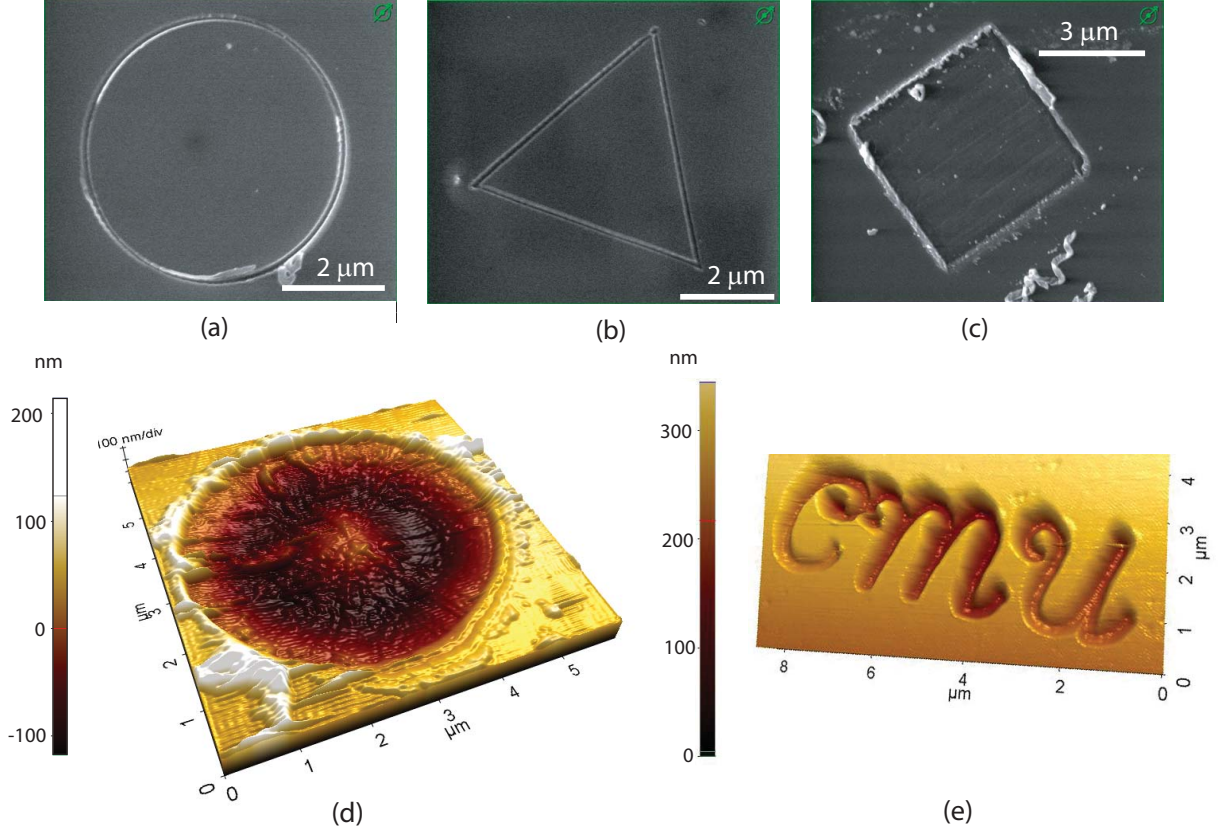


Figure 5.4: Various features created by nanomilling

5.3 Shape Capability of Nanomilling

Using the presented nanomilling system and procedure, a number of features with different shapes have been created. Fig. 5.4 shows SEM images of the created features, including a $5\ \mu\text{m}$ diameter circle with 30 nm depth, fabricated by circular in-plane motions of 3 kHz frequency and 100 nm diameter (5.4(a)); an equilateral triangle with $5\ \mu\text{m}$ side length and 30 nm depth, fabricated by circular out-of-plane motions of 3 kHz frequency and 100 nm diameter given by 5.4(b) (rotation center is set to be 20 nm above the sample surface); and a $4.5\ \mu\text{m}$ by $4.5\ \mu\text{m}$ square pocket with a 100 nm depth fabricated by circular in-plane motions of 3 kHz frequency and 100 nm diameter (5.4(c)).

Two of the more complex features including the cursive letters CMU (Figure 5.4 (d)) and a circular recess with radially changing depth (in a sinusoidal fashion, see Figure 5.4 (e)) were also nanomilled. The in-plane nanotool configuration with 100 nm diameter circular motions at 5 kHz rotational frequency is used in each case. The depth for the text CMU and the peak to valley depth variation for the circular recess are set to be 100 nm. The circular recess was nanomilled by feeding the nanotool along the radial direction while changing the

depth normal to the sample surface sinusoidally, and repeating this step at every angular increment.

During the creation of the presented features a G-code like programming is used through the aforementioned LabViewTM based software to impose the necessary feeding and nanotool motions. It is seen that the complex shapes such as these can be successfully fabricated by nanomilling. The in-depth analysis of dimensional accuracy of the created features through nanomilling is presented in Chapter 5

5.4 Observations on Material Removal Mechanism

One of the premises of the nanomilling process is the effective removal of the material mainly in the form of a chip, rather than only ploughing the material [21,22]. To demonstrate the material removal characteristics, an SU-8 sample surface was nanomilled to create channels with 5 μm length and 100 nm depth using each of the in-plane and out-of-plane configurations (5.5). For the in-plane configuration, the nanotool was rotated using a 100 nm circular motion at 3 kHz frequency. For the out-of-plane configuration, the elliptical nanotool motion included a normal (to the surface) diameter of 40 nm and a feeding-direction diameter of 100 nm at 3 kHz frequency. As a reference, channels were also fabricated without a nanotool-motion (i.e., by scratching). A commercial silicon probe tip with a pyramidal shape and 10 nm nominal tip radius was used as the nanotool. Due to the potential effect of nanotool orientation, three feeding directions were tested. It can be seen that the in-plane and out-of-plane nanotool motions facilitated material removal in the form of long, curled chips, and produced well-defined edges of the channels. Scratch (no-motion) configuration, on the other hand, did not produce chips in a consistent manner, and resulted in reduced edge definition, indicating a removal process with dominant ploughing effects.

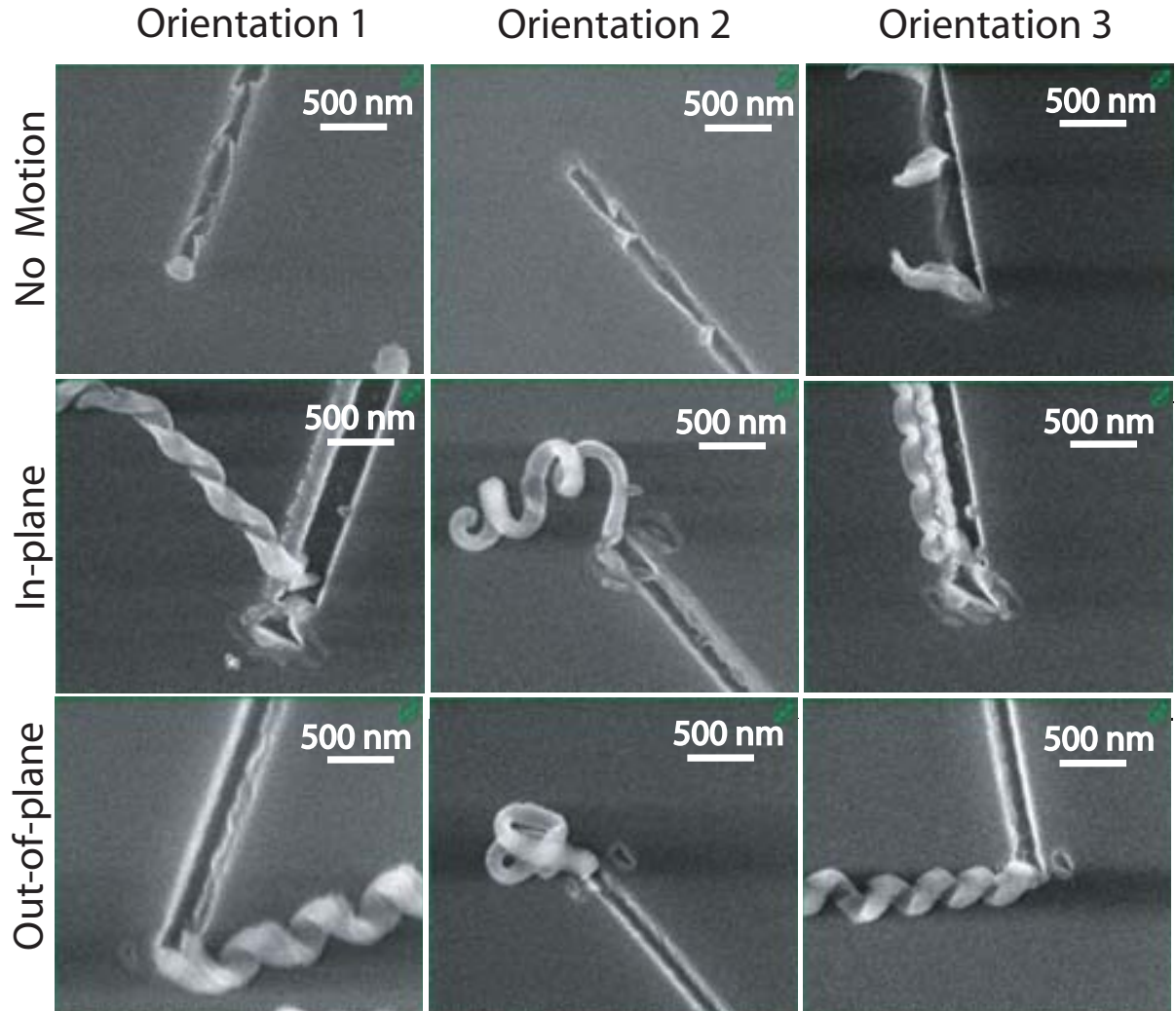


Figure 5.5: SEM images of the channels created using different nanotool motions. The long and curled chips observed for the cases with nanotool motions indicate that the material removal mechanism is shearing dominated. No-motion (scratch) case does not produce chips consistently, indicating the dominance of the ploughing mechanism.

Chapter 6

Preliminary Analysis of Nanotool Wear

This chapter presents the preliminary work towards the development of the methodology for quantitative analysis of nanotool wear. This experimental study involves atomic force microscopy analysis of the nanotools after they are used to remove material through nanomilling. Initial findings on nanotool replication to facilitate the understanding of wear progression during nanomilling is also presented. This study constitutes the groundwork for a more comprehensive analysis of nanotool wear and its relation to various process parameters.

6.1 Experimental and Analysis Method

A number of representative nanomilling tests are conducted to study nanotool wear. During these tests, a set of linear channels are nanomilled on a copper surface. The workpieces are prepared through physical vapor deposition (PVD) of copper on silicon wafers, generating surfaces with less than 5 nm Ra roughness. Single crystal diamond AFM tips with nominal radius of 50 nm are used as nanotools. The diamond nanotools are of four-faced pyramidal shape with a nominal height of 5.6 μm . The process parameters used during the experiments are summarized in Table 6.1. The feeding direction is kept constant during nanomilling of the channels throughout the experiments. To avoid abrupt tip damage during depth prescription, the depth of removal is gradually increased from 0 to 120 nm while feeding the nanotool along the first 1 μm length of the created channels as shown in Fig 6.1.

To characterize the nanotools and determine the wear volumes, the nanotools are imaged

Channel Length	10 μm
Channel Depth	120 nm
Nanomilling Configurations	In-plane/Out-of-plane
Nanotool motion shape	Circular, 100 nm radius
Nanotool motion frequency	4000 Hz
Material removal rate (for a feed rate of 60 $\mu\text{m/s}$)	15 nm/rev

Table 6.1: Experimental parameters used during the characterization of the piezo-stack actuators.

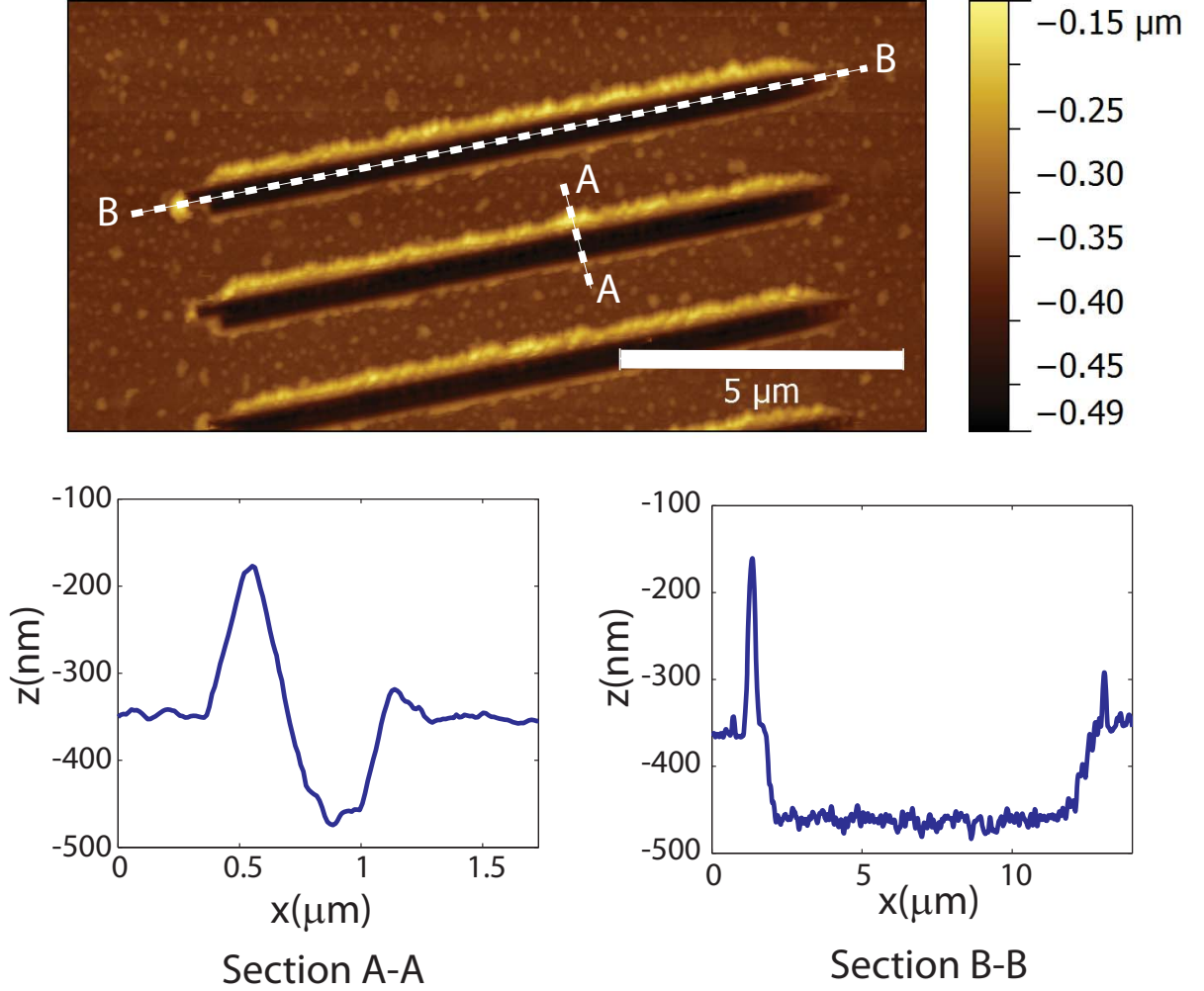


Figure 6.1: AFM image of the channels created during the wear tests

using non-contact AFM before and after the experiments are conducted. Silicon AFM probes having a nominal tip radius less than 10 nm are used for measurement purposes. Representative AFM images of a fresh (unused) diamond nanotool is given in Fig 6.2. For each nanotool, a 5 μm x 5 μm area around the tip apex, corresponding to a total height of around 3 μm is first imaged. The topography data is acquired with a spatial resolution of

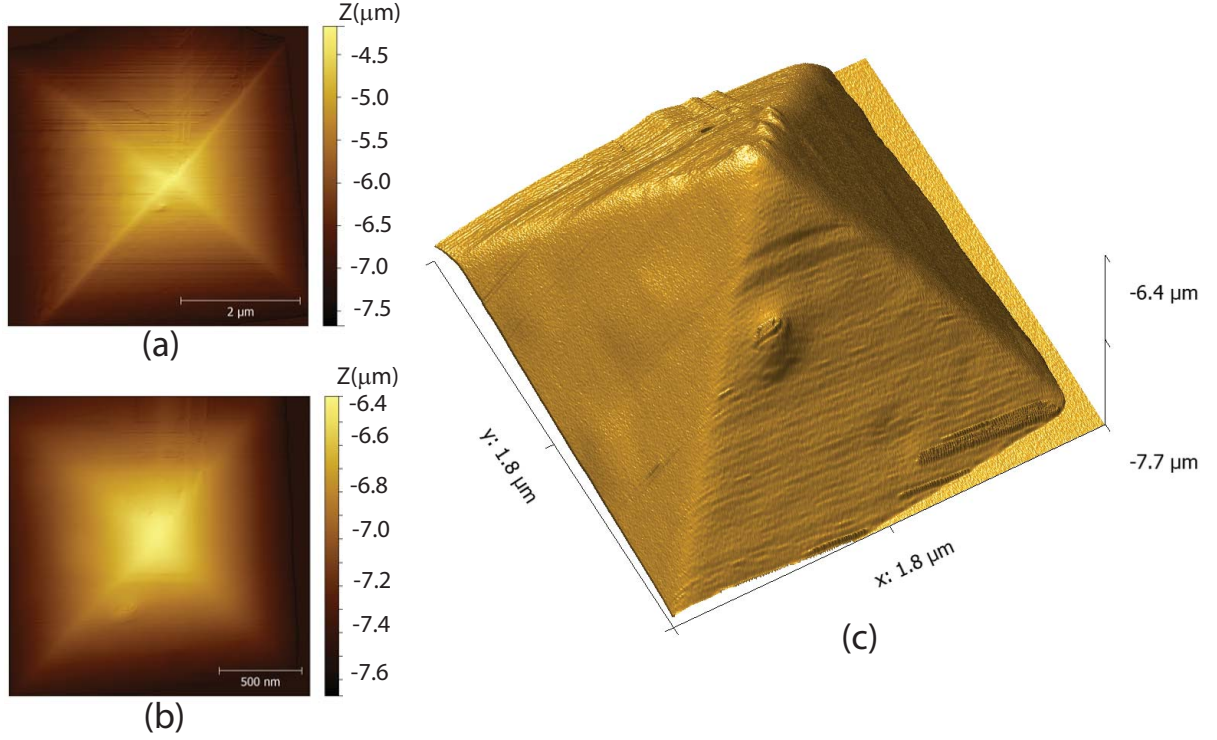


Figure 6.2: AFM images of an unused diamond nanotool (a) Low resolution image (b) High resolution image (c) Three dimensional representation of the high resolution image

20 nm for this first (low resolution) image. Next, a second scan is performed within a $1.8 \mu\text{m} \times 1.8 \mu\text{m}$ area around the tip apex, corresponding a total height of $1 \mu\text{m}$. The spatial resolution is improved to 7 nm for the second (high resolution) image.

To calculate the wear volume, the three-dimensional AFM data corresponding to the unused and worn phases of the nanotools are correlated to each other. Since the low resolution images include the unworn regions of the nanotool well below the apex, they are used for the purpose of image correlation. To correlate the unused and worn nanotool images, first the angular misalignments between the before and after images (arising due to mounting errors during the measurements) are corrected. Orientation of a given AFM image is indicated by three vectors that are normal to three faces of the pyramidal nanotools. To determine these vectors, least square plane fitting is applied to low resolution AFM image data within the planar regions more than $2 \mu\text{m}$ below the nanotool apex (unworn regions). Next, angles of rotation around three mutually orthogonal axes to be imposed on the worn nanotool image are determined such that the angles between the corresponding plane normals of the unused and the (rotated) worn nanotool images are minimized. Nelder-Mead simplex direct search optimization algorithm is used to determine the rotation angles. Following the angular alignment, spatial offsets between the planar regions of the aligned low resolution images

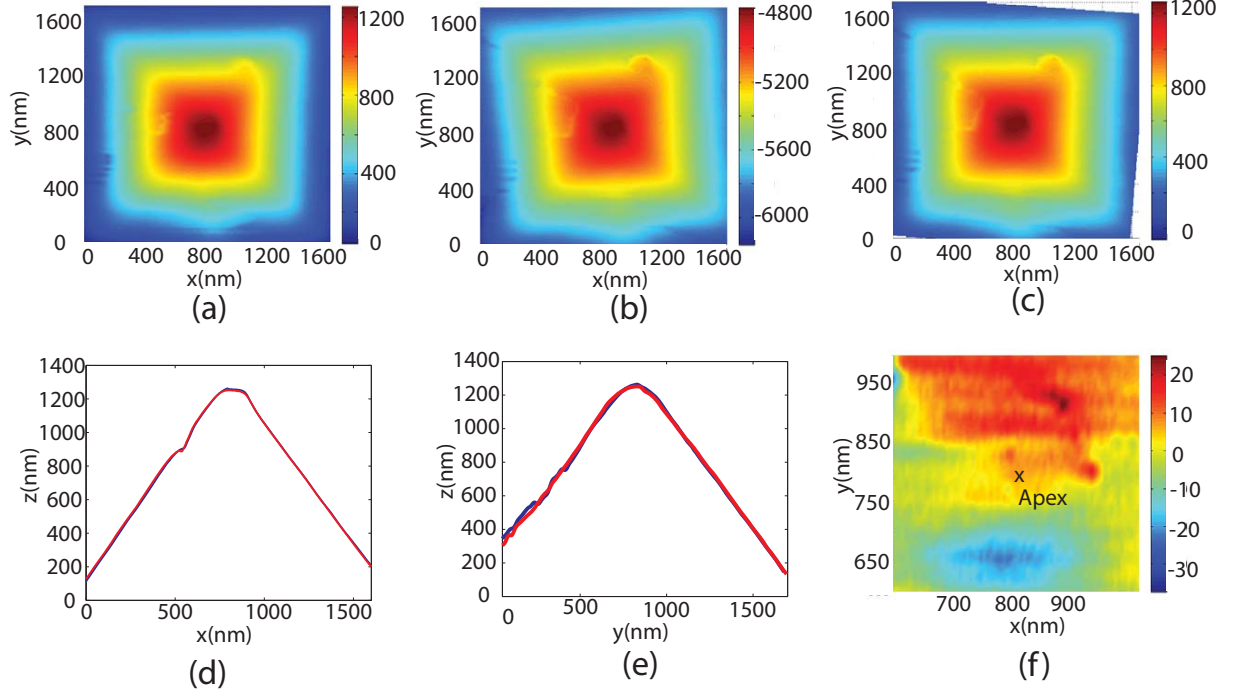


Figure 6.3: The result of the correlation of two AFM images corresponding to the same nanotool, (a) First high resolution image (b) Second high resolution image before angular and translational alignment, (c) Second high resolution image after the alignment, (d-e) Cross-sectional data corresponding to the aligned images around the apex along the X and Y axes, (f) The height difference map of the aligned images.

are determined. These offsets are calculated through the same optimization algorithm such that the distances between the corresponding planar regions are minimized when they are imposed on the worn nanotool image. Determined rotation angles and offsets are then imposed the high resolution image of the worn nanotool. Finally, the wear volume is calculated by the double-integration of the height difference between the aligned high-resolution images around the nanotool apex.

To evaluate the performance of the explained correlation, two separately obtained images of the same unused nanotool are correlated. The results of the correlation is summarized in Fig. 6.3. Comparing figures 6.3(a) and (b), angular misalignments can be noted between the two images that are corrected through the correlation algorithm as shown in Fig. 6.3(c). The three dimensional map of the height difference between the correlated AFM images around the apex region is given in Fig. 6.3(f). The mean value and the standard deviation of the height difference within this region is determined to be 2 nm and 12 nm, respectively. The highest discrepancies between the images are observed within the regions where the AFM images exhibit abrupt changes with high spatial frequencies where the accuracy of AFM

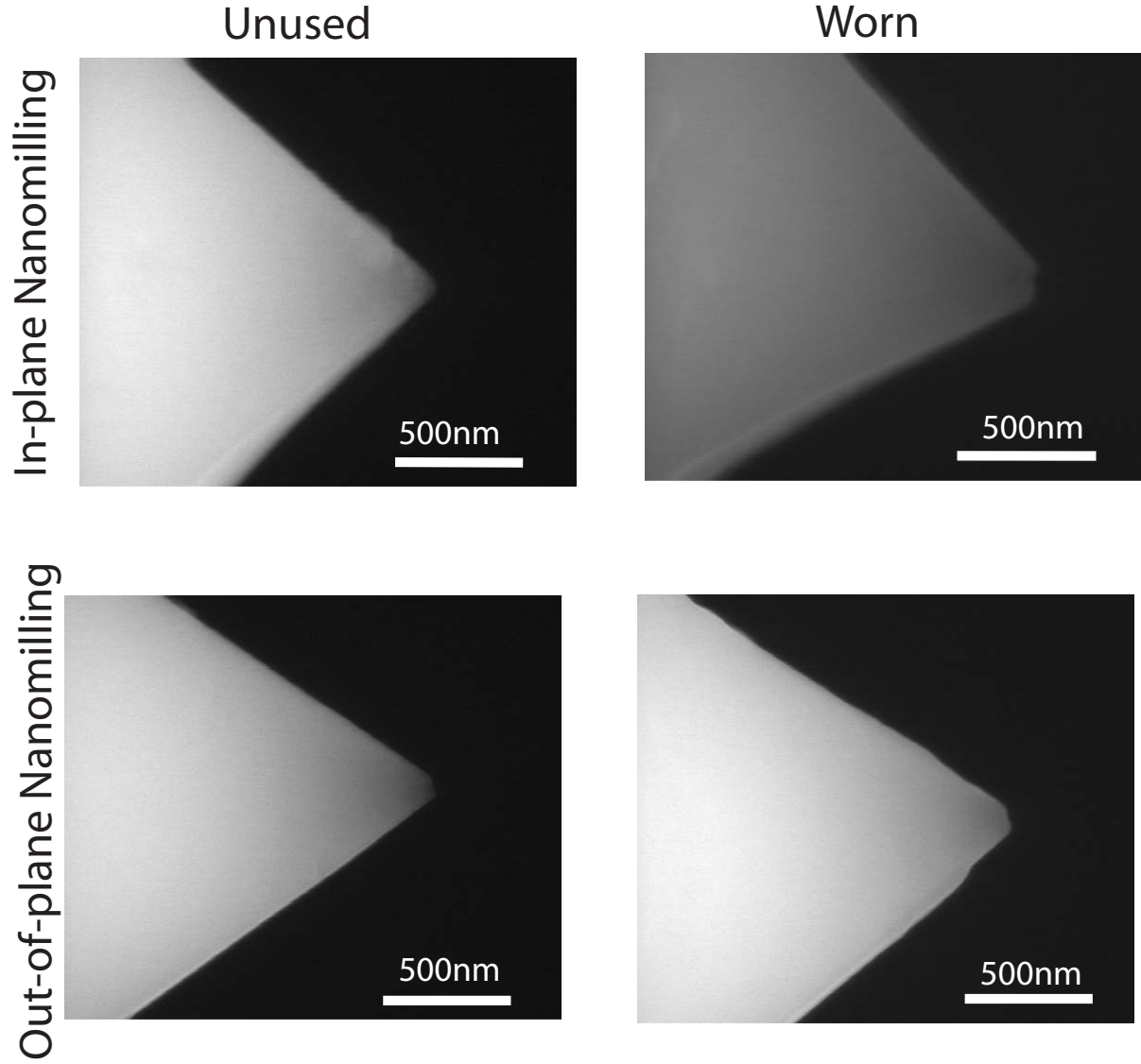


Figure 6.4: SEM images of the unused and worn nanotools

imaging is lower. Since the volumetric difference can be captured through low frequency spatial data, this issue can be addressed by low-pass spatial filtering of the images. In fact, when the correlation is applied to the images after two dimensional low-pass filtering, the mean value and the standard deviation of the height difference is reduced to less than 1 nm and 6 nm, respectively.

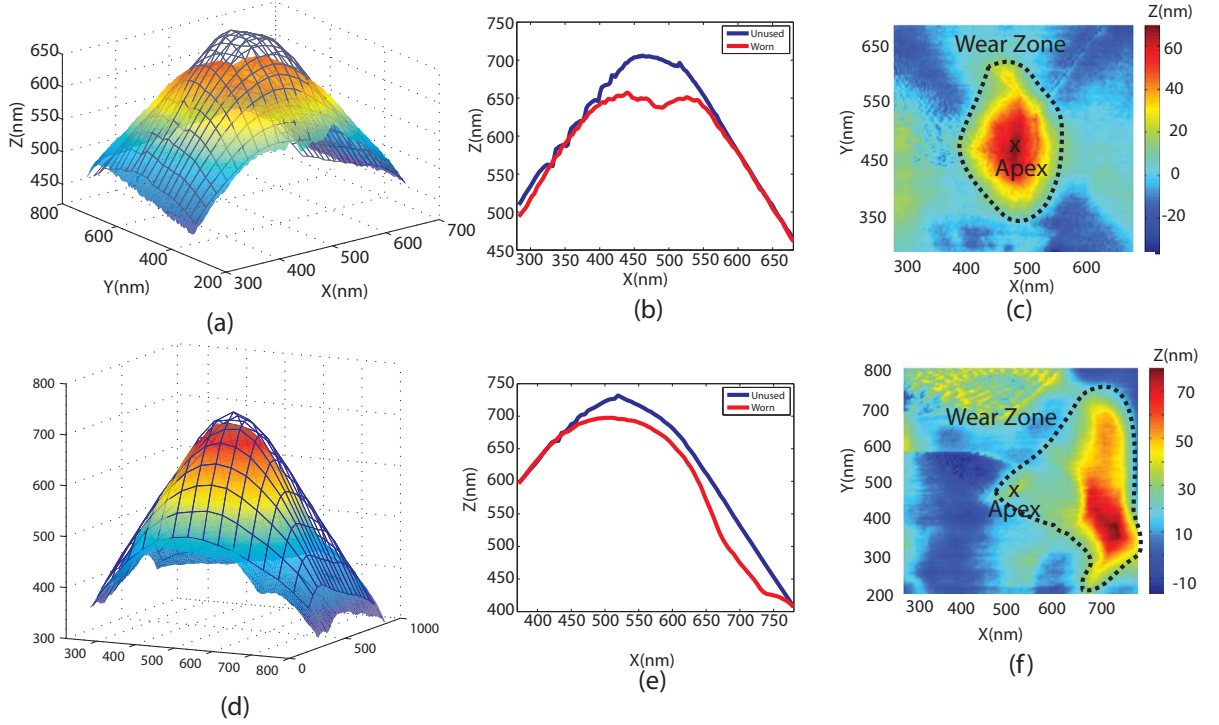


Figure 6.5: Results of the wear experiments. Three dimensional images of the nanotool before and after nanomilling in the (a) in-plane (d) out-of-plane configurations, the unused nanotool is depicted by a wireframe representation. Cross sectional images of the unused and worn nanotools after nanomilling in the (b) in-plane (e) out-of-plane configurations. Height difference maps around the nanotool apices after (c) in-plane (f) out-of-plane nanomilling.

6.2 Results

Discernible wear of the nanotools have been observed as result of the in-plane and out-of-plane nanomilling tests after nanomilling of 100 channels (corresponding to a total nanomilling length of 1 mm). The scanning electron microscopy images of the unused and worn nanotools used during these experiments is given in Fig. 6.4.

Results of the AFM analysis of the wear exhibited as a result of the the nanomilling tests is given in Fig. 6.5. As shown in Figures 6.5(a)-(c), following the in-plane nanomilling tests, wear is localized around the apex of the nanotool within around a 200 nm X 200 nm area, leading to a total height change around 50 nm. For this case, the total wear volume is calculated as $7.8 \times 10^5 \text{ nm}^3$. Figures 6.5 (d)-(f) indicate that as a result of the out-of-plane tests, nanotool wear occurred both at the apex and one of the faces of the nanotool. In fact, the wear is observed on the face that is in direct interaction with the workpiece material due to the selection of feed and nanotool rotation directions. For this particular case, the

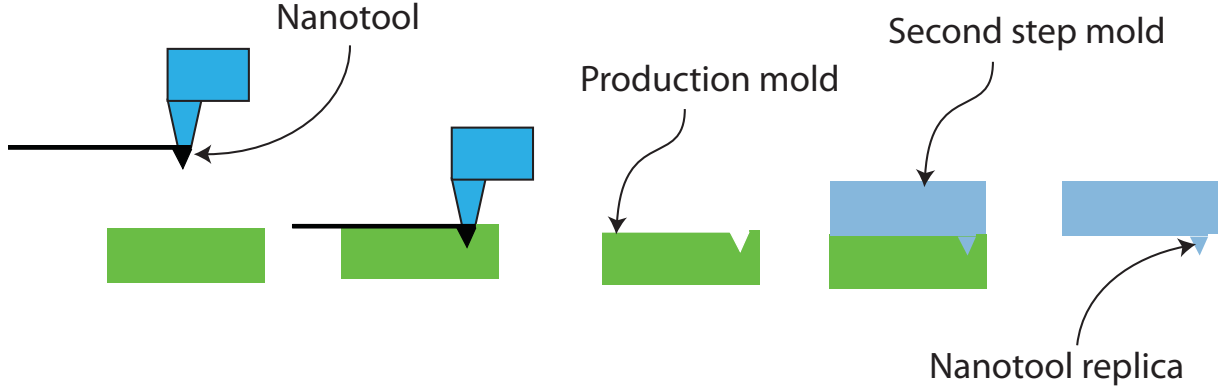


Figure 6.6: Two step molding process to produce nanotool replicas

total wear volume is determined to be $5.9 \times 10^6 \text{ nm}^3$.

It should be noted that, the presented data is not sufficient to reach deterministic conclusions regarding the particular geometry and amount of nanotool wear for the two nanomilling configurations. However, the developed framework for experimentation and analysis and the preliminary results presented in this chapter is foundational for a comprehensive study of nanotool wear.

6.3 Preliminary studies on nanotool replication for wear progression studies

A thorough experimental understanding of the wear characteristics of nanomilling necessitates frequent characterization of the nanotool at different stages of process to capture the wear progression. Although direct characterization of the nanotool through AFM measurements is a powerful tool to quantify the nanotool wear, it is a considerably time consuming process. Furthermore, it requires removal of the nanotool from the nanomilling setup at the intermediate phases of the process, disturbing the alignment of the system and adversely affecting the process repeatability. Accordingly, direct characterization of nanotools is not a feasible method for wear progression studies.

To address this issue, an alternative method is considered where indirect wear characterization at the intermediate states of the process is performed on the produced replicas (copies) of the nanotools. These replicas are obtained within the nanomilling setup without removing the nanotool. Therefore the process repeatability is not affected. To create the nanotool replicas, a two step molding process is proposed as depicted in Fig.6.6, where an inverse image of the nanotool is first obtained through elastomer molding. Next, the

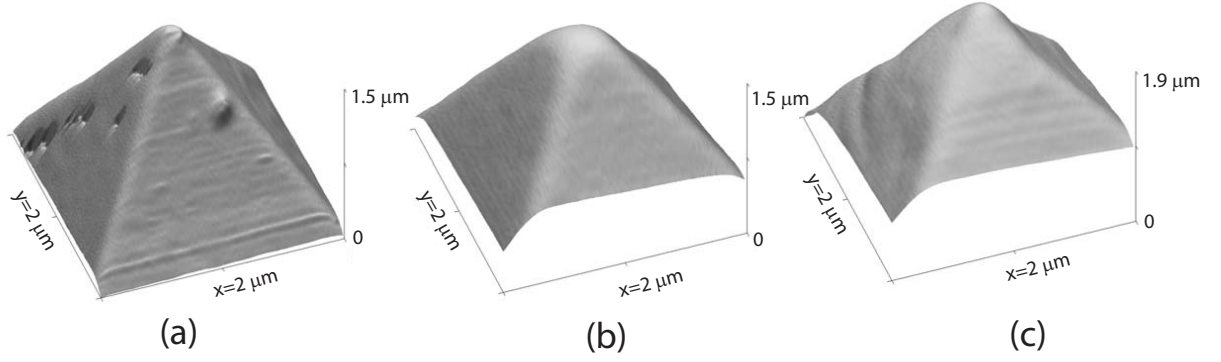


Figure 6.7: AFM images of the obtained nanotool replicas (a)Original unused nanotool (b)PU replica (c)Resin replica

obtained elastomeric mold with the inverse nanotool image is molded with another polymer to produce the replica of the nanotool. For the first step molding, a polyvinylsiloxan dental wax (President Light Body Gel, ISO 4823, polyvinylsiloxan (PLB), Coltene Whaledent, Hamburg, Germany) is used as the molding elastomer. First, the base prepolymer is mixed with its catalyst with a 1:1 mass ratio. Next, the nanotool is immersed into a small droplet of the mixture and kept for 10 minutes until the mixture solidifies. The nanotool is then raised and separated from the elastomer and the production mold is obtained.

For the second molding step, two materials are considered. First material is a UV-curable polyurethane(PU) (Norland Adhesives, NOA 63). To obtain PU replicas, the uncured liquid pre-polymer is poured on the production mold in a container. The container is spun in a centrifuge at 4000 rpm for 20 minutes. Immediately after centrifugation, the liquid pre-polymer is spot cured with a 150 Watt UV-light source for a total duration of 15 minutes. The elastomeric production mold is then stripped off and the nanotool replica is exposed. The second considered material is an embedding resin, that is obtained by mixing 4.1 g of embedding medium (ERL 4221), 1.43 g of Diglycidyl ether of Polypropylene glycol (DER 736), 5.9 g of Nonenyl succinic anhydride (NSA) and 0.1 g of Dimethylaminoethanol (DMAE). The mixture is poured in the production mold and baked at 70°C for 8 hours. The resin replica is then obtained by stripping the production mold.

Three-dimensional AFM images of an unused nanotool along with its PU and resin replicas is given in Fig. 6.7. It can be observed that the replicas are unable to accurately capture the apex of the original nanotool. It is hypothesized that the liquid pre-polymers cannot completely fill the cavity on the production mold (inverse nanotool image). Potential causes of this issue includes trapped air within the cavity and poor wettability of the production mold surface by the liquid pre-polymers. The future work includes optimization of the

nanotool replication process through selection of more suitable materials and improvement of the overall procedure.

Chapter 7

Conclusions

The research presented in this thesis aimed to develop, implement and analyze the novel tip-based mechanical nanomanufacturing method, referred to here as nanomilling. Nanomilling process uses a ultra-sharp probe tip as the nanotool and imposes high-frequency rotations to the nanotool to remove material, thereby achieving configuration similar to the conventional milling process at nano-scale.

The developed nanomilling system includes a three-axis piezo-stack actuator that hosts the nanotool and imposes the nanotool rotations, as well as a precision nanopositioning stage to feed the sample and generate desired feature shapes. The nanotool assembly is obtained by attaching a commercial AFM cantilever to the piezo-stack actuator in a reverse configuration where the probe tip (nanotool) is at the fixed end of the cantilever. This high-stiffness configuration enables the direct prescription of the removal depth rather than the normal force as in conventional tip-based mechanical nanomanufacturing methods. A laser doppler vibrometry based nanotool-sample contact detection method is developed. In this approach, the sample is vibrated with sub-nm amplitudes at the resonant frequency of the free standing nanotool cantilever. It was shown that the contact of the nanotool to the vibration sample surface results in an abrupt change vibration amplitude at the free end of the nanotool cantilever (measured by the LDV system), enabling indication of the sample surface with better 10 nm accuracy.

The accuracy of the nanomilling process requires high-precision characterization, alignment and control of the nanotool rotations and feeding motions. For this purpose, an LDV-based motion measurement system is constructed. This system utilizes three LDV beams aligned in a mutually orthogonal configuration within 0.04 degrees to measure three dimensional dynamic motions of the piezo-stack actuator and nanopositioning stage.

To accurately characterize and control the non-linear motions of the three-axis piezo-stack actuators, a new three-dimensional dynamic characterization method is developed. In this method, three-dimensional dynamic response of the actuator is analyzed in the frequency domain and categorized into response components that are measured at the excitation frequency, its harmonics and the non-harmonic frequencies. A response power analysis is conducted to identify the contribution of each response component to the total response. A novel extended frequency response function (FRF) definition is devised to separately describe each response component as a function of the excitation frequency and amplitude. Several specific conclusions regarding the dynamic response of the piezo-stack actuators are drawn from this work:

- Piezo-stack actuators do not possess stationary physical motion axes: The response is three-dimensional, and its direction for a given excitation varies mainly with the excitation frequency and secondarily with the excitation amplitude. This is an important departure from the conventional quasi-static behavior of piezoelectric actuators. Therefore, obtaining specific high-accuracy motions from piezo-stack actuators necessitates three-dimensional characterization of their dynamic behavior within a broad range of excitation frequencies and amplitudes. The developed characterization approach successfully addresses this need.
- The dynamic response of piezo-stack actuators involves relatively strong components at the harmonics of the excitation frequency, and a broad-band response at non-harmonics frequencies. This behavior, and the amplitude-dependent nonlinearities, can be effectively captured through the developed characterization technique.
- Contribution of different response (frequency) components can be analyzed through the presented power-based approach. This analysis enables identifying dominant response components, and thus, representing the dynamic behavior in a simplified fashion.
- The developed extended-FRF technique successfully represents the 3D non-linear dynamics of piezo-stack actuators within a simplified framework. This representation can be used to facilitate obtaining accurate motions from piezo-stack actuators within a broad range of frequencies and amplitudes.
- The measurement errors associated with the presented characterization technique are characterized. The maximum error for the amplitude at the fundamental frequency is less than 1.5% of the response amplitude. Although higher error percentages are

observed for higher harmonics, their corresponding response amplitude is in the pico-meter range. It is also concluded that the measurement noise and error accounts for a major portion of the measurements of (the broadband portion of) the non-harmonic response.

Using the extended-FRF based response representations obtained through dynamic characterization, a new frequency-domain-based open-loop control method is developed to accurately generate single-frequency motions using the multi-axis piezo-stack actuators. This method involves excitation of the actuator at the fundamental (motion) frequency to obtain the desired response and inclusion of a compensatory excitation at the higher harmonics of the fundamental frequency to reduce or eliminate for the higher harmonic response components. Fundamental component of excitation is directly determined using the inverse of the fundamental FRF matrices (describing the three-input three-output actuator system) and the desired response. A multi-order method is used for the harmonic compensation, where the first order compensatory excitation components can be analytically calculated using the higher harmonic FRFs (hFRFs). An iterative experimental procedure is outlined for determining the higher-order compensatory excitation components. Following conclusions are drawn from the evaluation of the developed control approach:

- The open-loop control approach were able to generate motions having amplitudes ranging from 10 nm to 240 nm with 1.1% average mean radial deviation, 4.1% average path deviation and 2.0% average normal deviation.
- The harmonic compensation successfully reduced the unwanted higher harmonic response components to acceptably low levels, resulting in more than 75% reduction in path deviation.
- The first-order harmonic compensation reduces the harmonic response power by more than 80% for many cases. For better accuracy, one should use higher-order harmonic compensation, determination of which requires an iterative compensatory testing procedure.
- Sub-nanometer levels of radial and out-of-plane non-harmonic deviations were observed for all cases. An analysis of measurement errors showed that the major contributor of the determined non-harmonic deviations is the measurement error.

Having established the method for accurate generation of nanomilling motions, the process is successfully used to create complex three-dimensional features on PMMA, SU-8 and

copper surfaces. Preliminary observations on the material removal indicated that a shearing type material removal in the form of long and curled chips is achieved through nanomilling. The dimensional accuracy of the nanomilling process is also evaluated. It was shown that the high-stiffness nanotool configuration and the implemented motion control methods enabled the control of the depth and width of the material removal with less than 5 nm average error. This error is commensurate with the repeatability of the nanopositioning stage.

Finally, preliminary studies are conducted on the analysis of the nanotool wear. An experimental framework for wear testing, methods of AFM-based nanotool wear characterization and wear volume analysis are developed. Discernible nanotool wear is observed on diamond nanotools after nanomilling of copper with a total length of 1 mm at a depth of 120 nm. The conducted preliminary studies on nanotool wear constitutes the foundation for more comprehensive studies towards a thorough understanding of wear and its dependence on various process parameters.

Chapter 8

Future Work

Research presented in this thesis provided the foundation for the implementation of mechanical material removal as an effective nano-fabrication method. The future work towards rendering the nanomilling process as a fully-controllable and industrially feasible nano-fabrication process and expanding the conducted fundamental research can be categorized into three main groups.

8.1 Completion of the fundamental research on the nanomilling process

Considering the fully-functional nanomilling system and the conducted preliminary studies, the fundamental research on the nanotool wear and material removal can now be finalized.

8.1.1 Analysis of the nanotool wear

Thorough understanding of the nanotool wear during nanomilling requires a comprehensive study of the nanotool wear progression and its relation to various process parameters. For this purpose, the development of the analysis method should be finalized and a design of experiments should be conducted.

As outlined in Chapter 6, the methodology for experimentation, AFM-based characterization of nanotools and analysis of the experimental data is established. The method development will be completed by the establishment of successful nanotool replication for efficient acquisition of wear progression data. Accordingly, primary research effort will be spent on the optimization of the two step molding process to obtain nanotool replicas. Var-

Workpiece Materials	Cu,PMMA,Si
Nanotool Materials	Si,PCD,SiN ₄
Nanomilling configurations	In-Plane,Out-of-Plane
Rotation Frequencies (kHz)	2,4,8
Feed rates (nm/rev)	1,5,10,20
Removal depth (nm)	40,80,120
Nanotool orientations	Two orientations, 60° apart

Table 8.1: Experimental parameters to be used during the experimental analysis of nanotool wear.

ious alternatives for the first and second step molding materials will be considered. For the first step molding, UV-curable polymers are the most appropriate since they can be controllably and rapidly cross-linked in ambient conditions. This enables the repeatable application of the first step molding within the nanomilling setup. For the second molding step, a number of polymers, application of which is demonstrated in nano-scale molding processes, will be considered. These polymers include but are not limited to Polydimethylsiloxane (PDMS), perfluoropolyether (PFPE), Polystyrene (PS) and Polyisocyanacrylate (PC). As per the promising preliminary results, different formulations of epoxy resins will also be considered. Furthermore, the procedural details of the two-step molding process will be revised to improve its efficiency and the repeatability.

Following the establishment of the complete wear analysis method, a detailed parametric wear study will be conducted. For this purpose, a design of wear experiments will be performed where various process parameters will be tested. A set of potential process parameters that can be studied is listed in table 8.1. For each parameter set, the wear progression curves that correlate the wear volume to the removed material volume will be obtained and the volumetric wear rate will be determined. Statistical analysis of the results for the experimental study will provide a fundamental understanding of the relations between the nanotool wear and the process parameters.

The quantitative results of the comprehensive wear study can also be utilized to devise and calibrate an empirical wear model. This model can then be used to predict the volumetric wear rate for a given set of process parameters.

8.1.2 Realization of force measurement during nanomilling

The process forces observed during the tip-based mechanical nanomanufacturing processes have been shown to be a direct indicator of the mechanics of material removal. Therefore, capability of measuring the forces acting on the nanotool is essential for understanding the

material removal during nanomilling. The current high-stiffness configuration of the nanotool does not inherently have the force measurement capability. Accordingly, a methodology for measuring forces during nanomilling and the corresponding experimental setup will be developed.

One possible design for the force measurement setup is a optical lever based apparatus consisting of a compliant cantilever. The workpiece material will be deposited near the fixed end of this cantilever. The nanomilling forces applied on the deposited workpiece can be detected through the laser-based measurement of the deflections at the free-end of the cantilever.

The specific objectives of this work include the design and calibration of the force measurement apparatus and quantification of the resolution, repeatability and bandwidth of the developed system.

8.1.3 Analysis of material removal

Preliminary observations indicated that the nanomilling process is able to remove material from the sample surfaces in the form long and curled chips. A thorough understanding of the mechanics of material removal is crucial in achieving high feature quality, dimensional accuracy and low nanotool wear. Established methods of understanding mechanics of material removal at different size scales include the in-situ observation of process forces , acoustic emission (AE) monitoring and post process analysis of the created features.

To study the mechanics of material removal and its dependence on various process parameters, a design of experiments will be conducted. These experiments will involve nanomilling of channels using different combinations of various process parameters. A tentative set of process parameters to be used during the experiments is listed in Table 8.2. During the experiments, normal nanomilling forces (using the developed apparatus) and acoustic emission signals from the workpiece will be acquired. Following the experiments, the created channels will be characterized through AFM measurements. Using the force data versus the measured depth of the channels, specific cutting energies will be determined corresponding to the each parameter set. Furthermore, using the AFM measurements of the created channels, a removal efficiency (RE) metric for each test will be determined. This metric is defined as the ratio of the volumes of the removed material and the material accumulated in the vicinity of the channels. High removal efficiency ($RE \gg 1$) indicates a true removal of material through shearing (formation of chips), whereas low removal efficiency ($RE \approx 1$) indicates a ploughing dominated removal mechanism. An analysis of variance (ANOVA) will

Workpiece Materials	Cu,Ag,Si
Nanotool Materials	PCD
Nanomilling configurations	In-Plane,Out-of-Plane
Rotation Frequencies (kHz)	2,4,8
Feed rates (nm/rev)	1,5,10,20
Removal depths (nm)	20,40,60,80,100
Nanotool orientations	30° increments

Table 8.2: Experimental parameters to be used during the experimental analysis of material removal.

be performed using the determined specific cutting energies, AE parameters and removal efficiencies to determine the statistical significance of each parameter and interactions.

Obtained specific energy data can be utilized to devise and calibrate an empirical force model. This model can than be used to predict the process forces as a function of process parameters.

8.2 Towards Industrial Feasibility of Nanomilling

Despite many advantages of the nanomilling process demonstrated in this thesis including high dimensional accuracy and material removal rates, the industrial feasibility of the process is hindered by its limited throughput. Two specific approaches can be considered in the long term to realize the high throughput implementation of the nanomilling.

8.2.1 Parallelization of the Nanomilling Process

In its current configuration, similar to other tip-based nano-fabrication methods, fabrication of nano-structures through nanomilling has a serial nature. Namely, only one feature is created at a time within micron-scale areas leading to a low process throughput. This issue can be addressed by considering parallel operation of multiple nanotools to realize creation of multiple features in larger areas. One important requirement for such an application is the heterogeneity within the large area. This requirement brings the need for nanotools that can operate independently. Such tools should possess individual sensing and actuation capabilities while maintaining the low compliance levels required for high dimensional accuracy. One potential nanotool design for this purpose is a cantilever structure including multiple layers of piezoelectric and piezoresistive materials for actuation and sensing, respectively. If successfully implemented, such a nanotool design can be used to directly sense the process forces, maintain constant nanotool position under these forces achieving

high nanotool stiffness. Furthermore, these nanotools can also be directly used for in-situ atomic force microscopy of the created features.

The specific objectives of this work will include the physical design and fabrication of the next generation nanotools, development of the electronic and software architectures to control multitude of these nanotools and performance evaluation of the parallel operation.

8.2.2 Combination of the Nanomilling and Elastomer Molding Processes

Even in the parallel implementation, throughput of the nanomilling process cannot be increased to industrially feasible levels. Such a throughput increase can be achieved by combining nanomilling process with an inherently high-rate production process. Following the growing interest for the elastomeric materials, elastomer nano-molding can be an exciting candidate. In this implementation, nanomilling process will be used as to create master-molds including nano-scale features with high dimensional accuracy. Fabricated master-molds can then be molded many times to produce large number of elastomeric molds. These molds can be used as final products themselves, production molds to be used in a second-step molding process or stamps for high-rate soft-lithography processes such as micro-contact printing (μ CP).

Successful implementation of this approach requires an in-depth study on the capability of the molding elastomers to accurately replicate the nanomilled features. Complementary to the presented research, preliminary studies were conducted on the accuracy of elastomer molding of the nanomilled features. Figure 8.1 presents the AFM images of step structure created through nanomilling and corresponding elastomer (PDMS) mold. Through this analysis, it has been concluded that the average depths of the created steps can be replicated by the PDMS mold with less than 2 nm error. These promising results indicate the potential success of such a combined method for high-accuracy, high-throughput nanofabrication.

8.3 Extension of the Fundamental Research on Dynamics of Piezo-stack Actuators

The presented fundamental research of the characterization and open-loop control of dynamic motions of piezo-stack actuators provided valuable insights on implementation of these actuators. A number of directions can be suggested for the extension of this research:

- In its current form, presented open-loop control method is limited to generation of sin-

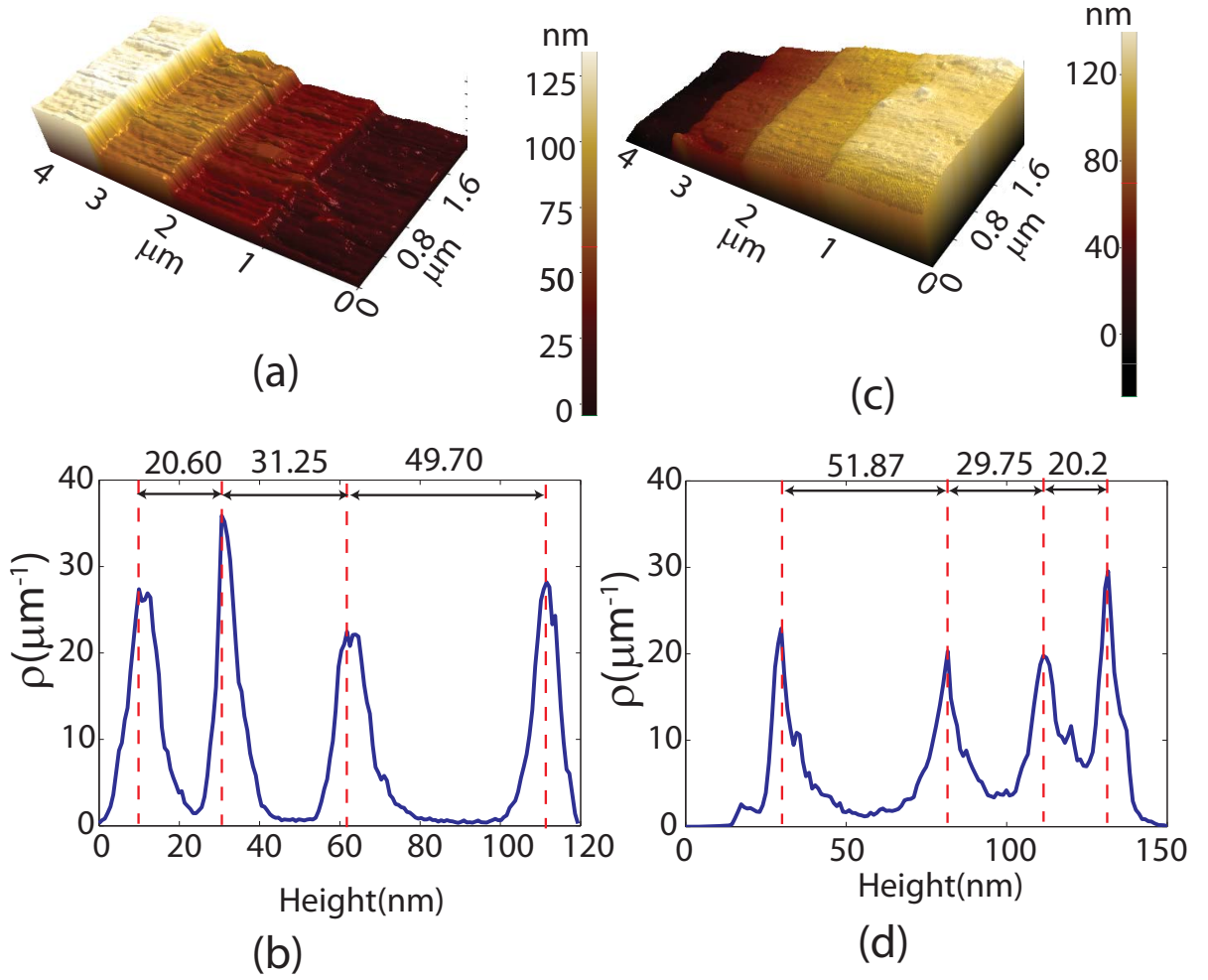


Figure 8.1: Three-dimensional AFM images and height density plots of the (a-b) step structure nanomilled on a PMMA surface and corresponding (c-d) PDMS mold

gle frequency motions. Further research can be conducted on enhancing this method for generation of more complex paths that are represented by multiple frequency response components. For this purpose, effect of the ratio of the frequencies corresponding to the targeted response components should be investigated. It can be hypothesized that the implementation of the control method will require different approaches if the targeted response frequencies are harmonics of each other, or their ratio is close to or significantly less than 1.

- The results of the dynamic characterization, particularly the novel harmonic FRF representations, can be utilized in development and implementation various non-linear dynamic system models, not only for piezo-stack actuators but also for other non-linear systems.

Bibliography

- [1] Y. Chen, A. Pepin, Nanofabrication: Conventional and nonconventional methods, *Electrophoresis* 22 (2) (2001) 187–207.
- [2] B. D. Gates, Q. Xu, M. Stewart, D. Ryan, C. G. Willson, G. M. Whitesides, New approaches to nanofabrication: molding, printing, and other techniques., *Chemical reviews* 105 (4) (2005) 1171–96.
- [3] J. Bryan, Design and construction of an ultraprecision 84 inch diamond turning machine, *Precision Engineering* 1 (1) (1979) 13–17.
- [4] W. Gao, Precision nano-fabrication and evaluation of a large area sinusoidal grid surface for a surface encoder, *Precision Engineering* 27 (3) (2003) 289–298.
- [5] H. Kim, Diamond turning of large off-axis aspheric mirrors using a fast tool servo with on-machine measurement, *Journal of Materials Processing Technology* 146 (3) (2004) 349–355.
- [6] X. Xie, H. Chung, C. Sow, a.T.S. Wee, Nanoscale materials patterning and engineering by atomic force microscopy nanolithography, *Materials Science and Engineering: R: Reports* 54 (1-2) (2006) 1–48.
- [7] A. a. Tseng, A. Notargiacomo, T. P. Chen, Nanofabrication by scanning probe microscope lithography: A review, *Journal of Vacuum Science & Technology B: Microelectronics and Nanometer Structures* 23 (3) (2005) 877.
- [8] G. Binnig, C. Quate, C. Gerber, Atomic force microscope, *Physical review letters* 56 (9) (1986) 930–933.
- [9] P. McKeown, From micro- to nano-machining towards the nanometre era, *Sensor Review* 16 (2) (1996) 4–10.

- [10] R. M. Nyffenegger, R. M. Penner, Nanometer-Scale Surface Modification Using the Scanning Probe Microscope: Progress since 1991., *Chemical reviews* 97 (4) (1997) 1195–1230.
- [11] C. Quate, Scanning probes as a lithography tool for nanostructures, *Surface Science* 386 (1-3) (1997) 259–264.
- [12] Y. Yan, T. Sun, Y. Liang, S. Dong, Investigation on AFM-based micro/nano-CNC machining system, *International Journal of Machine Tools and Manufacture* 47 (11) (2007) 1651–1659.
- [13] Y. Yan, Z. Hu, X. Zhao, T. Sun, S. Dong, X. Li, Top-down nanomechanical machining of three-dimensional nanostructures by atomic force microscopy., *Small (Weinheim an der Bergstrasse, Germany)* 6 (6) (2010) 724–8.
- [14] N. Kawasegi, N. Takano, D. Oka, N. Morita, S. Yamada, K. Kanda, S. Takano, T. Obata, K. Ashida, Nanomachining of Silicon Surface Using Atomic Force Microscope With Diamond Tip, *Journal of Manufacturing Science and Engineering* 128 (3) (2006) 723.
- [15] C. H. Choi, D. J. Lee, J.-H. Sung, M. W. Lee, S.-G. Lee, S.-G. Park, E.-H. Lee, B.-H. O, A study of AFM-based scratch process on polycarbonate surface and grating application, *Applied Surface Science* 256 (24) (2010) 7668–7671.
- [16] X. Jinal, Submicrometer modification force microscope of polymer surfaces with a surface, *Applied Physics Letters* 61 (August) (1992) 657–659.
- [17] H. Schumacher, Controlled mechanical AFM machining of two-dimensional electron systems: fabrication of a single-electron transistor, *Physica E: Low-dimensional Systems and Nanostructures* 6 (1-4) (2000) 860–863.
- [18] M. Versen, B. Klehn, U. Kunze, D. Reuter, A. Wieck, Nanoscale devices fabricated by direct machining of GaAs with an atomic force microscope, *Ultramicroscopy* 82 (1-4) (2000) 159–63.
- [19] U. Keyser, Direct fabrication of parallel quantum dots with an atomic force microscope, *Physica E: Low-dimensional Systems and Nanostructures* 13 (2-4) (2002) 1155–1158.
- [20] S. Hu, Fabrication of silicon and metal nanowires and dots using mechanical atomic force lithography, *Journal of Vacuum Science & Technology B: Microelectronics and Nanometer Structures* 16 (5) (1998) 2822.

- [21] A. Notargiacomo, V. Foglietti, E. Cianci, G. Capellini, M. Adami, P. Faraci, F. Evangelisti, C. Nicolini, Atomic force microscopy lithography as a nanodevice development technique, *Nanotechnology* 10 (1999) 458–463.
- [22] H. Gobel, Atomic force microscope as a tool for metal surface modifications, *Journal of Vacuum Science & Technology B: Microelectronics and Nanometer Structures* 13 (3) (1995) 1247.
- [23] Y. Ichida, Y. Morimoto, R. Sato, Nanomachining on Si (1 0 0) surfaces using an atomic force microscope with lateral force transducer, *Nanotech* 1 (2003) 534–537.
- [24] A. Tonck, S. Bec, Nano-machining with a surface force apparatus, *MRS Proceedings* 522 (1) (1998) 409–414.
- [25] C. Hyon, S. Choi, S. Hwang, D. Ahn, Y. Kim, E. Kim, Nano-structure fabrication and manipulation by the cantilever oscillation of an atomic force microscope, *Jpn. J. Appl. Phys* 38 (12) (1999) 7257–7259.
- [26] V. Bouchiat, D. Esteve, Lift-off lithography using an atomic force microscope, *Applied Physics Letters* 69 (20) (1996) 3098.
- [27] Q. Zhao, T. Sun, Y. Liang, S. Dong, Atomic force microscope using a diamond tip: a tool for micro/nanomachining on single-crystal silicon surface, *Proceedings of SPIE* 4601 (2001) 73–78.
- [28] T. Sun, Y. D. Yan, J. Xia, S. Dong, Y. C. Liang, K. Cheng, Research on Micro Machining Using AFM Diamond Tip, *Key Engineering Materials* 259-260 (2004) 577–581.
- [29] F. Iwata, M. Kawaguchi, H. Aoyama, a. Sasaki, Ultrasonic micromachining on Al thin film using atomic force microscopy combined quartz crystal resonator, *Thin Solid Films* 302 (1-2) (1997) 122–126.
- [30] T. Fang, C. Weng, J. Chang, Machining characterization of the nano-lithography process using atomic force microscopy, *Nanotechnology* 11 (2000) 181–187.
- [31] Z. Shen, L. Yingchun, Micro/nano-machining on silicon surface with a modified atomic force microscope 14 (003) (2001) 207–211.
- [32] K. Ashida, N. Morita, Y. Yoshida, Study on nano-machining process using mechanism of a friction force microscope, *JSME International Journal Series C* 44 (1) (2001) 244–253.

- [33] N. Kawasegi, Nanomachining Zr-based metallic glass surfaces using an atomic force microscope Noboru Morita , Shigeru Yamada and Noboru Takano Tatsuo Oyama Kiwamu Ashida, *International Journal of Machining and Machinability of Materials* 2 (1) (2007) 3–16.
- [34] F. Iwata, K. Ohara, Y. Ishizu, A. Sasaki, H. Aoyama, T. Ushiki, Nanometer-Scale Manipulation and Ultrasonic Cutting Using an Atomic Force Microscope Controlled by a Haptic Device as a Human Interface, *Japanese Journal of Applied Physics* 47 (7) (2008) 6181–6185.
- [35] Z. Hu, Y. D. Yan, T. Sun, S. Dong, Z. Zhao, Depth Control Method of AFM-Based Nanomachining with Diamond Tip in Deflection Mode, *Applied Mechanics and Materials* 10-12 (2008) 578–582.
- [36] N. S. Tambe, B. Bhushan, Nanowear Mapping: A Novel Atomic Force Microscopy Based Approach for Studying Nanoscale Wear at High Sliding Velocities, *Tribology Letters* 20 (1) (2005) 83–90.
- [37] B. W. Ahn, S. H. Lee, Characterization and acoustic emission monitoring of AFM nanomachining, *Journal of Micromechanics and Microengineering* 19 (4) (2009) 045028.
- [38] Y. Yan, T. Sun, S. Dong, Study on effects of tip geometry on AFM nanoscratching tests, *Wear* 262 (3-4) (2007) 477–483.
- [39] M. J. Adams, A. Allan, B. J. Briscoe, P. J. Doyle, D. M. Gorman, S. a. Johnson, An experimental study of the nano-scratch behaviour of poly(methyl methacrylate), *Wear* 251 (1-12) (2001) 1579–1583.
- [40] S. H. Lee, B. W. Ahn, Monitoring of Brittle-Ductile Transition during AFM Machining Using Acoustic Emission, *Key Engineering Materials* 326-328 (2006) 405–408.
- [41] B. Du, M. R. VanLandingham, Q. Zhang, T. He, Direct measurement of plowing friction and wear of a polymer thin film using the atomic force microscope, *Journal of Materials Research* 16 (05) (2001) 1487–1492.
- [42] B. Bhushan, Nanotribology and nanomechanics, *Wear* 259 (7-12) (2005) 1507–1531.
- [43] X. Zhao, Material removal mechanisms of single-crystal silicon on nanoscale and at ultralow loads, *Wear* 223 (1-2) (1998) 66–78.
- [44] J. Blach, A mechanistic approach to tip-induced nano-lithography of polymer surfaces, *Thin Solid Films* 459 (1-2) (2004) 95–99.

- [45] Y. Yan, Q. Zou, Z. Lin, A control approach to high-speed probe-based nanofabrication., *Nanotechnology* 20 (17) (2009) 175301.
- [46] F. H. Zhang, H. L. Zhang, Y. D. Yan, J. H. Wang, Research on Nanoscale Material Removal Process Using Atomic Force Microscopy, *Key Engineering Materials* 359-360 (2008) 269–273.
- [47] S. Li, T. M. Dellinger, Q. Wang, S. Szegedi, C. Liu, Pneumatically actuated elastomeric device for nanoscale surface patterning, *Applied Physics Letters* 91 (2) (2007) 023109.
- [48] R. Ribeiro, Z. Shan, a. Minor, H. Liang, In situ observation of nano-abrasive wear, *Wear* 263 (7-12) (2007) 1556–1559.
- [49] J. Michler, R. Rabe, J. Bucaille, B. Moser, P. Schwaller, J. Breguet, Investigation of wear mechanisms through in situ observation during microscratching inside the scanning electron microscope, *Wear* 259 (1-6) (2005) 18–26.
- [50] K.-h. Chung, D.-e. K. Å, Fundamental investigation of micro wear rate using an atomic force microscope, *Wear* 15 (2) (2003) 135–144.
- [51] K.-H. Chung, Y.-H. Lee, D.-E. Kim, Characteristics of fracture during the approach process and wear mechanism of a silicon AFM tip., *Ultramicroscopy* 102 (2) (2005) 161–71.
- [52] M. L. Bloo, H. Haitjema, W. O. Pril, Deformation and wear of pyramidal, silicon-nitride AFM tips scanning micrometre-size features in contact mode, *Measurement* 25 (1999) 203–211.
- [53] S. T. Zhao Q.L, Dong S., Investigation of an Atomic Force Microscope tip wear in micro/nano-machining, *Key Engineering Materials* 202-203 (2001) 315–320.
- [54] a. Khurshudov, Wear of the AFM diamond tip sliding against silicon, *Wear* 203-204 (1997) 22–27.
- [55] K.-H. Chung, D.-E. Kim, Wear characteristics of diamond-coated atomic force microscope probe., *Ultramicroscopy* 108 (1) (2007) 1–10.
- [56] B. A. Gozen, O. B. Ozdoganlar, A Rotating-Tip-Based Mechanical Nano-Manufacturing Process: Nanomilling., *Nanoscale research letters* 5 (9) (2010) 1403–1407.

- [57] D. Brehl, T. Dow, Review of vibration-assisted machining, *Precision engineering* 32 (3) (2008) 153–172.
- [58] S. Heamawatanachai, E. Bamberg, Design and characterization of a PZT driven micro-machining tool based on single-point tool tip geometry, *Precision Engineering* 33 (4) (2009) 387–394.
- [59] Polytec Vibromenter Controller OFV-5000 User Manual, 2005
- [60] Arfken, G. "Gram-Schmidt Orthogonalization." 9.3 in *Mathematical Methods for Physicists*, 3rd ed. Orlando, FL: Academic Press, 1985, pp. 516-520.
- [61] B. A. Gozen, O. B. Ozdoganlar, Design and evaluation of a mechanical nanomanufacturing system for nanomilling, *Precision Engineering* (2011) 1–12.
- [62] Y. Chen, a. J. Dick, F. H. Ghorbel, Tip trajectories of a smart micro-cantilever beam: analysis and design, *Smart Materials and Structures* 18 (11) (2009) 115012.
- [63] G. Alici, B. Shirinzadeh, J. Smith, Sliding Mode Control of a Piezoelectric Actuator with Neural Network Compensating Rate-Dependent Hysteresis, *Proceedings of the 2005 IEEE International Conference on Robotics and Automation* (April) (2005) 3641–3645.
- [64] J. Tzen, S. Jeng, W. Chieng, Modeling of piezoelectric actuator for compensation and controller design, *Precision Engineering* 27 (1) (2003) 70–86.
- [65] F. Weibel, Y. Michellod, P. Mullhaupt, D. Gillet, Real-time compensation of hysteresis in a piezoelectric-stack actuator tracking a stochastic reference, *2008 American Control Conference* (2008) 2939–2944.
- [66] D. Song, C. Li, Modeling of piezo actuator's nonlinear and frequency dependent dynamics, *Mechatronics* 9 (4) (1999) 391–410.
- [67] R. Ben Mrad, H. Hu, A model for voltage-to-displacement dynamics in piezoceramic actuators subject to dynamic-voltage excitations, *IEEE/ASME Transactions on Mechatronics* 7 (4) (2002) 479–489.
- [68] M. Arafa, a. Baz, On the Nonlinear Behavior of Piezoelectric Actuators, *Journal of Vibration and Control* 10 (3) (2004) 387–398.
- [69] M. Bryant, A characterization of the linear and non-linear dynamic performance of a practical piezoelectric actuator part 2: Theory, *Sensors and Actuators* 9 (2) (1986) 105–114.

- [70] M. Bryant, A characterization of the linear and non-linear dynamic performance of a practical piezoelectric actuator part 1: Measurements, Sensors and Actuators 9 (1986) 95–103.
- [71] Ewins DJ, Modal Testing: Theory and Practice, London, 1984.
- [72] A. Harvey, The fundamentals of FFT-based signal analysis and measurement in LabVIEW and LabWindows, Application Note (1993) 1–20.
- [73] F. Harris, On the use of windows for harmonic analysis with the discrete Fourier transform, Proceedings of the IEEE 66 (1) (1978) 51–83.
- [74] J. Johnston, Transform coding of audio signals using perceptual noise criteria, IEEE Journal on Selected Areas in Communications 6 (2) (1988) 314–323.
- [75] K. Worden, a Harmonic Probing Algorithm for the Multi-Input Volterra Series, Journal of Sound and Vibration 201 (1) (1997) 67–84.
- [76] D. Adams, Frequency Domain Arx Model and Multi-Harmonic Frf Estimators for Non-Linear Dynamic Systems, Journal of Sound and Vibration 250 (5) (2002) 935–950.
- [77] a. Chatterjee, Non-linear parameter estimation with Volterra series using the method of recursive iteration through harmonic probing, Journal of Sound and Vibration 268 (4) (2003) 657–678.
- [78] B. Shirinzadeh, J. Smith, Sliding-Mode Enhanced Adaptive Motion Tracking Control of Piezoelectric Actuation Systems for Micro/Nano Manipulation, IEEE Transactions on Control Systems Technology 16 (4) (2008) 826–833.
- [79] G. Aguirre, T. Janssens, H. Van Brussel, F. Al-Bender, Asymmetric-hysteresis compensation in piezoelectric actuators, Mechanical Systems and Signal Processing (2011) 1–14.
- [80] S. Devasia, E. Eleftheriou, S. Moheimani, A survey of control issues in nanopositioning, Control Systems Technology, IEEE Transactions on 15 (5) (2007) 802–823.
- [81] W. T. Ang, P. K. Khosla, C. N. Riviere, Feedforward Controller With Inverse Rate-Dependent Model for Piezoelectric Actuators in Trajectory-Tracking Applications, IEEE/ASME Transactions on Mechatronics 12 (2) (2007) 134–142.
- [82] M. Rakotondrabe, C. Clévy, P. Lutz, Complete open loop control of hysteretic, creeped, and oscillating piezoelectric cantilevers, Automation Science and Engineering, IEEE Transactions on 7 (3) (2010) 440–450.

- [83] M. Rakotondrabe, Bouc Wen Modeling and Inverse Multiplicative Structure Actuators, *IEEE Transactions on Automation Science and Engineering* 8 (2) (2011) 428–431.
- [84] S. Bashash, N. Jalili, Intelligence rules of hysteresis in the feedforward trajectory control of piezoelectrically-driven nanostagers, *Journal of Micromechanics and Microengineering* 17 (2) (2007) 342–349.
- [85] Y. Wu, Q. Zou, Iterative control approach to compensate for both the hysteresis and the dynamics effects of piezo actuators, *Control Systems Technology, IEEE Transactions on* 15 (5) (2007) 936–944.
- [86] S. Salapaka, a. Sebastian, J. P. Cleveland, M. V. Salapaka, High bandwidth nanopositioner: A robust control approach, *Review of Scientific Instruments* 73 (9) (2002) 3232.
- [87] S. S. Aphale, S. Devasia, S. O. Reza Moheimani, High-bandwidth control of a piezoelectric nanopositioning stage in the presence of plant uncertainties., *Nanotechnology* 19 (12) (2008) 125503.
- [88] G. Gu, L. Zhu, High-speed tracking control of piezoelectric actuators using an ellipse-based hysteresis model., *The Review of scientific instruments* 81 (8) (2010) 085104.
- [89] M. Kageshima, S. Togo, Y. J. Li, Y. Naitoh, Y. Sugawara, Wideband and hysteresis-free regulation of piezoelectric actuator based on induced current for high-speed scanning probe microscopy, *Review of Scientific Instruments* 77 (10) (2006) 103701.
- [90] K. Furutani, M. Urushibata, Improvement of control method for piezoelectric actuator by combining induced charge feedback with inverse transfer function compensation, in: *Proceedings of the 1998 IEEE International Conference on Robotics & Automation* Louven. Belgium ,May 1998, no. May, 1998, pp. 1504–1509.
- [91] B. A. Gozen, O. B. Ozdoganlar, Characterization of Three-Dimensional Dynamics of Piezo-Stack Actuators, *Mechanical Systems and Signal Processing*, <http://dx.doi.org/10.1016/j.ymssp.2012.03.021>
- [92] S. Braun, The synchronous (time domain) average revisited, *Mechanical Systems and Signal Processing*,(25) 4 (2011) 1087–1102
- [93] ISO 230-4:2005 Test code for machine tools Part 4: Circular Tests for numerically controlled machine tools (2005).